

C.1

DAMAGE GROWTH IN BENDING OF COMPOSITE BEAMS

By

MARK NORMAN DOROSH

B.A.Sc., The University of British Columbia, 1985

A THESIS SUBMITTED IN PARTIAL FULFILLMENT OF
THE REQUIREMENTS FOR THE DEGREE OF
MASTER OF APPLIED SCIENCE

in

THE FACULTY OF GRADUATE STUDIES
Department of Metals and Materials Engineering

We accept this thesis as conforming
to the required standard

THE UNIVERSITY OF BRITISH COLUMBIA

April 1988

© Mark Norman Dorosh, 1988

In presenting this thesis in partial fulfilment of the requirements for an advanced degree at the University of British Columbia, I agree that the Library shall make it freely available for reference and study. I further agree that permission for extensive copying of this thesis for scholarly purposes may be granted by the head of my department or by his or her representatives. It is understood that copying or publication of this thesis for financial gain shall not be allowed without my written permission.

Department of Metals & Materials Engineering

The University of British Columbia
1956 Main Mall
Vancouver, Canada
V6T 1Y3

Date April 25, 1988

ABSTRACT

A study has been made of glass fibre reinforced plastic beams in three-point bending. In recent years, the importance of flexural loading in composites has manifested itself in the form of composite leaf springs, helicopter rotors, and other applications. This study is directed at the initiation, growth, characterization and measurement of damage in unidirectional and cross-ply composite beams.

Beams were tested in three-point static and cyclic bending. Following damage initiation, either by a machined notch or by repeated cycling, damage growth has been characterized by two damage parameters: a damage depth encompassing a number of broken fibres on the tensile surface at the central load point, and a damage length or delamination parallel to the beam longitudinal axis.

A model was developed to predict the compliance, or deflection under applied load, as a function of beam properties and damage dimensions. The model is able to predict the compliance of damaged beams with reasonable accuracy. From fracture mechanics concepts it is shown that the two damage dimensions, depth and length, are related. It is concluded that the increase in compliance, a result of the growing damage dimensions, is related to the growth of the damage depth; the damage length follows from the relation between damage parameters and the compliance follows from the compliance model.

The damage state can thus be determined by compliance measurements if the relevant material properties and loading conditions are known. However, in service, compliance measurements may not be practical. Therefore a section of this study is devoted to an

alternative damage measurement technique, namely acoustic emission monitoring. Damage initiation, compliance, damage length and damage depth were measured with AE monitoring techniques.

Table of Contents

Abstract	ii
Table of Contents	iv
List of Tables	vi
List of Figures	vii
Notation	x
Acknowledgement	xii
1 Introduction	1
2 Growth and Measurement of Damage in Composites	6
2.1 Damage Growth	6
2.1.1 Applications of Linear Elastic Fracture Mechanics	9
2.1.2 Fatigue	11
2.1.3 Flexure	12
2.2 Damage Measurement	15
2.2.1 Stiffness Reduction	15
2.2.2 Acoustic Emission	17
3 Fracture and Fatigue of Unidirectional Composite Beams	38
3.1 Experimental Procedure	38
3.2 Results	40
3.2.1 Fracture	41
3.2.2 Fatigue	44
3.3 Stiffness Reduction	49
3.3.1 Comparison With Experiment	53

3.4 Energy Release Rate	57
3.4.1 Relation Between Damage Parameters	59
3.5 Damage Development	63
4 Fracture and Fatigue of Cross-ply Composite Beams	99
4.1 Experimental Procedure	99
4.2 Results	100
4.3 Stiffness Reduction	102
4.3.1 Comparison With Experiment	104
4.4 Energy Release Rate	105
4.5 Damage Development	106
5 Damage Detection	113
5.1 Experimental Procedure	113
5.2 Damage Initiation	114
5.3 Compliance	117
5.4 Damage Length	119
5.5 Damage Depth	125
6 Summary and Conclusions	157
6.1 Unidirectional Beams	157
6.2 Cross-ply Beams	159
6.3 Damage Measurement	159
References	161
Appendix A	165
Appendix B	170
Appendix C	173

List of Tables

Table	Page
1.1 Comparison of mechanical properties of metals and high performance composites.	1
2.1 Characterization of failure modes in CFRP by AE amplitudes.	26
2.2 Characterization of damage processes using AE duration and amplitude.	27
2.3 Comparison of critical energy release rates of metals and glass/epoxy.	33
3.1 Rod types.	38
3.2 Damage length, depth and compliance, static test.	43
3.3 Fatigue test conditions.	44
3.4 Growth rate of damage depth, type II rods.	47
3.5 Growth rate of damage depth, type III rods.	48
3.6 Comparison of measured and predicted compliance.	55
4.1 Laminate test conditions.	100
4.2 Damage growth in laminate L.	102
5.1 Damage initiation.	115
5.2 Event parameters at crack fronts.	122

List of Figures

Figure		Page
2.1	Failure of clear Douglas Fir parallel to the grain, three point bending.	36
2.2	Typical acoustic emission waveform.	37
3.1 (a)	Three point bending apparatus.	66
3.1 (b)	Details of three point bending apparatus.	67
3.2 (a)	Broom-like fracture zone in type II rod.	68
3.2 (b)	Schematic representation of damaged rod.	68
3.3	Damage profile of type I rod.	69
3.4	Compliance increase in type I rod with increasing damage zone size.	70
3.5	Damage profile of type II rod A ($R=0.10$).	71
3.6	Damage profile of type II rod I ($R=0.45$).	71
3.7	Damage profiles at the central load point of type II rods.	72
3.8	Increase in damage length as a function of cycles for type II rods.	73
3.9	Increase in damage depth as a function of cycles for type II rods.	74
3.10	Increase in compliance as a function of cycles for type II rods.....	75
3.11	Damage profile of type III rod G ($R=0.17$).	76
3.12	Damage profile of type III rod F ($R=0.45$).	76
3.13	Increase in damage length for type III rods F and G as a function of cycles.	77
3.14	Damage profiles at the central load point of type III rods.	78
3.15	Increase in damage depth as a function of cycles for type III rods.	79
3.16	Increase in compliance as a function of cycles for type III rods.	80
3.17	Damaged rod modeled as a non-uniform cantilever beam.	81
3.18	Measured vs. predicted compliance for type I rods, static loading.	82
3.19	Measured vs. predicted compliance for type II rod, static loading.	83
3.20	Measured vs. predicted compliance for type III rods, static loading. .	84
3.21	Measured vs. predicted compliance for type II rods, $R=0.10$	85
3.22	Measured vs. predicted compliance for type II rods, $R=0.17$	86
3.23	Measured vs. predicted compliance for type II rods, $R=0.45$	87
3.24	Measured vs. predicted compliance for type III rods, $R=0.17$	88

3.25	Measured vs. predicted compliance for type III rods, $R=0.45$	89
3.26	Damage growth hypothesis.	90
3.27	Growth in damage length at constant lengthwise crack resistance, G_c	91
3.28	Relation between damage depth and length, type I rod, static loading.	92
3.29	Relation between damage depth and length, type I rod, static loading.	93
3.30	Increase in critical energy release rate with increase in longitudinal crack area, type II rod, static loading.	94
3.31	Relation between damage depth and length, type II rods, cyclic loading.	95
3.32	Increase in critical energy release rate with increase in longitudinal crack area, type III rods, static loading.	96
3.33	Relation between damage depth and length, type III rods, cyclic loading.	97
3.34	Relation between damage depth and length, Type III rods, cyclic loading.	98
4.1	Test sample cut from glass reinforced polyester man-lift boom.	108
4.2	Laminate edge.	109
4.3	Increase in compliance as a function of cycles, laminate K.	110
4.4	Measured vs. predicted compliance, laminates K and L. The solid line represents ideal agreement between theory and experiment.	111
4.5	Critical energy release rate as a function of damage length, Laminate L.	112
5.1	Acoustic emission monitoring.	130
5.2	Damage initiation, rod A.	131
5.3	Damage initiation, rod I.	132
5.4	Damage initiation, rod E.	133
5.5	Damage initiation, laminate J.	134
5.6	Amplitude distribution histograms for rod A for increasing cycles. ...	135
5.7	Energy distribution histograms for rod A for increasing cycles.	136
5.8	Energy distribution histograms (energy > 100) for rod A for increasing cycles.	137
5.9	Cumulative AE events with energy greater than 100 (N_{100} as a function of damaged cross sectional area, rods A, B and C.	138
5.10	Cross sectional area damaged as a function of compliance for rods A, B and C.	139

5.11	AE events as a function of normalized compliance, rods A, B and C.	140
5.12	One dimensional AE source location.	141
5.13	Transducer positioning.	141
5.14	Location histogram between 2600 and 2700 cycles, rod G.	142
5.15	Location histogram between 2600 and 2700 cycles, rod G.	143
5.16	Series of location histograms for rod G.	144
5.17	Damage length measured by source location as a function of actual damage length, rod G.	145
5.18	(a-e) Series of location histograms for laminate L. (f) Damage length measured by AE source location as a function of actual damage length, laminate L.	146
5.19	Attenuation of energy transmitted by pulser as a function of damage depth, rods A and B.	147
5.20	Change in AE parameters from pulser as a function of normalized compliance, rod D. (a) change in travel time. (b) change in amplitude. (c) change in duration. (d) change in energy.	148
5.21	Change in AE parameters from pulser as a function of normalized compliance, rod E. (a) change in travel time. (b) change in amplitude. (c) change in duration. (d) change in energy.	149
5.22	Change in AE parameters from pulser as a function of normalized compliance, rod F. (a) change in travel time. (b) change in amplitude. (c) change in duration. (d) change in energy.	150
5.23	Change in AE parameters from pulser as a function of normalized compliance, rod G. (a) change in travel time. (b) change in amplitude. (c) change in duration. (d) change in energy.	151
5.24	Change in AE parameters from pulser as a function of normalized compliance, rod H. (a) change in travel time. (b) change in amplitude. (c) change in duration. (d) change in energy.	152
5.25	Change in AE parameters from pulser as a function of normalized compliance, rod I. (a) change in travel time. (b) change in amplitude. (c) change in duration. (d) change in energy.	153
5.26	Attenuation of energy transmitted as a function of damage length, rods F and G.	154
5.27	Attenuation of energy transmitted as a function of damage depth, rods F and G.	155
5.28	Change in AE parameters from pulser as a function of normalized compliance, laminate L. (a) change in travel time. (b) change in amplitude. (c) change in duration. (d) change in energy.	156

Notation

a	Longitudinal crack half-length
A_u	Area of undamaged rod cross section
A_d	Area of damaged rod cross section
b	Width
C	Compliance
C_o	Initial compliance
d	Damage depth
e^o	Midplane strain
E	Young's modulus
E_{11}, E_L	Longitudinal Young's modulus
E_{22}, E_T	Transverse Young's modulus
G	Energy release rate
G_c	Critical energy release rate
G_I	Mode I energy release rate
G_{II}	Mode II energy release rate
G_{LT}	Shear modulus
I_1	Area moment of inertia of undamaged rod cross section
I_2	Area moment of inertia of damaged rod cross section
k	Plate curvature
K	Stress intensity factor
ΔK	Stress intensity factor range
K_{IC}	Mode I fracture toughness
l	Span
M	Moment

N	Cycles
N_{100}	Acoustic emission events with energy > 100
P	Load
P_{max}	Maximum load
r	Rod radius
t	Laminate thickness
T	Travel time of simulated acoustic emission waveform
v	Velocity of simulated acoustic emission waveform
w	End deflection of cantilever beam
σ	Stress
σ_{max}	Maximum stress
AE	Acoustic emission
CCT	Centre Cracked Tension fracture specimen
CFRP	Carbon Fibre Reinforced Plastic
FRP	Fibre Reinforced Plastic
GFRP	Glass Fibre Reinforced Plastic
LEFM	Linear Elastic Fracture Mechanics
NDE	Non Destructive Evaluation
NDT	Non Destructive Testing

ACKNOWLEDGMENT

Many people have been most generous in their support of this research effort. I wish to especially thank Dr. A. Poursartip for his guidance, advice and technical assistance throughout the course of this study; to the late Professor J.S. Nadeau for his inspiration and encouragement; and to Professor E. Teghtsoonian for his helpful suggestions and support. My thanks are also extended to fellow members of the Composites Group, in particular Mr. R. Bennett, Mr. D. Chinatambi and Mr. P. Ostaff for their valuable technical assistance. I am also grateful to the Natural Sciences and Engineering Research Council of Canada for providing funding for this study in the form of a Research Assistantship.

1 INTRODUCTION

Composite materials are suited to many structural applications because of their high strength and stiffness to weight ratios over more conventional materials such as steel and aluminum. Further advantages to fabricating structures from composites are the ability to integrate mechanical assemblies with unique processing techniques and high resistance to fracture and fatigue.

As early as 1953 glass fibre reinforced epoxy was used for its high strength and light weight by the Marietta Corporation to manufacture filament wound rocket motor casings. Carbon fibres were commercialized in the late 1960's when Union Carbide introduced Thornel 25, the first high strength, high modulus carbon fibre. In 1971 DuPont introduced a high strength, high modulus, light weight aramid (aromatic polyamide) fibre under the trade names Kevlar 29 and Kevlar 49. The mechanical properties of these fibres as they might be used in a practical structure are listed in Table 1.1 along with the properties of their metallic competitors.

Table 1.1 Comparison of Mechanical Properties of Metals and High Performance Composites.

Material	Modulus (GPa)	Tensile Strength (MPa)	Specific Modulus (km)	Specific UTS (km)
4340 Steel	210	1827	2720	23.7
7075-T651 Aluminum	73	544	2750	20.5
AS4 Carbon*	55	591	3437	36.9
Kevlar 49*	29	375	1986	25.6
E-Glass*	19	425	1053	23.6

*60% volume fraction of fibres in epoxy matrix, (0/90/±45), laminate.

The majority of composite applications combine one of these three fibre types in a thermoset or thermoplastic matrix. Common thermosetting resins are epoxy, polyester and vinyl ester. The thermosets are generally easy to work with, have excellent creep and fatigue properties and adhere well to the fibres. Unfortunately their performance deteriorates in humid environments and at temperatures as low as 350 deg F. Of particular concern is the tendency of the matrix to absorb moisture, gain weight and swell at high temperatures. Thermoplastic matrices are relatively new. Among these are J and K polymers developed by DuPont and Torlon developed by Amoco Chemicals. J and K polymers can withstand temperatures up to 450 degrees F and have excellent resistance to impact and environmental deterioration. Torlon can withstand 500 degrees F and has been used successfully in internal combustion engines [1].

Besides the easily quantifiable advantages of strength and stiffness, there are other more subtle attractions to engineering structures made from composites. One of these is realized where composites are used not by material replacement but by material design. Composites, when applied efficiently, can be designed to give desired stiffness and strength in specified directions. An excellent example of this is found in high strength, light weight pressure vessels. Fibres of glass or carbon are wound onto a cylinder at an angle of 55 degrees to the longitudinal axis to provide resistance to hoop and longitudinal stresses by apportioning the material strength to match the applied stress. (In a pressure vessel the longitudinal stress is exactly twice the hoop stress). Another example has recently been given by Davidson [2] in a design for helicopter rotor linkages. Beams made of unidirectional glass fibre/epoxy with an "H" shaped cross section were fabricated to provide the required bending stiffness to attach the rotor blades to the hub. Simultaneously, the desired lack of torsional rigidity, inherent in composites, was built in. The twofold advantages were a reduction in weight and a reduction in number of parts.

The synergistic effect of materials design as an advantage over materials replacement has also been explored by the automotive industry. Beardmore [3] has reported on an integrated composite rear suspension package for the Ford Escort. A single transverse FRP leaf spring with metal end attachments was designed to replace the basic steel suspension consisting of two coil springs, two lower arms and two spring seats. Where material replacement alone of FRP for steel would have resulted in some weight saving, the combination of material replacement and part integration resulted in a weight reduction of 8 pounds from the original 16. To date most major auto manufacturers have embarked on programs involving production of composite leaf springs. In addition to weight savings the composite spring has excellent fatigue resistance. In 1981 Chevrolet introduced glass fibre reinforced epoxy leaf springs on 80,000 Corvette models. Since then General Motors has installed nearly 400,000 similar springs per year on its Astrovan.

Another of Ford's research efforts involved the fabrication of an all-composite car [4]. A 1986 full size Ford LTD fabricated of CFRP weighed 2504 pounds compared to 3750 pounds for the production model with no perceptible difference between vehicles. This significant weight reduction was due primarily to body, suspension and drive train assemblies. The success of this project showed that one car could be made although the challenge remains to do it economically.

In contrast to the high volume and economic constraints placed on composite structures by the auto industry are the more well known applications of the aerospace industry. Growth in the market for high performance composites (those used in place of traditional engineering materials such as steel) has taken place in areas in which designs tend to be conservative and composites have been chosen for their performance, regardless of cost.

With the commercialization of carbon and Kevlar several sophisticated applications have taken advantage of these fibres' strength, stiffness and light weight. A recent example is Burt Rutan's Voyager aircraft which completed its 12 day non-stop circle of the globe in 1987. The structure of the all composite aircraft, with a main wing comparable in length to a Boeing 737 (111 ft.), was kept to 839 pounds. The weight on takeoff, with enough fuel for the 28,000 mile flight, was 11,300 pounds. The light weight and structural integrity were achieved through efficient use of carbon, Kevlar and glass fibre composites [5]

Examples of aircraft containing primary structural components (components whose failure renders the aircraft incapable of flight) are numerous. In military aircraft, boron/epoxy and carbon/epoxy have been used on fuselage and horizontal and vertical tail sections of the General Dynamics F-111 and YF-16, the Northrop F-5, the Grumman F-14 and the McDonnell-Douglas F-15 and F-18 [6]. The increased use of composites has a further effect on weight reduction in that as more composites are used the weight reduces and as the weight reduces smaller parts are needed, which further reduces the weight. This technology is being applied to commercial aircraft to reduce structural weight in floors, doors and fairings. The obvious advantages are increased payload ability, operating range or efficiency. An added bonus of composites is their improved fatigue life over aluminum alloys.

Space applications have included the space shuttle's 60 foot long cargo bay doors and 112 foot long 12 foot diameter filament wound solid rocket booster case, both of carbon/epoxy. Satellite structures have taken advantage of the light weight of carbon fibre composites. One example is a 550 kg class satellite designed in Japan [7]. Centre body, equipment panels and propulsion system support were all made of a carbon/epoxy and honeycomb core sandwich structure.

Unfortunately, with the exception of leaf springs in cars and the most expensive aerospace applications, composites have not been used to their maximum advantage as structural components. Part of this is due to a lack of design experience, such as joining and processing, and part is due to a lack of acceptable methods to predict life. In the present work, composites are studied in the form of one of the most basic structural elements, the cantilever beam. Aspects of fracture, fatigue and damage assessment in composite beams have not received widespread attention and are therefore the subject of this work.

2 GROWTH AND MEASUREMENT OF DAMAGE IN COMPOSITES

The superiority of composites as structural materials in terms of strength, stiffness and light weight have been proven by the foregoing applications. The final concern facing engineering applications, particularly those in aerospace, is the life of the structure. Much has yet to be learned about how composites fail. The developing methodologies of fracture mechanics as applied to metals can to some extent be applied to composites. Often, however, the complex nature of orthotropic composites leads to a multiplicity of failure modes and overwhelms even the most sophisticated fracture mechanics analyses. Damage resulting from processing flaws, airborne projectile threats, accidental impact, thermal cycling, cyclic loading, stress concentrations, ultraviolet light and moisture ingress can all lead to failure. The study of the fracture mechanics and fatigue of composites has emerged as one of the major areas of composite materials research.

Typically, fracture mechanics analyses yield a relation between the integrity of a structural element based on a flaw size (such as a crack length) and an applied load. The residual life of a component can be assessed if the location and size of flaws can be estimated with confidence. Thus methods of damage measurement are synonymous with studies of damage growth.

2.1 Damage Growth

In designing metallic structures, linear elastic fracture mechanics (LEFM) has been used to identify a material parameter (toughness) which can be used in material selection. In its simplest form, LEFM can be used for failure prediction. When a crack in a plate reaches a certain size the *stress intensity factor*, a function of load, loading geometry and crack size, exceeds the *fracture toughness* and failure occurs as the crack propagates,

separating the plate into two pieces. This is analogous to the concept of yield strength. The same plate, with a smaller or non-existent crack, will fail by deforming permanently when the applied stress meets or exceeds the yield strength. The philosophy of designing using fracture mechanics concepts assumes that all structures contain initial cracks. These cracks can be tolerated if the stress intensity factor does not exceed the fracture toughness. The size of the initial allowable crack size is related to non-destructive testing (NDT) thresholds. If available NDT techniques can detect cracks 1 mm in length or more, then the structure must be designed to tolerate 1 mm cracks. The power of LEFM is that, like yield strength concepts, it is relatively insensitive to material dimensions. Stress intensity solutions exist for several crack geometries (see, for example "The Stress Analysis of Cracks Handbook" [8]). Fracture toughness values determined on laboratory size specimens are equally applicable to full scale structures. Thus, when the stress intensity at a crack in a structure reaches the fracture toughness of the same material as determined in the lab, catastrophic crack extension is predicted to occur.

In composites the idea of "failure" does not separate so logically between yielding and fracture. The constituents of a composite are, to a good approximation, linearly elastic to fracture for the fibres and matrices discussed above. Therefore a concept of failure by yielding as in metals does not exist. Any material can of course fail by fracture when the load applied to it exceeds an ultimate strength. Failure theories advanced by Tsai and Hill [9] have been applied successfully to composite laminates. In this case a ply of a laminate is assumed to fail when the stress applied to it reaches its ultimate strength. This is analogous to the Von Mises failure criteria for metals where a combined stress state causes yielding. This approach is satisfactory for structures without stress concentrators such as holes, notches or cracks.

For composites containing cracks LEFM can be used, with caution, only where the nature of the failure mechanism is well defined because a composite may exhibit several failure modes. In a unidirectional lamina a crack growing transverse to the fibre direction, with loading parallel to the fibre direction, the sequence of events is as follows : matrix crack extension to a fibre/matrix interface, debonding of the fibre/matrix interface parallel to the fibre direction, fracture of the fibre, and pull-out of the fibre from the matrix. When unidirectional lamina are stacked together in a laminate cracks often grow in different directions in lamina with different fibre orientation. As a result a unique crack length cannot be defined. Instead a damage zone ahead of the crack tip is often considered. The damage zone may contain energy absorbing mechanisms such as fibre breakage, debonding and pullout. Also in a laminate the possibility of delamination is introduced. This involves the initiation and propagation of cracks in the matrix layer between layers of fibres.

In metals the computation of stress intensity factors is based on a stress field near a crack tip which is proportional to the applied stress and reciprocal of the square root of the distance from the crack tip. The extension of LEFM from homogeneous isotropic materials to homogeneous anisotropic materials can be made by calculating anisotropic stress intensity factors from isotropic ones using complex variable mapping techniques [10]. On a macroscopic scale homogeneity is usually a valid assumption. On the microscopic scale of fracture processes, however, composites often behave heterogeneously.

An alternative approach, the energy release rate, was developed by Griffith [11] in 1921. Simply stated, a crack will extend when the energy required to create new surfaces can just be delivered by the system. Stated mathematically, a crack will grow when the change in compliance with respect to change in crack length reaches some critical value related to the fracture toughness. This is a popular approach in composites research as the

energy release rate is much easier to derive than the stress intensity factor. Fracture toughness values are often difficult to measure, however, as energy of fracture may be dissipated in several ways.

2.1.1 Linear Elastic Fracture Mechanics

Several authors have studied the fracture mechanics of unidirectional composites using LEFM. The dominant issue seems to be the circumstances under which LEFM can be used to characterize crack growth. Beaumont and Phillips [12] studied glass and carbon fibres in an epoxy matrix. By treating the fibres they were able to alter the shear strength of the interfacial bond between fibre and matrix. The untreated fibres had a weak interface due to low shear strength between the fibre and matrix. In unidirectional coupons with transverse notches these specimens showed no notch sensitivity. Cracks formed and grew parallel to the fibres; the notch did not extend. In tests on coupons with treated fibres the interfacial strength was improved and the material became more notch sensitive. As the sharpness (crack length/tip radius) of the initial notch was increased crack growth became self similar and LEFM was useful in predicting the notched strength of the laminates. In later work Beaumont and Tetelman [13] found that the fracture stress of unidirectional composites could be predicted by LEFM provided the longitudinal stress at the crack tip reached a maximum before longitudinal splitting occurred. Otherwise microstructural damage occurs at the crack tip before K_{IC} is reached. Once again, increasing the bond strength reduced the fracture toughness by increasing the notch sensitivity. Under fatigue loading, however, even strong interfacial bonds break down making the composite notch insensitive which leads to longer life.

In cases where the material is notch insensitive a longitudinal split may propagate from a notch root parallel to the fibre direction. Wolla and Goree [14] investigated centre notched glass fibre reinforced epoxy under tension and observed acceleration of longitudinal split growth. Using a shear lag theory they explain how loads are transferred around the notch to fibres on either side by shear. The model predicts that the stress for split initiation decreases as notch width increases. However the model is unable to predict the final length of the split.

Using a compact tension specimen Slepetz and Carlson [15] tested unidirectional glass laminates with the fibres oriented at various angles to the loading direction. Regardless of the angle between fibre and load direction they found the crack always propagated parallel to the fibre direction with no fibre breakage. All samples exhibited some amount of "fibre bridging" behind the advancing crack tip. A network of fibres was pulled across the crack surface well away from the crack tip. This tended to increase strength, stiffness and fracture toughness compared to machined cracks. It was found that toughness did not vary with fibre orientation. For various orientations they verified the important result that $G_c = G_I + G_{II} = \text{constant}$. For fibres at an angle to the loading direction the relative contributions of G_I and G_{II} vary, but their sum is a material constant. In cross ply configurations damage grew not by crack extension but by an expanding damage zone. This type of damage is comparable to, but much larger than, the plastic zone found ahead of a crack tip in a metal. In this case LEFM was inappropriate.

In testing three point bend specimens with fibres 0 and 45 degrees to the longitudinal axis Konish et al [16] found the same energy release rate for both. This was explained by both specimens having the same matrix toughness. For the 45 deg specimen the crack was not colinear with the initial transverse crack, but once it propagated at 45 deg it did grow in

a self similar manner. The force driving the crack is a mix of modes I and II but $G_c = G_I + G_{II} = \text{constant}$. For the 0 degree specimens a crack of depth 0.6" was cut and ultrasonically sharpened. The crack grew coplanar to the initial one before splitting longitudinally and making a series of sharp turns to regain its original direction. In the 45 deg specimen the crack grew along a path containing no fibres.

2.1.2 Fatigue

Among the most important questions surrounding composite materials performance are their stiffness, strength and life. Stiffness is routinely predicted or designed by use of mechanics of solids or, by extension of Hooke's Law from isotropic to orthotropic materials, laminated plate theory. Strength can be predicted with some success based on the Tsai-Hill failure criteria or other fracture concepts outlined above. Under cyclic loading, however, the stiffness and strength may reduce significantly over time due to matrix cracking, delamination or debonding.

Reifsneider [17] has separated life into initiation and growth. It is assumed that all engineering materials contain initial flaws in the form of material discontinuities or manufacturing defects. When the material is put into service these flaws become the sites of damage initiation.

Once initiated damage may grow by accumulation or may obey some growth law. Where LEFM can be applied life prediction may be based on the Paris Law. This assumes that most of the life is spent in the growth phase. The growth of damage is proportional to some power of the stress intensity amplitude, ΔK (or ΔG). This approach does not account

specifically for thresholds below which damage does not grow, temperature, corrosive environments or frequency effects. It becomes very useful, however, when compliance changes as a result of cyclic phenomenon can be measured and related to ΔG .

Delaminations that initiate from impacts, such as those from bird strikes, dropped tools, or stones are very difficult to detect when an impact does not result in through penetration of the laminate. If the delamination goes unrepaired in-service loads cause it to grow which can result in significant losses in compressive and tensile strength and stiffness [18]. Crack growth in metals under fatigue loading is often described by the Paris Law, $da/dN = C\Delta K^n$. In composites delamination growth has been described by the same law, substituting ΔG [19] or G_{\max} [20] for ΔK . Poursartip [20] has replaced the ΔK term with G_{\max}/G_R to describe the growth of edge delaminations. The G_R term takes into account the increase in resistance to crack propagation as the delamination grows; the other expressions imply that resistance to crack propagation is constant.

Effects of hot, wet environments do not seem to have an effect on fibre dominated properties, but can have adverse effects on matrix dominated properties [21]. High temperature and moisture lower matrix mechanical properties and combined with their fatigue sensitivity result in lower fatigue strengths for angle ply laminates.

2.1.3 Flexure

Since bending has taken on some importance in the auto industry in the form of leaf springs some recent efforts have turned from tension testing to flexure testing.

Damage growth in unidirectional beams in three point bending has been observed to occur in two directions: a damage depth on the tension side initiating at a point of maximum stress and a damage length parallel to the beam longitudinal axis in the form of a

split initiating at the damage depth. This type of damage growth was observed by Bodig and Jayne [22] on beams of Douglas Fir and Poursartip et al [23] in tests on unidirectional glass reinforced polyester rods. In [22] longitudinal splits parallel to the grain of a wood beam were observed at a certain notch depth, figure 2.1. In [23] the damage depth and length were measured and input into a compliance model which accurately predicted the bending stiffness of the damaged specimens.

De Roo and Paluch [24] have studied the fatigue of rectangular unidirectional glass reinforced plastic beams in three point bending in order to gain insight into the long term behaviour of composite leaf springs. They note that damage develops on the tension side through the depth and along the length. Damage through the depth was modeled using a damage law with three parameters:

$$\frac{dD}{dN} = \frac{A(\Delta\sigma)^p}{(1-D)^q} \quad (2.4)$$

where D is the reduction in extensional modulus and A , p and q are constants. The beam was divided into elements small enough for the stress state to be considered homogeneous within a volume element. For each volume element growth in the depth progressed until D in Eq. (2.4) became 1; A , p and q were determined independently from tensile tests. When D for a volume element became 1 damage in the length was initiated and propagated until the mode II stress intensity range (computed using finite element methods) became lower than the mode II threshold. The loss in bending stiffness was predicted successfully as a function of cycles. Although the authors do not mention any relation between the two damage dimensions, depth and length, they do state that an observed scatter in fatigue lives is due to variability of the material with respect to cyclic tension and not to delamination.

The flexural fatigue of AS-4 carbon reinforced thermosets and thermoplastics was studied by Croman [25] to compare the performance of epoxy and J-polymer. For both resin systems damage initiated on the compression side. This was likely due to crushing under the central load point as the span to depth ratio was only 16:1 and large bearing stresses may have been introduced. In the epoxy specimens delamination followed the crushing which was followed by complete fracture. In the thermoplastic specimens no delamination was observed, only fracture into two pieces. From the results of Beaumont and Phillips [12] on tensile specimens it appears that superior bonding in the J-polymer caused this type of behaviour. However, in independent tests by the same author, the J-polymer was found to have a critical energy release rate eight to ten times higher than the epoxy and it is not clear that either specimen showed any notch sensitivity. Thus the absence of delaminations in the J-polymer reinforced beam was attributed to the greater energy required to grow delaminations.

The Charpy impact test, essentially a high strain rate three point bend test, was investigated by Bader and Ellis [26]. They found by varying the span to depth ratio that failure was by compression at high span to depth ratios and by delamination at low span to depth ratios. Very short span to depth ratios are used in interlaminar shear strength tests and failure is usually by delamination. This is likely related to the increased shear stress (related to load) to in-plane stress (related to product of load and span) ratio; the shear strength is exceeded before the in-plane strength at shorter spans. Longer span to depth ratios likely sustained some combination of compression and crushing damage, similar to [25].

Han and Koutsky [27] also studied the interlaminar fracture energy of glass fibre reinforced epoxy, but with a tapered cantilever beam. They report a critical mode II energy release rate of 800 J/m^2 . They note, however, that viscoelastic and plastic energy dissipation can give higher G_c values.

2.2 Damage Measurement

Methods of measuring and assessing damage in composites vary from the simple to the sophisticated. The situation dictates whether measurement can be a visual inspection with aided or unaided eye, destructive in the form of residual strength measurement, or non-destructive in the form of residual stiffness, response to external input or change in level of acoustic or electromagnetic activity. In fatigue testing non-destructive measurements are required so that the post-investigation behaviour of the sample under investigation is not altered by the measurement.

2.2.1 Stiffness Reduction

The change in extensional stiffness of composite tensile specimens is non-destructive and has been correlated with the amount of damage to provide information on the state of the test specimen. In composites the value of stiffness, or more generally deflection as a result of applied load, often relates quite directly via strength of materials and fracture mechanics concepts to the damage state. This is superior to electromagnetic or acoustic methods where the connection between material response and damage state is complex and perhaps computationally unfeasible.

For example, in the work of Poursartip [30] the increase in compliance was used to establish an energy release rate G which was then used to characterize damage growth by a power law correlation of the form $dD/dN = C\Delta G^n$. The method of measuring stiffness

reduction during fatigue involves halting cycling and loading the sample quasi-statically while recording load and deflection or strain. The effect of one cycle at a slow strain rate over many thousands of cycles may be considered non-destructive provided the maximum cyclic load is not exceeded.

Another example is provided by O'Brien [19] who quantified the effect of edge delamination on laminate stiffness. A delamination redistributes stresses in a laminate and may influence strength and life as well as stiffness. From laminated plate theory an undamaged laminate has an extensional modulus

$$E = \frac{1}{A'_{11}t} \quad (2.5)$$

For a laminate containing one or more complete delaminations the extensional stiffness can be computed as the sum of the individual sublaminates divided by the total thickness

$$E^* = \frac{\sum E_i t_i}{t} \quad (2.6)$$

For incomplete delaminations that extend in from the edges a distance a over a laminate width b the stiffness is

$$\hat{E} = (E^* - E) \frac{a}{b} + E \quad (2.7)$$

The delamination size in the case of incomplete delaminations was studied for a $[+/-30/+/-30/90/90]_s$ glass reinforced epoxy laminate.

Several authors have suggested that the formation of transverse cracks in 90 degree plies reaches a uniform spacing which depends on ply thickness and applied load. The spacing increases as load increases until a saturation density is reached. An attempt to quantify the effect these cracks have on laminate stiffness has been attempted by Highsmith and Reifsneider [31]. In cross-ply laminates these authors observed that the crack spacing reached a uniform density under static and fatigue loading. A shear lag model was developed to predict the stiffness loss due to these cracks, but overestimated the stiffness loss.

2.2.2 Acoustic Emission

Besides measurement of residual mechanical properties (stiffness, strength), most damage measurement methods in composites may be classified as electromagnetic (visual inspection, radiography thermography, holographic interferometry, microwave attenuation) or acoustic (ultrasonics, natural frequency, acoustic emission). Where broken fibres are present, a qualitative visual inspection may suffice. Crack length measurements in laboratory tests may be measured quantitatively with a travelling microscope or with radiographic methods by injecting X-ray absorbing dye into a crack. Minute changes in surface temperature, caused by heat generated from friction between crack planes or from an external heat source, have been related to defects which alter thermal conductivity. Holographic interferometry has been successful in quantifying size, shape and orientation of defects very reliably and accurately. Attenuation of microwaves by internal damage in composite plates has been shown to give an indication of damage severity and location. Internal damage such as delaminations or voids can be detected by exciting the test object with an ultrasonic probe and receiving and processing the reflected or transmitted acoustic

signal. Qualitative indications of part integrity have been achieved by tapping the object in question with a solid object, such as a small hammer or coin, and listening for a certain audible response.

Some of these methods, particularly radiography and ultrasonics, are well understood and are used routinely for quality control, periodic inspection and fracture mechanics research. Other methods are fresh ideas at the forefront of NDE technology which will lead to an elevated level of competence in assuring material integrity at the manufacturing stage and in service. In particular, the emerging technology of *acoustic emission* (AE) has received widespread attention in recent years. Though similar to ultrasonics, AE has some potentially significant advantages, chiefly the ability to detect and locate flaws before they become of a threatening nature.

In its simplest form acoustic emission monitoring is a method of detecting transient mechanical waves generated by abrupt localized changes in strain within a body, locating the source of these waves, and correlating the observed parameters of these waves with the source or mechanism which produced them. A well known example is the cry of tin, the audible noise produced by crystal twinning when tin is deformed. Plastic deformation, crack initiation, crack growth from fatigue or corrosion and the deterioration of composite structural components all give rise to acoustic emission signals. Since the technique is scarcely 30 years old applications have been limited by its lack of reliability. In spite of this there is intense interest surrounding the subject. The unique ability of the method to provide continuous monitoring of a structure is largely responsible for this interest. Some obvious examples of structures that would benefit from continuous monitoring are offshore

oil rigs, nuclear reactors and, where composites are concerned, pressure vessels and aircraft. In spite of fervent research activity, however, the technique remains at the development stage.

The history of AE dates back to 1948 when workers at the Bell Telephone Laboratory used piezoelectric transducers to monitor crystal twinning. In the early 1950's Josef Kaiser made a systematic investigation of emissions from metallic and non-metallic materials. He is credited with the discovery of the Kaiser effect. When crystals are stressed while emissions are being monitored and the stress is relaxed, no new emissions occur until the previous highest stress is reached.

Today AE equipment is commercially available. The equipment is tailored to specific needs such as proof testing, in service monitoring and fracture research. A laboratory system typically consists of four channels which detect and record acoustic emissions independently. Analysis of the stored information is made possible by a microcomputer following data acquisition. Industrial systems may have many more channels. The emphasis is placed more on location of sources than on analysis of AE data. Systems are available for such diverse applications as proof testing of pressure vessels and underground pipes, certification of FRP man lift booms, weld monitoring, in-flight detection of major cracking and inspection of bridges, rocket motor cases and launch structures.

Background

Acoustic emission belongs to the class of NDE methods for composites known as acoustic methods (ultrasonics, acoustic emission and some similar techniques). In general any method where the transmission or detection of elastic waves is involved may be termed acoustic. The technology surrounding AE is similar in nature to ultrasonics where it is essential to accurately record and detect high frequency pressure waves. Though the precise mathematical description of acoustic emissions is complex the basics of wave propagation in solids has contributed to its understanding. A more complete background to wave propagation and detection is contained in Appendix A.

As mentioned previously, acoustic emissions are the generation of transient elastic waves by a rapid release of strain energy from a localized source from within a material. The problem of transient waves travelling in anisotropic solids has only begun to be solved. In an article by Pao [32] the generalized ray theory is presented as a means of analyzing acoustic emission signals. Unfortunately the theory has not been developed for orthotropic materials and may prove too complex for large numbers of emissions. Therefore an accurate description of the conduct of acoustic emissions in composites is unavailable for quantitative damage measurement. It is instructive, however, to realize the following points regarding propagation of acoustic emissions:

- A single acoustic emission may travel at four different speeds along a very complex path from source to receiver.
- A signal may be changed significantly along its path from source to receiver. Reflections and refractions at interfaces and free surfaces cause the waves to travel along a path which is not necessarily a straight line between source and receiver. Along this path waves are attenuated, or reduced in strength, by interacting with material boundaries.
- A single signal may be detected more than once. Waves may both reflect and refract at the same interface, causing multiple waves to propagate at different speeds and arrive at different times at the same receiver.

Rather than pursue the theoretical aspects of wave propagation, the usual approach in AE testing is to analyze each recorded AE signal or event. Acoustic emission events have been classified as either "burst" or "continuous". Burst emissions are those which are well enough separated in time to appear as discrete signals. Continuous emissions are essentially bursts which occur so close together, perhaps overlapping, that they cannot be resolved.

Unlike a transient recorder, acoustic emission equipment does not record and store complete waveforms. Instead, five parameters of each detected waveform are stored. Figure (2.2) shows an AE waveform. The five parameters are the amplitude, duration, energy, counts and rise time.

The magnitude or sound pressure of an acoustic wave is an important parameter in acoustic methods. This quantity is difficult to measure so the relative sound pressure or amplitude is normally used, defined as

$$Amp = 20 \log \frac{P}{P_0} \quad (2.8)$$

where P is the detected sound pressure and P_0 is the minimum or threshold sound pressure. The quantity P is measured with a transducer, a device that converts a small surface deflection into a voltage. The value P/P_0 is assumed to be proportional to V/V_0 , the induced and threshold voltages of the transducer. V_0 is customarily taken as 1 micro-volt.

The duration of an AE event is measured as the time between first and final penetration of a pre-set threshold. The threshold is set electronically at a constant amplitude, typically 60 dB.

Similar to duration, the rise time is measured as the time between first penetration of the threshold and maximum amplitude.

The number of counts in an AE signal is the number of times the signal exceeds the threshold value. A single event may have any number of counts from one or two to several hundred.

Energy analysis is done by integrating the voltage-time signal of an AE event electronically. If the sensor response is proportional to the surface displacements associated with the passing of a stress wave, then the electrical energy in the sensor is proportional to the mechanical energy in the stress wave [33]. Values reported as "energy", then, are not absolute values, but are (linearly) proportional to stress wave energy. If the assumptions regarding sensor response and surface displacement are true then processes releasing high amounts of strain energy should have higher energies than processes releasing smaller amounts of strain energy.

From figure (2.2) it should be noted that signal amplitude is the only one of the five parameters that is independent of the threshold setting.

Previous Work

The initial development of AE in the 1950's focused primarily on metals. Even minute amounts of plastic deformation or crack propagation can cause motions on the surface of a body large enough to be detected by a transducer. It was realized that emissions were generated in metals by dislocation motion, grain boundary sliding, twinning, phase transformations and crack growth. Two broad areas of AE application in metals are weld monitoring and fracture monitoring. In welding, monitoring by AE is divided into in-process monitoring and post-weld monitoring. Many authors have shown that cracks in welds can be easily and reliably detected, with excellent correlation between AE activity and weld strength [34]. This applies to arc and spot welding. The absence of background noise from slag cracking and the electric arc makes post-weld cracking even easier to detect. In both in-process and post-weld monitoring the location of weld defects can be found using source location algorithms built in to the monitoring equipment.

The unique ability of AE to detect and locate flaws as they initiate and grow has led to its widespread use in fracture mechanics research in metals. Typical examples are empirical relations between AE amplitudes and crack growth rates in two different steels [35], AE count rate and rate of increase of plastic zone volume, AE energy release rate and J-integral [36].

In composites there is a multiplicity of possible AE sources. Matrix cracking, matrix splitting, debonding, fibre fracture, pullout and post debond friction have all been shown to

generate AE. The volumes of research on AE from composites are varied and extensive, a testament to its promise. Methodologies of damage assessment may be divided into three categories: wave propagation, empirical approaches and proof testing.

Wave Propagation

Though a great body of literature exists on AE from composites, much of the work is empirical in nature. During the early applications of AE the technique was used with little appreciation of the physics of wave propagation and detection. As a consequence some extravagant claims were made which led to some later disillusionment. Towards the end of the 1970's the theory began to develop which has helped to remove the mystique which once surrounded the subject. The article by Pao [37] summarizes some of the principles of AE, particularly source mechanisms, signal dispersion, and source characterization.

Source mechanisms can be modeled by combinations of six dynamic nuclei of strains. The signals which propagate from these sources are distorted by viscous damping of the material, scattering by inhomogeneities and reflections and refractions at interfaces. The displacement of a point on the surface of a layered solid due to one of the above sources can be predicted by the Theory of Generalized Ray. From the generalized ray theory a measured response may be deconvoluted to determine the nature of the source. Cases such as infinite plates are numerically complex and more realistic geometries have not yet been attempted.

Along similar lines Michaels et al [38] attempted to characterize AE sources in steel plates. In an attempt to uncouple effects of structure and recording system on the AE signals, these workers modeled the AE system as a convolution of a source function, structure function and recording system function using the above theories of acoustic

emission and generalized rays. Deconvolution was used to find the source function once the system and recording functions were known. The plates tested were sufficiently large that infinite plate results were applicable. Results for three artificial AE sources (glass capillary fracture, pencil lead fracture and ball impact) showed good agreement with their expected source functions at various plate positions. Results for non-infinite plates or laminated plates are not available. Although this work is an important first step in understanding AE, the complexity of wave propagation in realistic structures has to date forbidden detailed analysis.

Empirical Approaches

Although wave propagation may some day provide a rigorous connection between AE sources and received AE signals, the complexities of the analysis have to date spawned a more empirical approach. Many authors have used the five AE parameters (amplitude, duration, energy, counts, rise time) from data collected during static or fatigue failure of composites or their constituents in attempts to identify distinct failure modes. Typically a composite specimen is loaded quasistatically or by cycling and acoustic emissions recorded. The data is then analyzed after the test in attempts to distinguish failure modes and track damage progression.

There has always been some hope that analysis of signal amplitudes alone could be used to distinguish failure modes for a given composite. Table 2.1 summarizes the work of several authors who have characterized failure processes in CFRP specimens using AE amplitudes.

Table 2.1 Characterization of Failure Modes in CFRP by AE Amplitudes.

Specimen	Test Geometry	Failure	Amplitude	Reference
unidirectional	tension	matrix crazing	<50	[39]
unidirectional	tension	fibre break delamination rapid delam. friction	<50 50 - 70 >70 40 - 50	[40]
unidirectional	tension	matrix crazing fibre break	25 40	[41]
unidirectional	flexure	matrix crack fibre break	20 - 30 40 - 65	[42]
unidirectional	DCB	delamination	70	[43]
cross-ply [0 ₂ /90/0] _s	tension	fibre break matrix crack delamination	70 40 - 70 40 - 70	[44]
cross-ply [0/90/0] _s	DCB	delamination	75 - 88	[45]

Although the above results do not contradict one another they are qualitative in nature and cannot be used confidently with other materials or to assess the severity of the damage state. In studies on Kevlar, Hamstad and Moore [47] conclude that even for a single source mechanism (Kevlar filament break) there is considerable variation in AE parameters, especially energy. Even though individual filament breaks within bundles could be identified, the load at which failure occurred did not correlate with event peak amplitude.

Using more than one of the five AE parameters can lead to more confidence in establishing damage mechanisms with AE, but the results are still only qualitative. One

[40] has used amplitude and duration values to identify failure processes in CFRP. After 44 tests on unidirectional specimens he concluded from careful examination of loading curves, failure modes and AE that damage processes could be characterized as in table 2.2.

Table 2.2 Characterization of Damage Processes using AE Duration and Amplitude.

Damage	Duration	Amplitude
fracture	<100 μ s	<50 dB
delamination	120 μ s	50 - 70 dB
rapid delamination	>200 μ s	>70 dB
splitting	100 μ s	
friction	<150 μ s	40 - 50 dB

Also using amplitude and duration Gorman and Rytting [48] find that in CFRP angle ply coupons long duration (up to 4000 us) and high amplitude (80-90 dB) events occur at 65% of maximum load. These were found to correspond to matrix or intraply cracking. Events at higher loads were found to have lower amplitudes and durations.

A quantitative relation between AE and damage state was studied by Fitz-Randolph et al [46] who observed that each fibre failure in boron reinforced epoxy was accompanied by the same number of emission counts. A simple correlation was then made to measure the number of fibres breaking during loading. This correlation is based on previous correlations between increase in compliance and electrical resistance with increase in the number of broken fibres.

Monitoring fatigue damage with AE presents some difficulties because considerable amounts of data may be collected, only a small portion of which may be meaningful. Awerbuch et al [49] discuss the merits of AE in determining fatigue damage initiation and progression in unnotched and double edge notched laminates. One reason for using AE

rather than radiography or ultrasonics is to avoid interrupting the test; interruption may affect the fatigue results. They find most of the emissions are from damage progression during the initial part of loading, that is, the first few cycles. After continuing cycles the emissions are mostly from friction among fracture surfaces created by matrix cracking and delamination. Qualitatively they distinguish between emission generated by friction between fracture surfaces and fatigue damage progression. They attempt to eliminate friction noise but at the same time acknowledge that damage can occur so fast as to be missed by the recording equipment, leaving an increase in friction noise as the only clue that damage has occurred. To this end they try to distinguish friction noise from other emissions rather than eliminating it. Friction noise was picked out by plotting event rate versus cycles for the arbitrary load ranges 60-100, 80-100 and 95-100% of P_{max} . A very low event rate is observed. The lower load ranges, 10-60, 10-80 and 10-95% of P_{max} show a rapid increase in event rate following matrix cracking. This jump in event rate is attributed to the increase in friction noise at low loads following the creation of new fracture surfaces. From this the precise cycle number where a sudden increase in damage occurred was determined. Unfortunately, using this method one cannot remove all friction events from the data set and analyze what is left because damage growth events may not have been recorded.

Echles and Awerbuch [44] have made further attempts to separate AE from friction. Friction events during cycling of double edge notch cross ply GFRP are excluded following a post-analysis. The left over events are used to monitor damage progression in terms of events versus cycles. Here they admit that even the high load ranges may contain friction events. They assign "thresholds" below which all events can be considered friction. For instance all events recorded with duration <180 us, energy <15 , counts <35 and located within 20-80% of the gage length are assumed to be friction. The remaining events are

used to create a "derived damage" curve, events versus cycles. This curve shows the intermittent nature of damage growth, although no specific source mechanisms are defined. The end result, following a post-test analysis, is that fatigue damage initiation can be detected and located with AE, AE may be generated by friction and new damage, and friction noise may be separated from damage progression events.

AE has been applied to impact by Ghaffari [50]. Normally C-scan or radiography is used to detect delaminations, intraply cracks, matrix splitting and fibre breakage which occur during impact. AE can provide information on damage initiation and growth during loading. During post-impact quasi-static loading AE is generated from friction between fracture surfaces. This friction AE is used to detect and locate the damage.

A new method of monitoring damage with AE has been proposed by Mitchell and Miller [51]. Termed acousto-ultrasonics the method makes use of ultrasonic testing techniques using AE equipment. A simulated AE source is pulsed into the sample by a probe (a transducer run backwards) and detected by the same apparatus used to detect AE. The character of the received signal is observed to change as the input signal passes through damaged and undamaged areas. The advantage over conventional AE testing is that the character of the source does not change, making interpretation simpler. Important considerations for propagation of a stress wave into a composite by a broad band transducer are given as frequency content, anisotropy, beam spreading, absorption, transducer contact and coupling. Impact damaged glass/epoxy cylinders were monitored in this way. The results show that impacted areas are effectively spotted by reduction in amplitude and increase in propagation time over impact areas. For these tests the transducer and pulser were mounted side by side normal to the surface. The result is a

reliable method to confidently detect non-visual impact damage requiring one operator. Many of the advantages of AE are lost, however, such as real-time indication that damage is occurring and source location.

Proof Testing

The increased use of FRP tanks in the chemical industry during the early 1970's was overshadowed somewhat by a significant number of FRP tank failures. As the industry evolves from non-critical FRP storage tank applications to pressure vessels and process applications satisfactory and reliable NDE methods for certification and monitoring are required. DuPont, Monsanto and Owens Corning were among the first to show that AE could be used effectively in this role. In 1970 the Society of the Plastics Industry Committee on AE from Reinforced Plastics (CARP) was formed to develop standardized test procedures. Today the committee has issued recommended practices for testing reinforced plastic tanks and pipes. These methods have been adopted for aerospace and automotive industry use. ASTM, ASME and API are also developing standards for AE testing of composites.

In 1982 the SPI published the first CARP Recommended Practice for Testing Reinforced Plastic Vessels [52]. Other organizations have modified this practice in devising their own standards. In fact one ASME code requires a mandatory AE test on one-of-a-kind RP vessels before they are put into service. The use of AE in testing RP vessels is widely accepted. As many as 7000 tank and vessel tests have been run [53]. PAC/Dunegan Inc., one of the major AE equipment suppliers, has, with Monsanto, developed a system to alert personnel to cracks, areas of corrosion and overstress and tell the severity of the problem. The technique is based on results of tests on over 2500 RP vessels by Monsanto. The procedures are apparently clear and reliable.

One year after its recommended practices for testing RP vessels CARP introduced a similar standard for RP piping [54]. The emphasis is on quality control and acceptance testing of downhole tubing (up to 4000 psi) and high pressure pipe. Here as many as 10,000 pipe tests may have been performed. The practice provides guidelines for AE examination and monitoring of reinforced thermosetting resin pipe to determine structural integrity of lined or unlined pipe, fittings and joints at pressures up to 34 MPa (5000 psi) and 610 mm (24 in) in diameter. In short, the practice consists of subjecting RTRP to increasing or cyclic pressure while listening for AE from growing defects. Methods to assess the location and severity of defects are given. Acceptance criteria are based primarily on AE event rate at constant proof loads (to 110% of maximum pressure) and the Felicity ratio (stress at onset of AE / previous maximum stress). Pressurization is done in five increasing steps with pressure held at constant values for four minutes between steps while monitoring AE.

Aerial personnel lifting devices (commonly known as bucket trucks, such as those used by electrical utilities to service overhead power lines) containing FRP manlift booms have proven to be one of the biggest applications of AE. In general the procedures are similar to those used for tanks, vessels and pipes, with special attention paid to joints. As many as 50,000 boom tests may have been conducted in the course of recertifying bucket trucks [54].

Development of AE test techniques for composites in aerospace applications has been discussed by Whalley and Cole [55]. These authors suggest that for AE to be useful in these applications it must:

- 1) determine at what load damage occurs
- 2) determine the severity of the damage
- 3) determine the residual strength of the structure
- 4) locate the damaged area
- 5) identify the damage

Unlike pipes, vessels and booms an indication that damage is occurring and its location is apparently inadequate. The ability to quantify the emissions to exact locations, to assess the type of damage and to know the loading conditions under which each source of AE becomes active offers numerous advantages. Where location is concerned, the high signal attenuation in composites necessitates many transducers to accurately locate sources of emissions. Also in many composite structures the wave velocity has large variations. The arrival times have an error due to the irregular acoustics of, say, a wing structure. This is due to variations in stress wave velocity in a composite structure. Both of these problems, attenuation and variations in velocity, are reduced in magnitude by more sophisticated software and sensor arrays. Attenuation was mapped over a wing structure by measuring detected amplitudes from a repeatable source at varying locations. Depending on the underlying wing structure attenuation ranged from 11 to 29 dB over 10 cm. Similarly wave velocities varied from 500 cm/s to 730 cm/s. Since most planar location algorithms are based on a unique wave propagation velocity location accuracy would be greatly reduced. From the attenuation and wave speed results the authors selected a transducer array that minimized location error. On a 5 m long wing structure with 28 sensors simulated AE sources were located with an error better than 5 cm.

Similarly workers at Rolls Royce [56] began a program of verifying integrity of CFRP aircraft engine nacelles. These workers identified location, characterization of wave

propagation, minimizing cost of hardware and simple interpretation of output as important aspects. They also noted that signal attenuation made location difficult. These workers had success with an attenuation mapping technique using a scanned gas jet as a calibration source and many transducers. Once the attenuation characteristics of a structure were known, optimum transducer frequency and position were determined.

2.3 Summary

In summary, it seems possible to apply concepts of fracture mechanics to mode I and mode II cracks growing parallel to the fibre direction in unidirectional laminates. Critical energy release rates are shown in table 2.3. High measured values can be attributed to fibre bridging, and viscoelastic and plastic energy dissipation.

Table 2.3 Comparison of Critical Energy Release Rates of Metals and Glass/Epoxy.

Material	$G_c(J/m^2)$	Geometry	Reference
4340 Steel	10,750	CCT	[28]
7075-T651 Aluminum	12,150	CCT	[28]
Glass/Epoxy	800	Tapered Cant. Beam	[27]
	878-1020	Double Cant. Beam	[29]
	472-1122	Compact Tension	[15]
	163	3-pt Bend	[16]

In the case of fatigue, delamination growth has been singled out as a potentially hazardous form of subcritical damage. Applications of the Paris Law involving energy release rate range (ΔG) have been successful in describing delamination growth.

The specific case of bending has not received widespread attention. Damage in static or cyclic flexure has been shown to occur as some combination of fibre failure, delamination or crushing. In general there seems to be at least two damage parameters: a damage depth (either from crushing or buckling or compressive or tensile failure) and a delamination length.

Stiffness reduction has been used in the laboratory as a measure of the damage state of composite specimens. The reduction in stiffness over the duration of a fatigue test may be as high as 40%. As a NDE technique it is effective when the stiffness measurement can be interpreted accurately as a function of the material's state of damage.

The major advantage of AE over other acoustic or electromagnetic NDE methods is its ability to monitor a structure continuously. Other methods require some form of energy input to the test object and are therefore intermittent in nature. This gives AE the unique ability to act as an early warning system. Applications exploiting this characteristic have typically involved qualitative indications of damage initiation and growth.

The five independent parameters of discrete AE events have lead many fracture mechanics researchers to attempt to distinguish failure modes in composites using AE. Because no precise mathematical relationship between AE source mechanisms and recorded AE signals exists most investigators use empirical approaches. As yet no methods have been developed which can distinguish failure modes from AE waveform parameters for a variety of materials. Awerbuch [44,49] has had some success in monitoring fatigue damage growth. Noise from damage growth and friction between damaged surfaces has been separated but the somewhat arbitrary methods are tedious to apply.

For AE to be accepted for general use in inspection of composite structures it must be able to locate damaged areas and determine the severity of the damage. Careful accounting of wave attenuation and speed variations coupled with sophisticated location algorithms and sensor arrays has led to successes in locating damage in aerospace structures. Fitz-Randolph et al [46] are among the few investigators to quantify the damage state of a composite using AE. A new technique, acousto-ultrasonics, may hold promise for quantifying the damage state of a composite. An AE sensor is run backwards, analogous to an ultrasonic probe, and changes in a simulated AE signal pulsed through an object have been related to the damage state of the object.

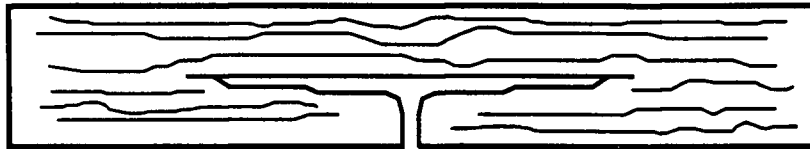


Figure 2.1 Failure of clear Douglas Fir parallel to the grain, three point bending. (from Bodig and Jayne [28])

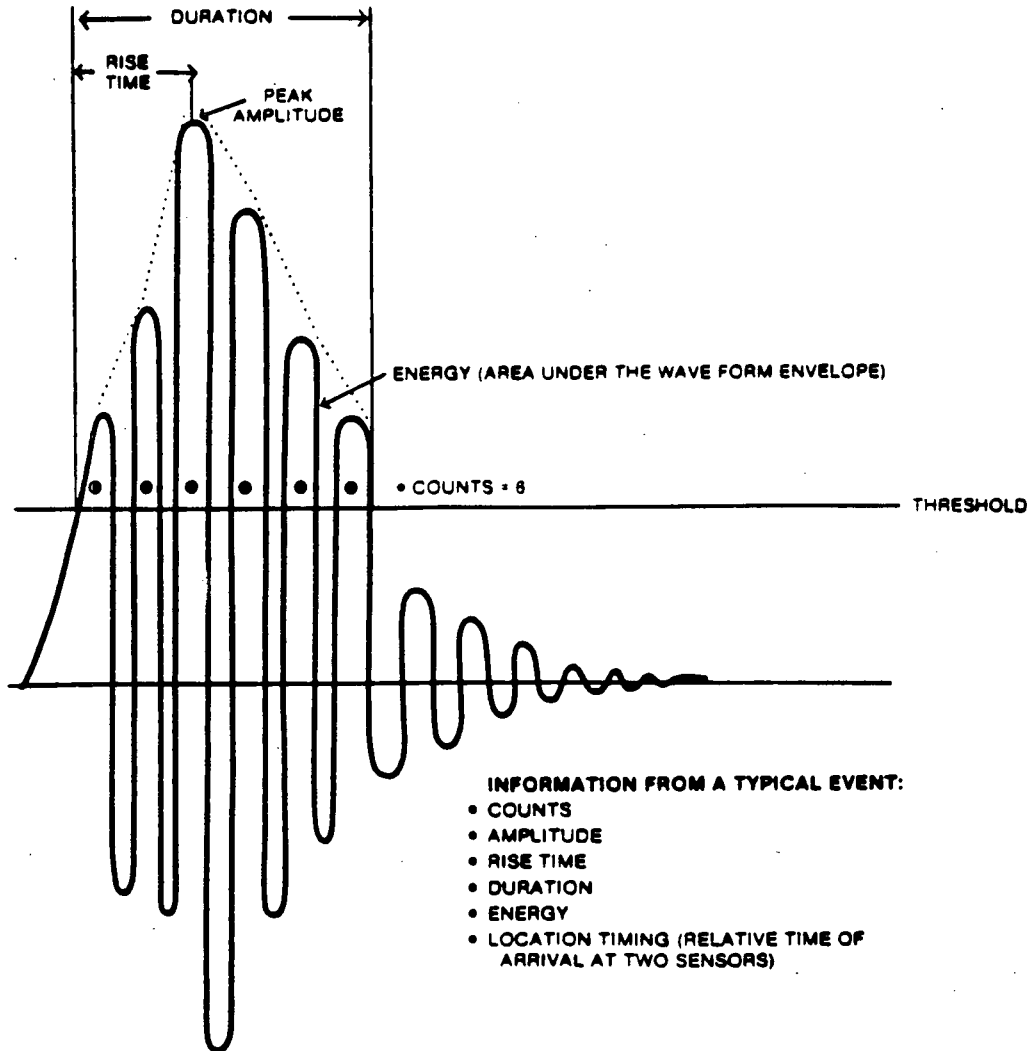


Figure 2.2 Typical acoustic emission waveform (Amko service Corp., Testing Div., Form AEB 185500)

3 FRACTURE AND FATIGUE OF UNIDIRECTIONAL COMPOSITE BEAMS

In this chapter the behaviour of circular cross section fibreglass rods in static and constant amplitude cyclic three point bending is investigated. Three types of commercially available 16 mm diameter glass reinforced plastic rods were chosen as test specimens. The circular cross section is favorable in three-point bend testing because the maximum stress is always concentrated at a single point on the tension side directly beneath the central load point, ensuring consistent initiation behaviour during cyclic loading. All three rod types were made with E-glass fibres but with a different matrix material. The first type was made with a filled polyester resin, the second with polyester resin and the third with epoxy resin as outlined in table 3.1. All three rod types were manufactured by the pultrusion process in which the resin wets the reinforcement as it feeds into a die that forms the circular cross section. The pultruded rods were obtained in 3 m sections and cut to 600 mm lengths for testing.

Table 3.1 Rod types.

Rod Type	Matrix	Fibre Volume Fraction (%)
I	Filled Polyester	57
II	Polyester	60
III	Epoxy	57

3.1 Experimental Procedure

Figures 3.1 (a) and (b) show the experimental setup. The span of the three-point bend jig was set at either 400 or 480 mm. Hence the minimum span to depth ratio was 25:1

which minimized deflections due to shear [58]. A special fixture was fabricated to apply the load at the centre of the span, figure 3.1 (b). This was necessary to avoid crushing on the compression side caused by a conventional half inch diameter steel pin, particularly during cyclic loading.

All samples were tested in an MTS servohydraulic fatigue machine under load control. Loads were measured with a 10 kN load cell and deflections with a linear variable displacement transducer. The operation of these devices is described in reference [59].

For the static tests the function generator on the MTS control panel was used to generate a ramp output. The load and displacement data were recorded using two channels of an Orion data logger and later downloaded to an IBM PC for analysis. For these tests the initial load versus deflection curve was measured which gave an initial value of compliance (ratio of deflection to load) for the undamaged sample. A shallow notch was then cut with a jewel saw on the tension side beneath the central load point. The load versus deflection curve was measured again, on three consecutive quasi-static cycles. The notch was deepened or the load level raised for subsequent cycles until the compliance had increased significantly.

For the cyclic loading tests the MTS was computer controlled to generate a sine waveform to control loading at the desired frequency. These tests were carried out at various load ratios with a maximum load corresponding to approximately 80% of the breaking strength. As the long span necessitated a long travel of the hydraulic ram, cycling was done very slowly, around 0.3 Hz. Compliance measurements were made by interrupting the test automatically, unloading the sample and reloading slowly to a predetermined load, during which the load and centre span deflection was measured and recorded by the

computer. These measurements were taken at roughly 200 cycle intervals in all the tests, with an average of 25 readings per test. The data was later transferred to a spreadsheet program for analysis.

In all tests a damage zone developed which was recorded by measuring its length and depth. Although the damage zone was easily visible with the unaided eye its accurate measurement was important. The damage length ranged from zero to 400 mm and was simple to measure with a set of calipers. The damage width was measured with a set of calipers directly beneath the central load point. For a cross section of radius r the damage depth d was calculated from the damage width b according to (see Appendix B)

$$b = 2\sqrt{2rd - d^2} \quad (3.1)$$

For example, at a damage depth of 0.1 mm the width was 2.5 mm and for a damage depth of 3 mm the width was 12.5 mm. Attempts to measure the depth directly with a travelling microscope were unsuccessful due to difficulties in focussing on the curved surface of the rod and to slight rotations of the rod about its longitudinal axis as it was removed and replaced for deepening the notch.

3.2 Results

From a previous study involving this same material in bending [60] it was consistently observed that a damage zone developed on the tension side after several loading cycles. Without exception this damage zone grew in two directions: in the depth direction as an increasing number of fibres broke beneath the central load point and in the length direction as the broken fibres split parallel to the longitudinal axis. For all samples tested in the present study a similar broom-like damage zone was observed. This consisted of broken fibres at the central load point on the tension side and longitudinal splits growing

outwards from the central load point in the longitudinal direction on the tension side. Thus the damage zone could always be measured in terms of a damage depth and a damage length. This broom-like fracture zone is shown in figure 3.2 (a) and schematically in figure 3.2 (b).

In the past other authors have documented this same type of damage growth [23-25]. The fracture of Douglas Fir beams, rectangular and circular cross section beams, automotive leaf springs and Charpy impact specimens has involved damage growth perpendicular and parallel to a beam longitudinal axis. In the case of flexure, damage growth in the depth direction has been observed either on the compression side as crushing or buckling or on the tension side as fibre breaks. In the case of impact, damage has resulted from crushing on the compression side. In any case damage growth in the length direction occurred after damage had occurred perpendicular to the longitudinal axis.

3.2.1 Fracture

Although two damage directions were apparent in all the rods tested the entire damage zone may or may not be characterized by two measurements. Two measurements, a length and a depth, will be adequate only if the damage depth is constant along the entire damage length. If this is not the case then more than two parameters may be required. To confirm the existence of only two damage parameters static tests on the three rod types were done under load control on the MTS machine.

Type I Specimens

For two type I rods, one at a span of 400 mm, one at a span of 480 mm, testing proceeded as follows: after measuring the initial compliance of the specimen, a notch was cut at the centre of the span on the tension side. The load was ramped three consecutive

times while monitoring load and deflection. On the first cycle a longitudinal split grew from the notch root in the length direction towards the outer load points. The damage length was nearly equal on both sides of the central load point. A slight amount of growth was observed in the length direction on the second cycle and almost none on the third cycle. On completion of these three cycles a deeper notch was cut by increasing the depth of the first notch. The three load cycles were repeated and on the first cycle the length grew to a new and longer length at the new depth. Slight growth in length was observed in two subsequent cycles. This was repeated two or three more times for each test until the sample broke in half. As the longitudinal split grew in length, regardless of depth, fibres could be seen bridging the crack from the top crack surface to the lower one, especially towards the longitudinal extent of the split. The horizontal plane of the longitudinal crack was smooth and uniform at the centre notch but became rougher towards the crack tips.

Visual inspection of the two samples at each new notch depth revealed that the depth was constant over the entire damage length. One of the rods was sectioned every 40 mm along its length to investigate the damage profile, figure 3.3. At each cross section it can be seen that the depth of damage is constant from the centre of the span out to the full extent of the damage length.

As the length and depth increased the compliance increased as shown in figure 3.4 for the specimen at the 480 mm span. Corresponding to the figure, values of length, depth and compliance are shown in table 3.2. For a small amount of damage the compliance increased only slightly. When the depth, and correspondingly the length, became large the compliance increased more quickly.

Table 3.2. Damage length, depth and compliance, static test.

Length (mm)	Depth (mm)	Compliance (mm/N)
0	0	0.0180
25.8	0.52	0.0185
85.8	2.22	0.0244
105.0	2.85	0.0304

Type II Specimens

The static test procedure was modified slightly for one type II and two type III rods. For the type II rod the initial compliance was measured and a notch was machined into the tension side at the centre span. The load was ramped to a pre-set level and released. Upon reaching a certain load, less than the pre-set maximum load, a smooth and uniform split grew longitudinally from the notch root. On each of three loading cycles the compliance and split length were recorded. The load level was raised and the three ramps were repeated. Each time the load level was increased the longitudinal split extended and the compliance increased. As the length increased a significant amount of fibre bridging was observed where fibres crossed from the top to bottom surfaces of the crack plane.

Type III Specimens

For two type III rods the depth of the machined notch was made different. In both rods the span was 480 mm. The crack that grew longitudinally from the notch root was smooth and uniform at first. As the load level was raised and the split grew in length a significant amount of fibre bridging was observed. Whole bundles of fibres, perhaps 2 mm in diameter, could be seen extending from the top crack surface to the lower one. This seemed to have an effect on the length to which the crack grew. On the final load ramp of both tests the fibres bridging the longitudinal crack plane were cut away with a scalpel

while the specimen was under load. Although the crack could not be opened far enough to cut all the bridging fibres, the ones that were cut caused growth in the length direction of up to 8 mm.

The compliance increased for each damage length increase and was higher for the rod with the deeper notch at equivalent crack lengths. As for the previous rod types the depth remained constant over the entire length although the extensive fibre bridging action tended to roughen the surface towards the longitudinal extent of the crack.

3.2.2 Fatigue

Five type II and four type III rods were tested under constant amplitude cyclic loading. The tests are summarized in table 3.3.

Table 3.3. Fatigue test conditions.

Specimen	Type	P_{max} (N)	Load Ratio	Cycles	Compliance Increase (%)
A	II	2670	0.10	4900	47
B	II	2670	0.10	4600	47
C	II	2670	0.10	4700	49
D	III	2890	0.45	17400	16
E	III	3100	0.17	7100	49
F	III	3100	0.45	9200	34
G	III	3100	0.17	5040	39
H	II	2760	0.17	3200	56
I	II	2890	0.45	2400	35

In each case damage initiated after several hundred cycles. The first visual indication was matrix related damage in the form of small light colored spots on the tension side beneath the central load point. These spots grew and eventually a fibre break occurred at or

near the central load point. Coinciding with the fibre break was a longitudinal split heading outwards from the central load point in the direction of the two outer load points. Damage growth continued in this manner, in some cases to a 50% increase in compliance, with no sign of imminent failure. Thus there are at least two damage parameters, a depth and a length, as in the case of static loading.

Type II Specimens

Rods A ($R=0.10$) and I ($R=0.45$) represent the extremes of testing in terms of load ratio for the type II rods. A series of cross sections of rod A is shown in figure 3.5. The damage surface at the central load point (left section in photo) is flat and uniform. The damage surface in the remaining sections (sections cut every 30 mm toward the outer load point) gets progressively less uniform and is not damaged to the same depth, especially the last two sections. This is evidenced by the damage width which decreases with increasing distance from the central load point. Rod I showed the same type of behaviour, figure 3.6. At the central load point the damage surface is flat, as in sample A. Towards the outside the damage surface is less uniform, and again is most pronounced in the last two sections.

The damage length and width were measured at intervals of approximately 100 cycles. Damage depth (or width) and length increased as cycling progressed, but not at the same rate. The width at the central load point was the maximum and corresponded to the maximum damage depth. Figure 3.7 shows the cross sections at the central load points of the two type II rods in more detail. Measurement of the damage width was straightforward as the damaged section was very flat.

For rods A, H and I the damage length as a function of cycles is shown in figure 3.8. In all cases the length grew quickly after initiation then slowed considerably. The fibre

bridging action that was observed along the damage length during the static test on this same rod type did not appear as severe in the fatigue tests. The fibres tended to break and split in discrete bundles rather than as one large section as in the static tests, making the appearance of fibre bridging less obvious.

The depth as a function of cycles for rods A, H and I is shown in figure 3.9. In all cases the growth rate was nearly constant and was measured by fitting a linear regression line to the data. The growth rates in the depth direction for all five type II samples are summarized in table 3.4 below.

Table 3.4. Growth rate of damage depth, type II rods.

Sample	P_{max} (N)	P_{min} (N)	ΔP (N)	P_{mean} (N)	dd/dN (10^{-3} mm/cycle)
A	2670	270	2400	1470	0.924
B	2670	270	2400	1470	1.013
C	2670	270	2400	1470	0.840
H	2760	470	2290	1615	0.911
I	2890	1300	1590	2095	1.827

Experience with metals [61] would suggest that the growth rate of the damage dimension should increase with increasing load range. Just the opposite occurred in this case, indicating a dependence of growth rate on mean or maximum stress.

After an initiation phase the compliance began to increase, figure 3.10. Here all the compliance values have been normalized with respect to the initial compliance. As with the rate of increase in depth, the rate of increase in compliance was highest for rod I and

nearly the same for rods A and H. In all cases the compliance increased slowly at first, accelerating towards the end of the test. This is opposite to the damage length which increased at a decreasing rate towards the end of the test.

Type III Specimens

Two type III rods, G ($R=0.17$) and F ($R=0.45$), were sectioned after cycling and photographed, figures 3.11 and 3.12. Both photographs show that the damage zone is much rougher and less flat than either of the type II rods, even directly beneath the central load point (left sections in photos). As with the type II rods the damage depth decreased as distance from the central load point increased.

Damage length as a function of cycles for the two rods is plotted in figure 3.13. For both load ratios the damage grew in the length more quickly at the start of the test than at the end. Once again, as with the type II rods, fibre bridging along the crack length was evident.

Measurement of damage depth in these specimens was slightly less accurate than in previous tests as the damage surface was not as flat, figure 3.14. Figure 3.15 shows damage depth as a function of cycles for both rods. In the sample tested at $R=0.17$ the damage initiated after 1200 cycles and grew to a final depth of just over 2 mm. In the sample tested at $R=0.45$ the damage initiated after 2000 cycles and grew more slowly. In both cases the test was stopped when the damage depth reached 2 mm and there was no sign of imminent failure. As for damage length the growth rate was highest for the lower load ratio. The growth rate of the damage depth is summarized in table 3.5 for the four samples tested.

Table 3.5. Growth rate of damage depth, type III rods.

Sample	P_{\max} (N)	P_{\min} (N)	ΔP (N)	P_{mean} (N)	dd/dN (10^{-3} mm/cycle)
D	2900	1305	1595	2100	0.205
E	3100	527	2573	1810	0.486
F	3100	1395	1705	2250	0.238
G	3100	527	2573	1810	0.462

Unlike the type II rods, the growth rate through the depth increases with increasing load range.

Compliance as a function of cycles is plotted in figure 3.16. Both samples sustained approximately the same compliance increase, but the rate of increase was much higher in the sample at the low load ratio. The high load ratio tests were discontinued at the smaller changes in compliance because all samples were monitored with acoustic emission (see chapter 5) and the AE data gathered was proportional to the number of cycles. Longer tests would have exceeded the AE monitoring system's capacity.

3.3 Stiffness Reduction

From the above results it is clear that the compliance of each rod type increased as damage grew in length and depth. In the static tests the damage depth was constant over the entire damage length, with some roughening of the longitudinal crack surface due to fibre bridging. For the fatigue tests the damage depth was constant over most of the length, becoming shallower at the extremes of crack length, especially for the high load ratios.

Analysis of the damaged rod begins by considering only the left half, figure 3.17. This produces no loss in generality as the depth is assumed constant along the damage

length and in all cases the damage length was symmetric about the centre. The damage zone is assumed to carry no load and is therefore assigned zero stiffness. The cantilever beam is divided into two parts: one (damaged) part is of length a and has a cross section of diameter $2r$ with a sector of depth d removed; the other (undamaged) part is of length $(l-a)$ and has a circular cross section of diameter $2r$. The half-rod is treated as a non-uniform cantilever beam. From the theory of beam deflections [62] it is desired to find w , the vertical deflection of any point from its initial undeflected position, as a function of the longitudinal axis coordinate x . The deflection of the cantilever may be considered as the sum of the deflections of segment AB and segment BC if continuity is assured between the two segments.

For segment AB in figure 3.17

$$\frac{d^2w}{dx^2} = \frac{M}{EI_1} \quad (3.1)$$

where M is the bending moment, E is Young's modulus and I_1 is the area moment of inertia about the neutral axis of the undamaged cross section. By inspection of figure 3.17 the bending moment M along the beam is

$$M = Px \quad (3.2)$$

Integrating Eq. (3.1) twice with respect to w yields

$$\frac{dw}{dx} = \frac{Px^2}{2EI_1} + A_1 \quad (3.3)$$

$$w = \frac{Px^3}{6EI_1} + A_1x + A_2 \quad (3.4)$$

For segment BC in figure 3.17 the same moment M acts over a different cross section having moment of inertia I_2

$$\frac{d^2w}{dx^2} = \frac{M}{EI_2} \quad (3.5)$$

Integrating this expression twice yields

$$\frac{dw}{dx} = \frac{Px^2}{2EI_2} + B_1 \quad (3.6)$$

$$w = \frac{Px^3}{6EI_2} + B_1x + B_2 \quad (3.7)$$

The four constants A_1, A_2, B_1, B_2 are determined from two boundary and two continuity conditions. At point C in figure 3.17 $x = l$ and the deflection is zero. From Eq. (3.7)

$$\frac{Pl^3}{6EI_2} + B_1l + B_2 = 0 \quad (3.8)$$

Also at point C the slope is zero. From Eq. (3.6)

$$\frac{Pl^2}{2EI_2} + B_1 = 0 \quad (3.9)$$

$$B_1 = -\frac{Pl^2}{2EI_2} \quad (3.10)$$

Combining Eqs. (3.8) and (3.10)

$$B_2 = \frac{Pl^3}{3EI_2} \quad (3.11)$$

The remaining two constants are determined by imposing two continuity conditions. The slope and deflection must be continuous at point B for both segments AB and BC.

Equating deflections

$$\frac{P(l-a)^3}{6EI_1} + A_1(l-a) + A_2 = \frac{P(l-a)^3}{6EI_2} - \frac{Pl^2(l-a)}{2EI_2} + \frac{Pl^3}{3EI_2} \quad (3.12)$$

Equating slopes

$$\frac{P(l-a)^2}{2EI_1} + A_1 = \frac{P(l-a)^2}{2EI_2} - \frac{Pl^2}{2EI_2} \quad (3.13)$$

Solving these two equations simultaneously determines the coefficients A_1 and A_2

$$A_1 = \frac{P(l-a)^2}{2EI_2} - \frac{P(l-a)^2}{2EI_1} - \frac{Pl^2}{2EI_2} \quad (3.14)$$

$$A_2 = -\frac{P(l-a)^3}{3EI_2} + \frac{Pl^3}{3EI_2} + \frac{P(l-a)^3}{3EI_1} \quad (3.15)$$

The deflection measured in the experiments is the quantity sought. This corresponds to the deflection of the free end of the cantilever in figure 3.12. For $0 < x < (l-a)$

$$w(x) = \frac{P}{E} \left[\frac{x^3}{6I_1} + \left(\frac{(l-a)^2}{2I_2} - \frac{(l-a)^2}{2I_1} - \frac{l^2}{2I_2} \right) x + \left(\frac{(l-a)^3}{3I_1} - \frac{(l-a)^3}{3I_2} + \frac{l^3}{3I_2} \right) \right] \quad (3.16)$$

The free end is at $x=0$. Evaluating Eq. (3.16) at $x=0$

$$w(0) = \frac{P}{3E} \left[\frac{(l-a)^3}{I_1} - \frac{(l-a)^3}{I_2} + \frac{l^3}{I_2} \right] \quad (3.17)$$

The compliance C is defined as the deflection per unit load. Using Eq. (3.17)

$$C = \frac{1}{3E} \left[\frac{a^3 - 3la^2 + 3l^2a}{I_2} + \frac{(l-a)^3}{I_1} \right] \quad (3.18)$$

Derivations of the two area moments of inertia, I_1 and I_2 , may be found in Appendix B.

3.3.1 Comparison With Experiment

Using Eq. (3.18) the compliance can be predicted for the observed pairs of (a,d) and compared to the corresponding observed compliance from the static and fatigue tests. To be consistent with the cantilever beam representation in figure 3.17 the semi-span $L/2$ is

now substituted for the total span L . Likewise the measured load P will be replaced by $P/2$, the force acting at the end of the cantilever in figure 3.17 and the crack length $2a$ is replaced by the crack half-length a .

Comparison between the experimental and theoretical results for the two type I rods are shown in figure 3.18. Both axes are linear and cover the same range. The straight line represents ideal agreement between the calculated and measured compliance. Agreement is excellent and confirms that a strength of materials approach which ignores displacements due to shear, assumes that the damaged portion supports no load and that the damage depth is constant along the damage length is adequate for this specimen type. The predicted values are from Eq. (3.18) and the modulus E was calculated from the initial compliance with a and d taking on zero values which reduces Eq. (3.18) to the cantilever beam equation

$$E = \frac{Pl^3}{3wI_1} \quad (3.19)$$

One type II rod was tested at one single notch depth. Increasing load levels caused growth in the length direction, increasing the compliance. Thus the same depth at a series of increasing lengths was used as input to Eq. (3.19). The comparison with measured compliance is shown in figure 3.19. Again the straight line represents ideal agreement between measurement and prediction. At longer lengths the model has underestimated the compliance; thus the rod is slightly less stiff than the model would predict.

Two type III rods were tested similarly, at a semi-span of 240 mm, but at two different depths. The results of both tests are presented in figure 3.20. The compliance of the rod with the shallower of the two notches ranged between 0.03 and 0.045 mm/N and is

in excellent agreement with predicted values. The compliance of the rod with the deeper notch ranged between 0.06 and 0.08 mm/N and also correlates well with the predicted values.

Results from the fatigue tests show similar agreement, except for the specimens at the high load ratios, $R=0.45$. Figure 3.21 shows data for type II rods A, B and C, all at load ratio 0.10. Once again, agreement between measured and predicted values appears quite good, in spite of the depth diminishing slightly at the longitudinal extremes of damage length. Figure 3.22 shows data for rod H at load ratio 0.17, also with fairly good agreement. Figure 3.23 shows that the predicted compliance is overestimated over the whole range for type II rod I at $R=0.45$. The photograph of the sectioned rod I in figure 3.6 shows that the assumption of constant depth is slightly worse than for rod A, figure 3.5, for which measured and predicted compliance are in agreement. If the depth diminishes significantly along the length and the maximum depth is used as input in Eq. (3.18) the predicted compliance will be overestimated, which appears to be the case in figure 3.23.

Figure 3.24 shows data for type III rods E and G ($R=0.17$). The accuracy of the predicted values is similar to results for type II rods at $R=0.10$ and 0.17. Figure 3.25 shows data for rods D and F at load ratio 0.45. Similar to figure 3.23 for type II rod I at $R=0.45$, the predicted values are significantly higher than the measured values. The photographs in figure 3.11 and 3.12 show that the assumption of constant depth is slightly worse for rod F ($R=0.45$) than for rod G ($R=0.17$).

Inspection of figures 3.18 through 3.25 reveals, qualitatively at least, reasonable agreement between the measured values and the two parameter non-uniform cantilever beam approximation. To take a more critical look at the quality of the agreement linear regression lines were fit through each data set. The straight lines in figures 3.18 through

3.25 have a slope exactly equal to one. The slope from linear regression gives an indication of how good the agreement is; a slope less than one indicates the rod is stiffer than measured and a slope greater than one indicates the rod is less stiff than measured. These results are summarized in table 3.6.

Table 3.6. Comparison of measured and predicted compliance.

Rod Type	Test	Slope
Type I	Static	0.78-1.03
Type II	Static	1.15
Type III	Fatigue: R=0.10,0.17 R=0.45	0.78-0.95 0.60
	Static	0.93-1.00
Type III	Fatigue: R=0.10,0.17 R=0.45	0.78-1.08 0.55-0.76

In the static tests no trend towards overestimating or underestimating the compliance is apparent. As the approximation of constant depth over the damage length is a good one in this case, the model and damage state converge to give slopes near 1.00, some higher, some lower. The second assumption, that the damage part carries no load, appears to be justified in spite of fibre bridging.

For the fatigue tests the measured compliance has been consistently overestimated. In eight tests out of nine the slope of the measured versus predicted compliance line is less than one, indicating that the sample is stiffer than predicted. In the samples at load ratio 0.45 the correlation is particularly bad. The explanation lies in the constant depth assumption. As discussed above, the photographs in figures 3.6 and 3.12 show that the depth decreases at the longitudinal extremes, leaving more material to support the load than predicted, which has resulted in measured compliance values being lower than predicted

compliance values. Another factor may have been the contribution of fibre bridging allowing the damaged portion to support load, but this is ruled out in view of the static test results.

Apparently fatigue damage growth in these specimens cannot be modeled exactly by two damage parameters, nor can it be simulated exactly by a centre notch geometry under static loading. However, the agreement between theory and experiment is satisfactory under static conditions and under cyclic conditions at low load ratios. This agreement, coupled with the closed-form simplicity of the model, now leads to further insight into the nature of damage growth by way of energy release rate principles.

3.4 Energy Release Rate

Referring to figure 3.26 a damage growth hypothesis is advanced. In (a) the sample is damaged to an initial depth d by some as yet undetermined process. Further cycling breaks the fibres to depth d_1 . On breaking to depth d_1 the rod splits to length a_1 at constant depth d_1 . The longitudinal crack, once initiated, is assumed to grow in a self similar manner. Since the damaged part is unable to support load it can be neglected, (c). Further cycling causes further growth through the depth to d_2 . At depth d_2 the rod splits to length a_2 . Once again, the damaged part supports no load and may be removed, (f). The compliance in (f) is greater than the compliance in (c). Growth of the crack in the length direction is assumed to be met by a resistance G_c , the critical energy release rate.

According to the work of Griffith [11] a crack will grow when the energy required for crack extension is the same as the energy available from the system. Mathematically, the crack grows catastrophically in the length direction when

$$\frac{P^2 \partial C}{2b \partial a} \geq G_c \quad (3.20)$$

where b is the damage width. In figure 3.24 the crack grows in the length when the equality in Eq. (3.20) becomes true. However, it is important to emphasize that the longitudinal crack in the rods does not extend catastrophically. Thus if the critical energy release rate is a constant then the energy release rate must decrease, otherwise the crack would extend through to the ends of the rod. The partial derivative in Eq. (3.20) is easily evaluated from Eq. (3.18)

$$\frac{\partial C}{\partial a} = \frac{1}{E} \left[\frac{(l-a)^2}{I_2} - \frac{(l-a)^2}{I_1} \right] \quad (3.21)$$

The energy release rate G is then

$$G = \frac{P^2(l-a)^2}{2bE} \left[\frac{1}{I_2} - \frac{1}{I_1} \right] \quad (3.22)$$

For given material parameters and damage condition, that is given values of E , P , l , a and d , the energy release rate G takes on a particular value. If this value meets or exceeds the lengthwise crack resistance G_c , the damage length will extend. By inspection of Eq. (3.22) it is clear that the energy release rate *decreases* as crack length increases and increases as crack depth increases (from Appendix B : I_1 =constant, I_2 decreases as d increases). Figure 3.27 shows this graphically. Plotted is the energy release rate as a function of crack length for four crack depths. At a given depth the energy release rate decreases. At a given length the energy release rate increases with increasing depth. The horizontal line represents the lengthwise crack resistance, for the moment assumed constant. At point A the depth is 0.5 mm and G is greater than G_c . From Eq. (3.22) the crack must grow. It does so not in the

depth direction, but in the length direction at constant depth to point B. At point B, G and G_c are equal and growth in the length direction stops. Further cycling causes damage to grow in the depth direction to point C. At this new depth G is once again greater than G_c . Once again, the damage grows in the length direction at constant depth to point D. At this point G and G_c are equal and growth in the length direction stops. This process continues out to point H and beyond. As the length grows closer to the outer load points, increases in depth cause smaller increases in length. This is consistent with the observation that the growth rate in the length direction decreased while the growth rate in the depth direction remained constant as cycling progressed in each of the cyclic loading tests.

3.4.1 Relation Between Damage Parameters

During cyclic loading damage growth occurs on a much finer scale than depicted in figure 3.27. However, if Eq. (3.22) is true there should be a relation between length and depth regardless of whether loading conditions are static or cyclic. By rearranging Eq. (3.22) and combining with Eq. (3.1) the length can be written as a function of depth as follows

$$a = l - \frac{2}{P} \left(\frac{G_c E I_1 I_2 (2rd - d^2)^{1/2}}{I_1 - I_2} \right)^{1/2} \quad (3.23)$$

Since I_2 is a function of damage depth, Eq. (3.23) relates damage length and depth.

By substituting the constant values of $P_{\max}/2$, E , $L/2$ and the varying values of a and d into Eq. (3.22) values of G_c at several points during the damage evolution were determined for type I, II and III rods. It is possible to substitute values of the crack length into Eq. (3.22) to obtain G_c and not just G because G is decreasing as the crack length increases. Thus when a particular crack length and load $P < P_{\max}$ combination reaches G_c , the crack

grows, but not catastrophically. When the load reaches P_{\max} the crack stops lengthening and G and G_c strike a balance between growth and arrest; this is the combination of material and geometric parameters that define G_c and these are the parameters that were recorded during the static tests.

The two type I rods were each tested at a different span and maximum load. For both rods it was found that G_c increased considerably as crack area increased. The minimum value measured, at a shallow depth and for a short crack length, was 183 J/m^2 . For both rods the value increased to 638 J/m^2 for crack areas of approximately 1800 mm^2 . Once the values of G_c are known the relation between damage length and depth becomes apparent. Figure 3.28 shows the depth as a function of length for the longer of the two specimens. The solid lines are from Eq. (3.23). At the start of the test depth and length were small and the first point falls on the line representing $G_c=483 \text{ J/m}^2$. Had G_c remained constant the remainder of the points would have fallen on this line. However, as fibre bridging developed, G_c increased, first to 567 J/m^2 where the second point lies, then levelled off at 638 J/m^2 where the final two points lie. Thus there appears to be a relation between the two damage parameters, but it becomes evident only by recognizing that G_c increases with increasing crack length.

The results for the shorter of the two type I rods are shown in figure 3.29. The line representing $G_c=638 \text{ J/m}^2$ in figure 3.29 is different than the line representing $G_c=638 \text{ J/m}^2$ in the previous figure because the relation between damage parameters changes due to the change in span and maximum load. For this test the lowest recorded G_c value was 183 J/m^2 , the line on which the first point lies. The points towards the middle are fit with the line representing $G_c=432 \text{ J/m}^2$ and the final points land on the line representing $G_c=638 \text{ J/m}^2$.

The type II and the type III rods were tested slightly differently. Rather than measuring a series of a,d pairs at the same maximum load, the depth was kept constant while maximum load and length increased. The value of G_c for the type II rod is shown as a function of crack area in figure 3.30. The minimum value of G_c was 202 J/m^2 , slightly higher than for the type I rod. As the crack area increased beyond approximately 200 mm^2 the critical energy release rate increased rapidly. At a value of approximately 500 J/m^2 it increased more slowly, reaching 920 J/m^2 at a crack area of 1400 mm^2 . This large increase may be attributed to the extensive network of fibre bridging.

Since the G_c values are known for the static case the relation between damage dimensions, a function of G_c , can now be investigated for the type II rods subjected to cyclic loading, figure 3.31. The three solid lines represent G_c at 202, 561 and 920 J/m^2 , the maximum, minimum and average values of G_c from the static test. Data for rods A (R=0.10), H (R=0.17) and I (R=0.45) fall mostly between the three lines. At the beginning of the test where the crack length was between 0 and 80 mm the points are nearer to the lines representing the low G_c values. This correlates well with the static test where G_c was small for small crack areas. As the length and depth progressed the crack area became larger and G_c increased. For instance at a damage length of 140 mm and a damage depth of 2 mm in figure 3.31 the crack area is 1400 mm^2 . At this point the data for rod A fall on the line representing $G_c=920 \text{ J/m}^2$ which correlates well with the static test where G_c is also near 920 J/m^2 when the crack area is 1400 mm^2 , figure 3.30. As discussed previously, the predicted compliance for Rod I, tested at the high load ratio, was in poor agreement with the measured compliance because the depth diminished towards the ends of the longitudinal crack. This implies the crack area was smaller than what would be predicted from the product of crack length and maximum crack depth. Thus the true crack area for the points corresponding to rod I in figure 3.31 is less than that implied by the plotted length and

depth values. From figure 3.30 a smaller crack area implies a smaller G_c value which may explain why these points lie closer to the line representing $G_c=561 \text{ J/m}^2$. As with the type I rods, it appears that the damage length and depth are related by Eq. (3.23), but only by recognizing that G_c increases as crack area increases. In particular G_c has increased in the fatigue tests similar to the way it increased during the static test, indicating the presence of fibre bridging during the fatigue tests.

The two type III rods were tested in similar fashion, at two different crack depths. The increase in critical energy release rate as a function of crack area for both rods is shown in figure 3.32. Since the crack depths were different the same crack area was achieved at different crack lengths, yet the data from both tests fall on the same line. The minimum G_c value for the type III rods was 287 J/m^2 . Once again G_c increased with crack area, levelling off at 1400 J/m^2 for the larger crack areas. This unusually large G_c value may be attributed to the large amount of fibre bridging that was observed during these tests; recall that fibre bundles as large as 2 mm in diameter were seen between the upper and lower crack planes.

The relation between damage parameters for rods E and G ($R=0.17$) is shown in figure 3.33. The solid lines indicate constant G_c at 287, 854 and 1416 J/m^2 . Even at large crack areas (high values of a and d) the data do not reach the high values of G_c . Figure 3.34 shows the relation between damage parameters for rods D and F ($R=0.45$). As in the previous figure the data lie closer to the lines representing the lower G_c values. In the previous section the lack of agreement between measured and predicted compliance for type III rods was related to decreasing damage depth as a function of length. Thus the crack area is less than that implied by the product of length and depth in figures 3.33 and 3.34. At constant damage depth the same crack area in figure 3.32 would be represented by

a shorter crack length. The points would then shift left (shorter crack length) towards the higher G_c value in figures 3.33 and 3.34. A second possible explanation is that rather than fibres bridging the crack plane, the crack plane shifted to a lower depth at points along the length where large bundles of fibres would have otherwise bridged the crack plane. This might reduce the measured compliance from its predicted value and reduce G_c due to the absence of fibre bridging.

3.5 Damage Development

From the preceding discussion of compliance and energy release rate the general conclusion is that the damage zone resulting from cyclic loading can be described, to a first approximation, by a damage length and a damage depth and that these two damage parameters are related to each other by modulus, span, maximum load and critical energy release rate. The relation between length and depth allows one to prescribe one damage dimension and determine the other. Thus damage development may be seen as damage growth in the depth direction as a result of some fatigue process and damage growth in the length direction as a result of damage in the depth direction.

It has already be shown in figures 3.9 and 3.15 that the growth rate of the damage depth is nearly constant with respect to applied cycles. The growth rate of damage depth for each of the samples tested under cyclic loading is shown in tables 3.3 and 3.4. The limited amount of data available will not lead to a high level of confidence in establishing a growth law due to the limited range of loading conditions tested. However some trends are apparent between the growth rate and mean load, maximum load and load range.

The present data suggests that in addition to stress range, maximum or mean stress may influence the growth rate. As mentioned previously all cyclic loading tests were

carried out at maximum stresses approaching the failure stress, at various stress ratios.

Therefore only the maximum stress and stress range will be considered. Thus as a starting point

$$\frac{dd}{dN} = C \sigma_{\max}^m \Delta\sigma^n \quad (3.24)$$

Since the rods are transversely isotropic the usual solution for bending stresses for isotropic materials applies

$$\sigma = \frac{My}{I_2} \quad (3.25)$$

The tensile stress at the central load point is therefore strictly a function of load, span and depth at that point. The damage depth some distance away from the central load point, in most cases slightly less than at the central load point, does not affect the maximum stress at the central load point. For the circular cross section it turns out that the y/I_2 term in Eq. (3.25) is nearly constant over the range of damage depths encountered. Thus it is more convenient to substitute ΔP for $\Delta\sigma$ in Eq. (3.24) to arrive at

$$\frac{dd}{dN} = C P_{\max}^m \Delta P^n \quad (3.26)$$

The growth rate of damage depth in type II rods A, H and I is shown in figure 3.9. The growth rates and loading conditions of the five type II rods tested are tabulated in table 3.3. Unfortunately the data do not permit the determination of the exponent m at constant load range or the exponent n at constant maximum load. The best fit to the data based on ΔP ($m=0$) is $dd/dN = 117.36\Delta P^{-1.6576}$. As mentioned previously a negative value for n is contrary

to expectations. Based on P_{\max} ($n=0$) $dd/dN = 3.05 \times 10^{-29} P_{\max}^{8.143}$. The latter empirical relation fits the data, but is insufficient to determine whether the C and m values are material constants or to determine the influence of load range.

For the type III rods the growth rate of damage depth is shown for rods F and G in figure 3.15. The growth rates and load data for these and two other type III rods are shown in table 3.4. Three samples were tested at the same maximum load, two at $R=0.17$ and one at $R=0.45$. One rod was tested at a smaller maximum load and at $R=0.45$. With $m=0$ in Eq. (3.26) the relation $dd/dN = 2.36 \times 10^{-9} \Delta P^{1.705}$ appears to fit all the data. This is consistent with experience in metals as the growth rate increased with increasing load (or stress) range. Here also there may be some dependency on maximum stress. The above correlation at constant maximum load can be made for rods E, F and G; $dd/dN = 2.999 \times 10^{-9} \Delta P^{1.671}$. Using these new values of C and n, a value for m in Eq. (3.40) was determined from rods D and F which were tested at nearly the same load range but at different maximum loads. The best fit was obtained with $dd/dN = 3.441 \times 10^{-15} P_{\max}^{1.867} \Delta P^{1.671}$. This particular set of constants, C, n and m, fit the present data, but more tests would be needed to verify whether or not they are material constants.

Based on these limited results the type II rods seem to have a large dependency on maximum load and the type III rods on load range and maximum load.

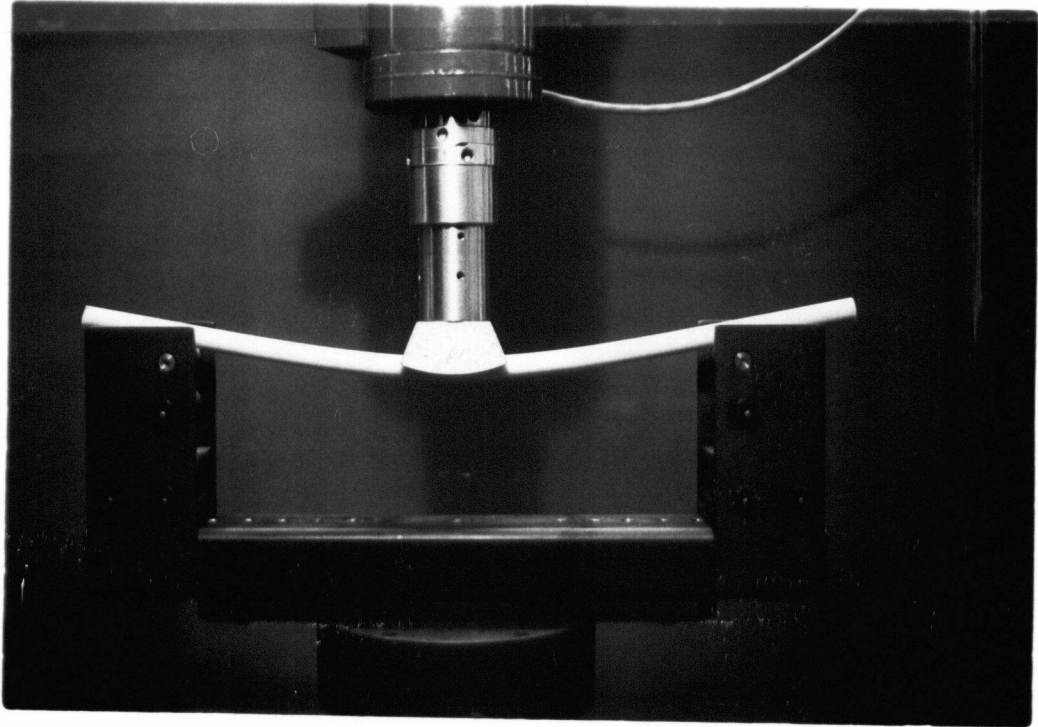
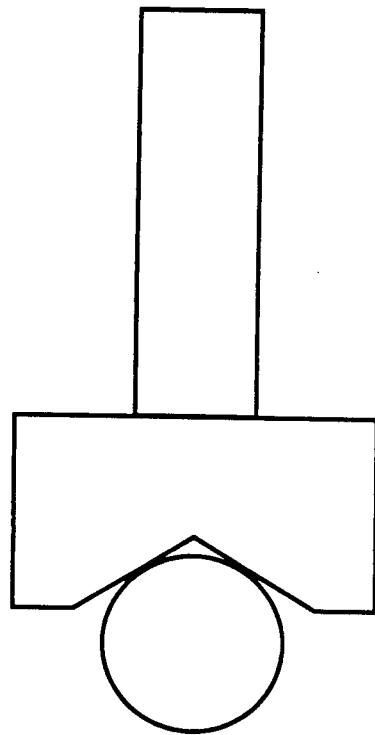
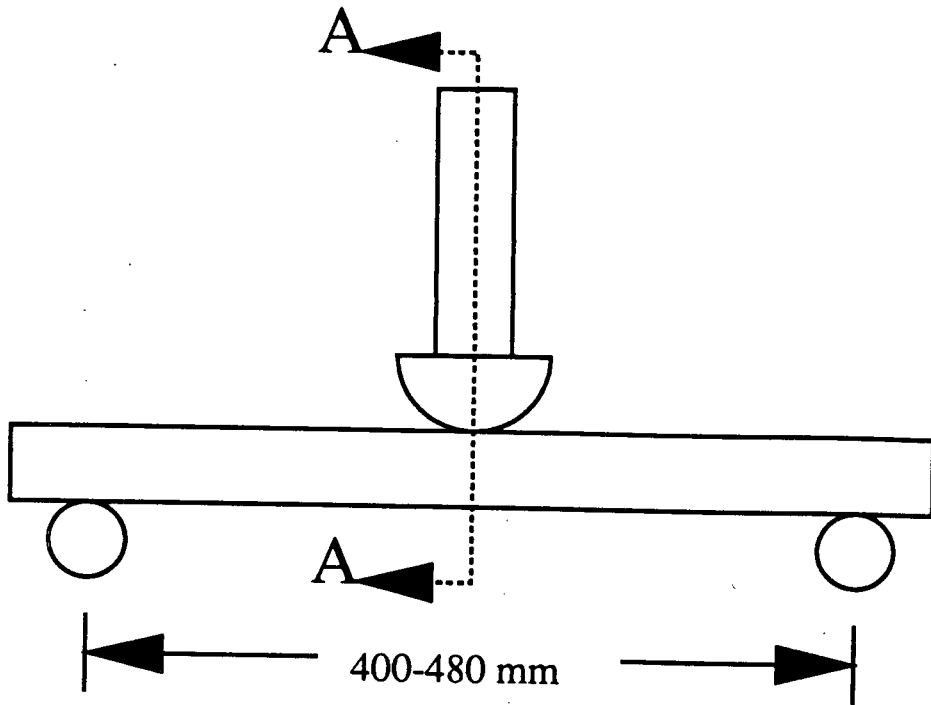


Figure 3.1 (a) Three point bending apparatus.



Section AA

Figure 3.1 (b)

Details of three point bending apparatus.

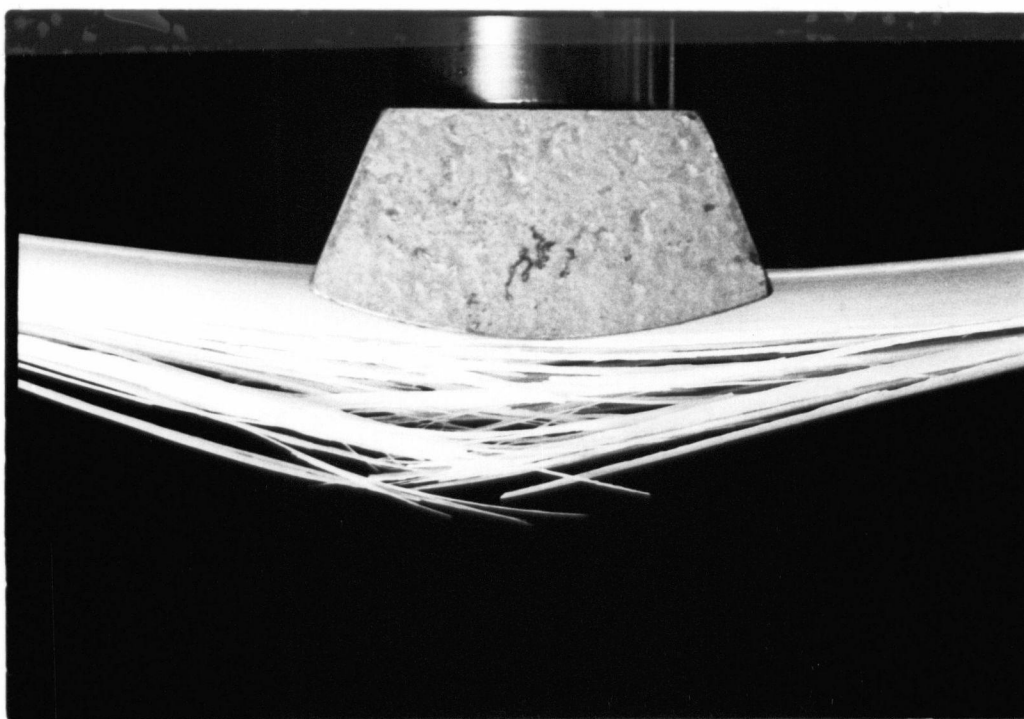


Figure 3.2 (a) Broom-like fracture zone in type II rod. Damage grows in both length and depth.

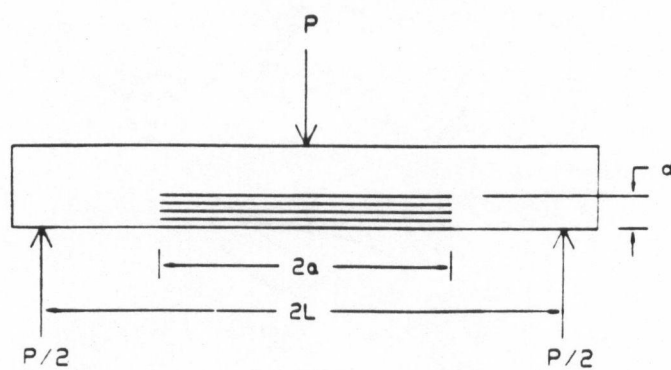


Figure 3.2 (b) Schematic representation of damaged rod.

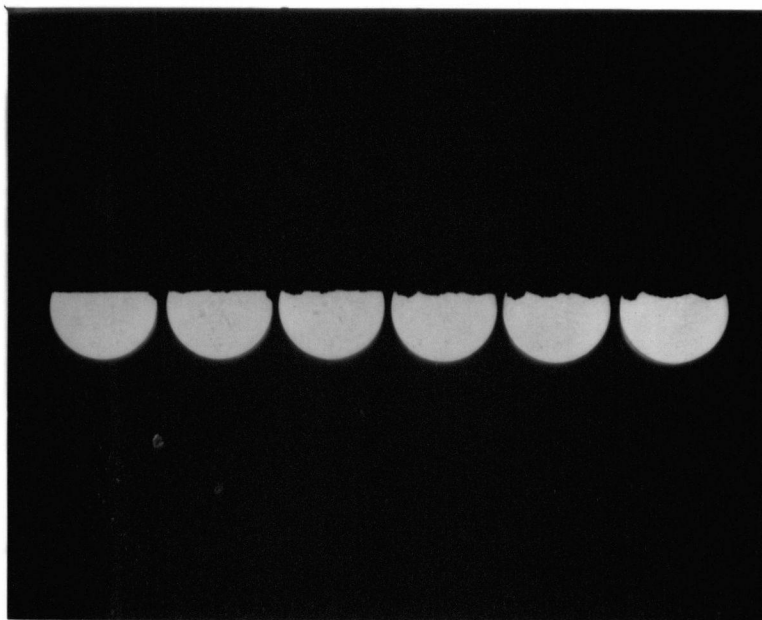


Figure 3.3 Damage profile of type I rod. Cross sections are at 40 mm intervals from the central load point (left) to the maximum extent of longitudinal damage (right).

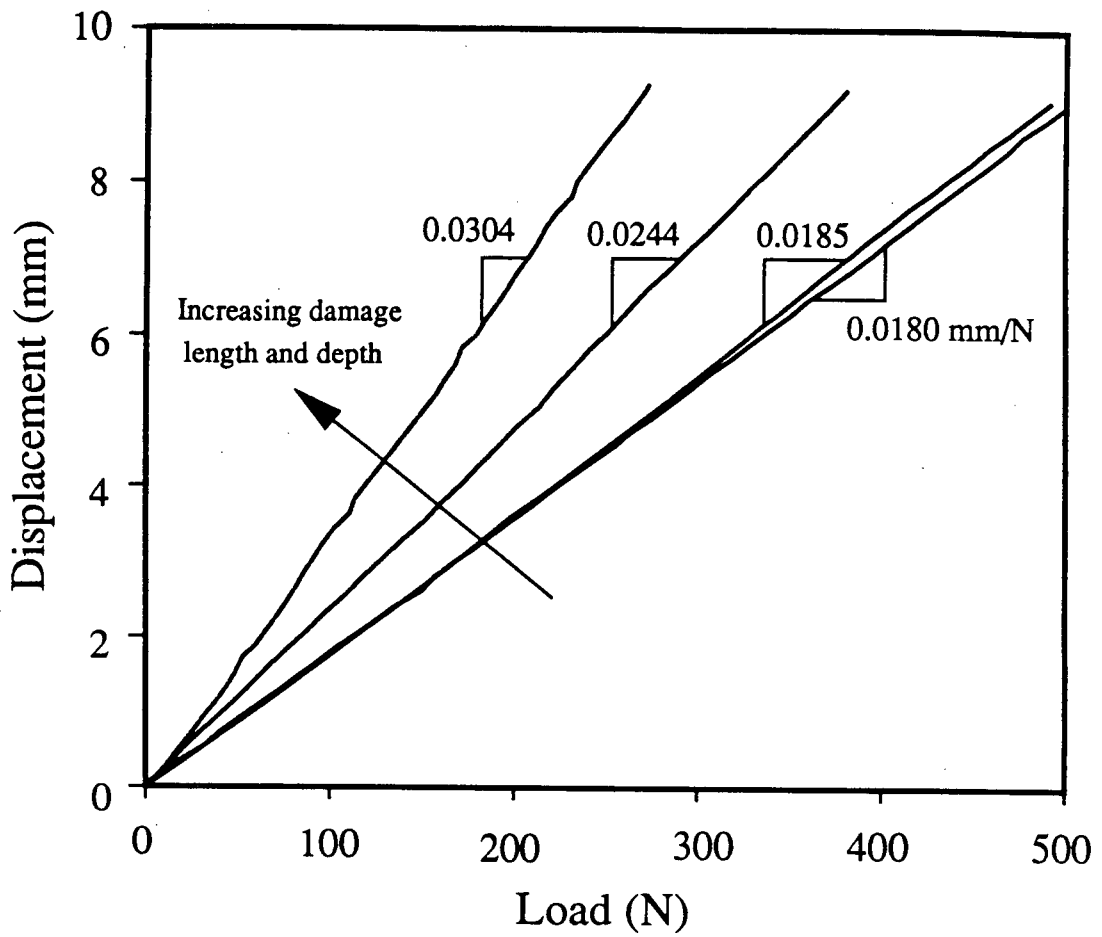


Figure 3.4

Compliance increase in type I rod with increasing damage zone size.

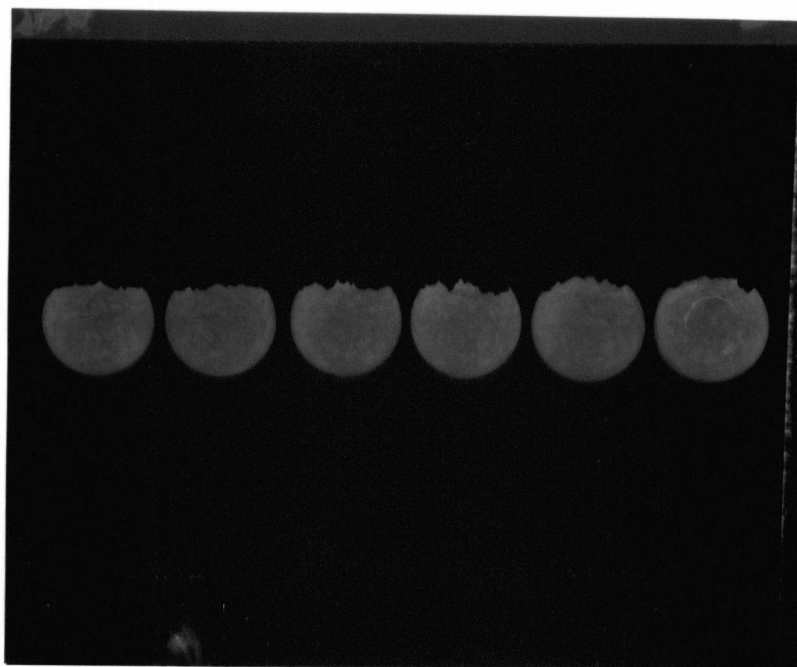


Figure 3.5 Damage profile of type II rod A ($R=0.10$). Cross sections are at 30 mm intervals from the central load point (left) to the maximum extent of longitudinal damage (right).



Figure 3.6 Damage profile of type II rod I ($R=0.45$). Cross sections are at 30 mm intervals from the central load point (left) to the maximum extent of longitudinal damage (right).

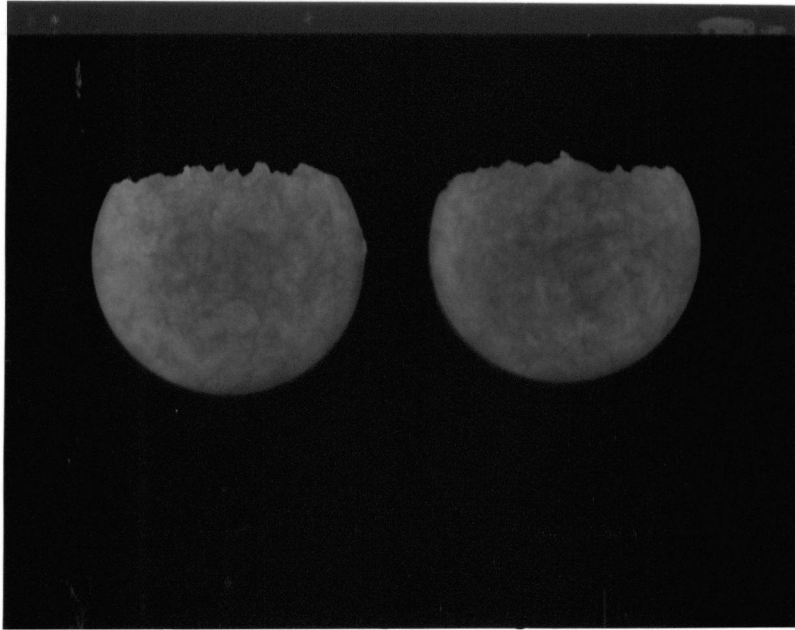


Figure 3.7 Damage profiles at the central load point of type II rods A, $R=0.10$ (left), and rod I, $R=0.45$ (right).

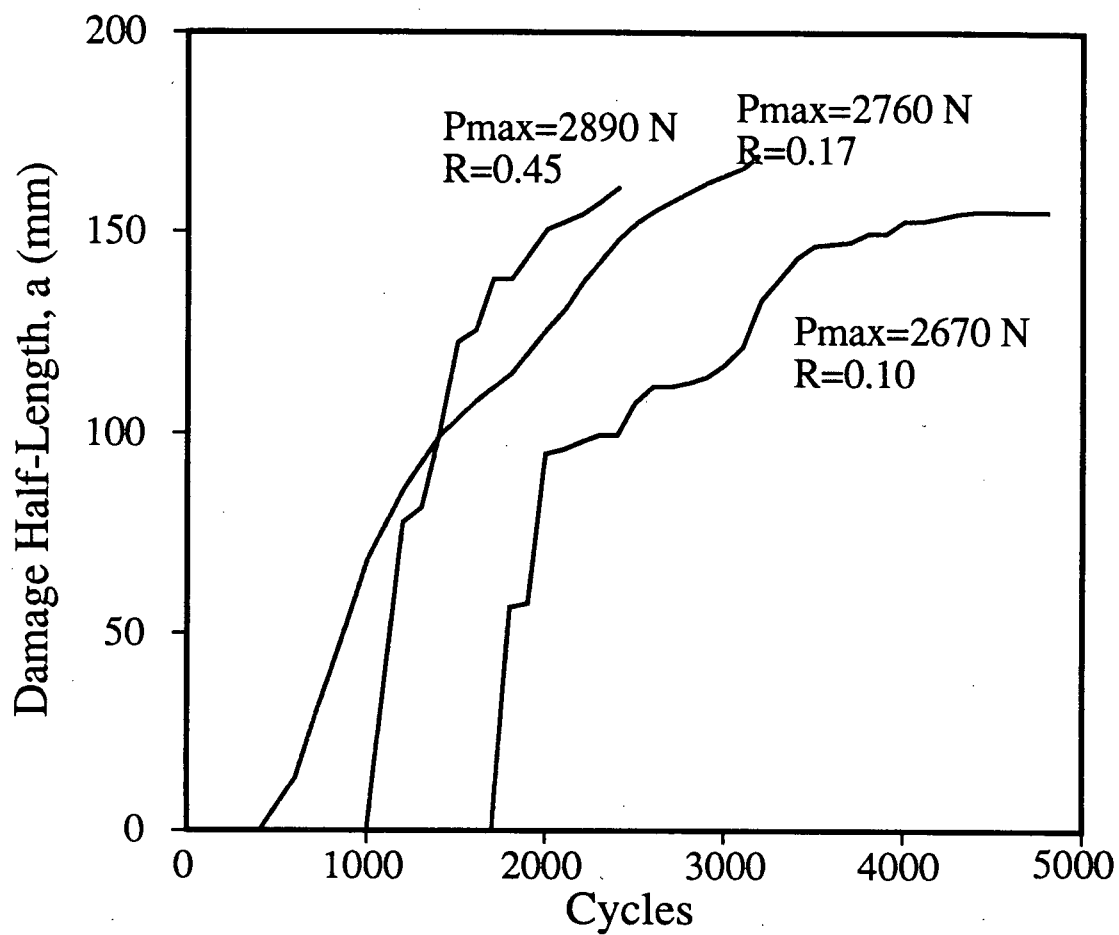


Figure 3.8 Increase in damage length as a function of cycles for type II rods A, H and I.

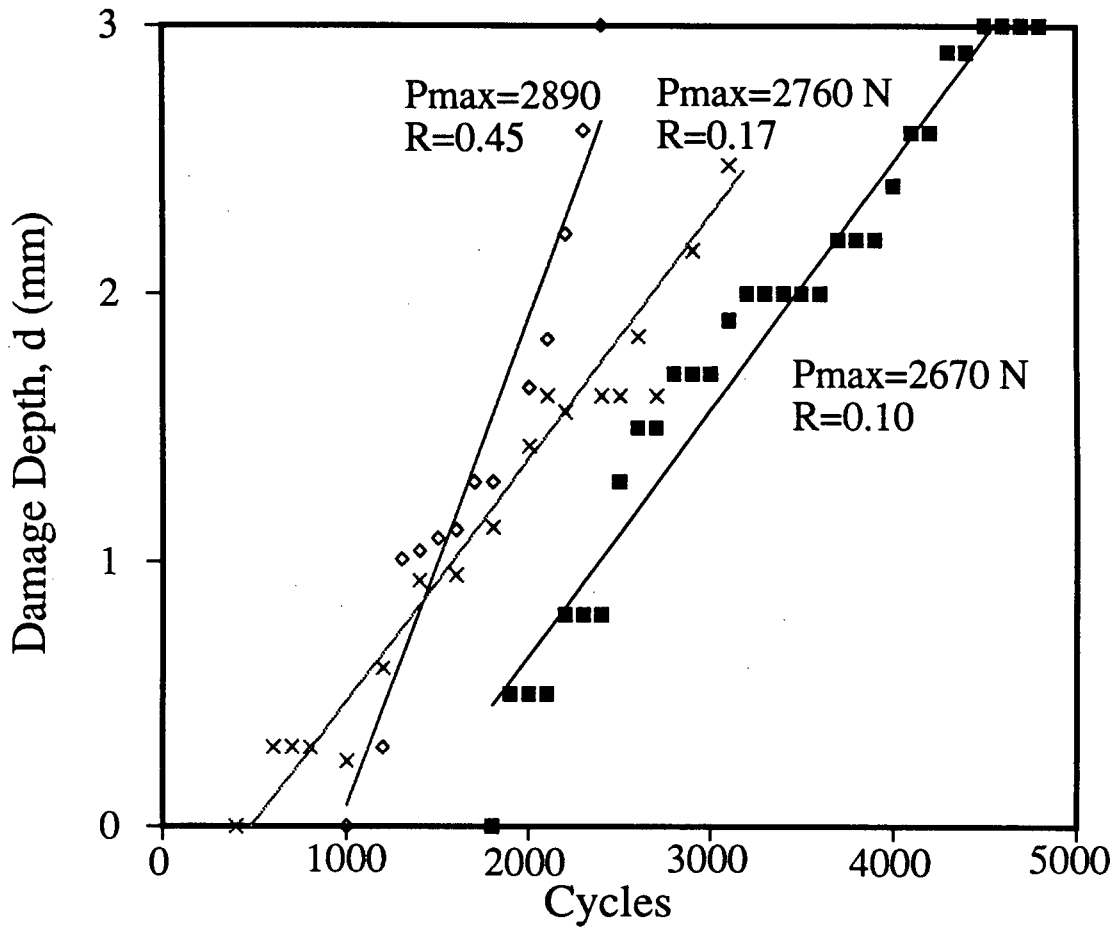


Figure 3.9 Increase in damage depth as a function of cycles for type II rods A, H and I. Linear regression lines represent constant growth rate.

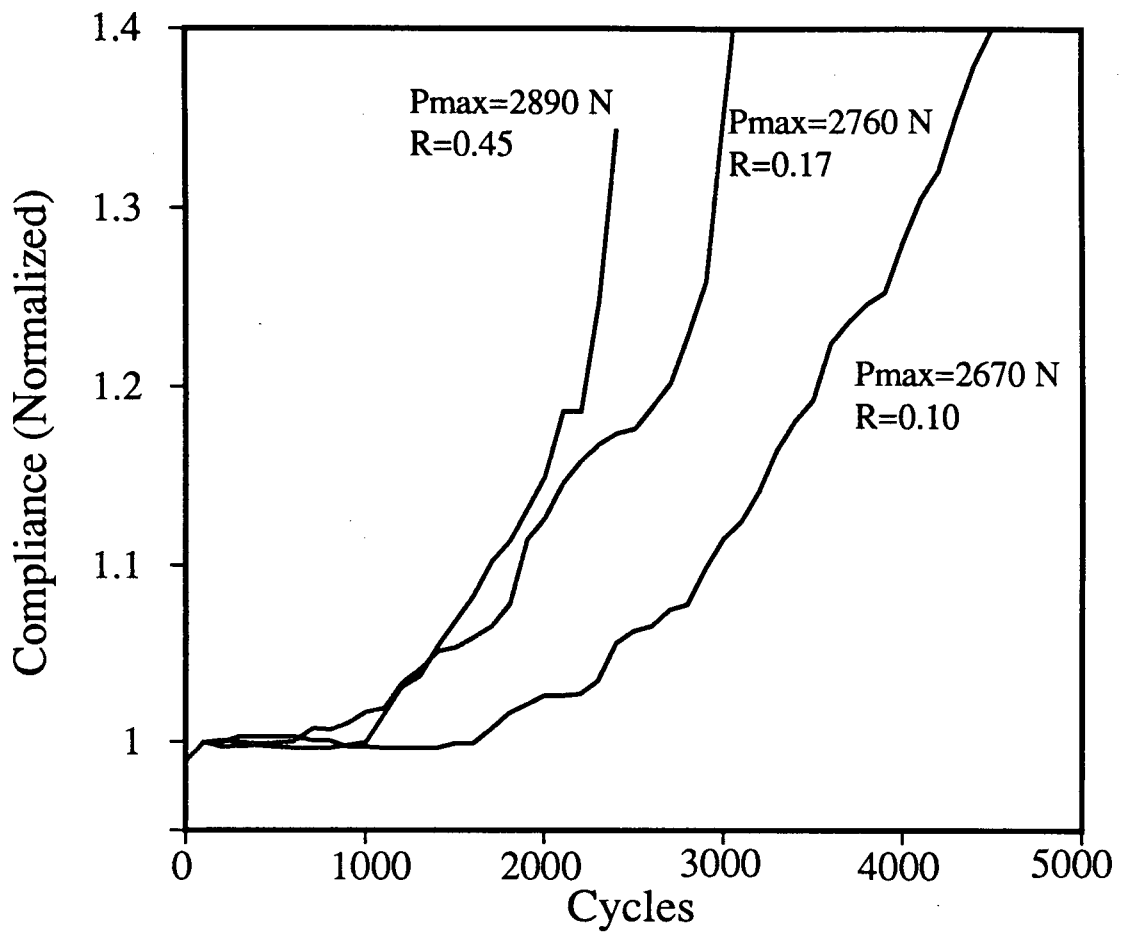


Figure 3.10 Increase in compliance as a function of cycles for type II rods A, H and I. Compliance values are normalized with respect to initial compliance.

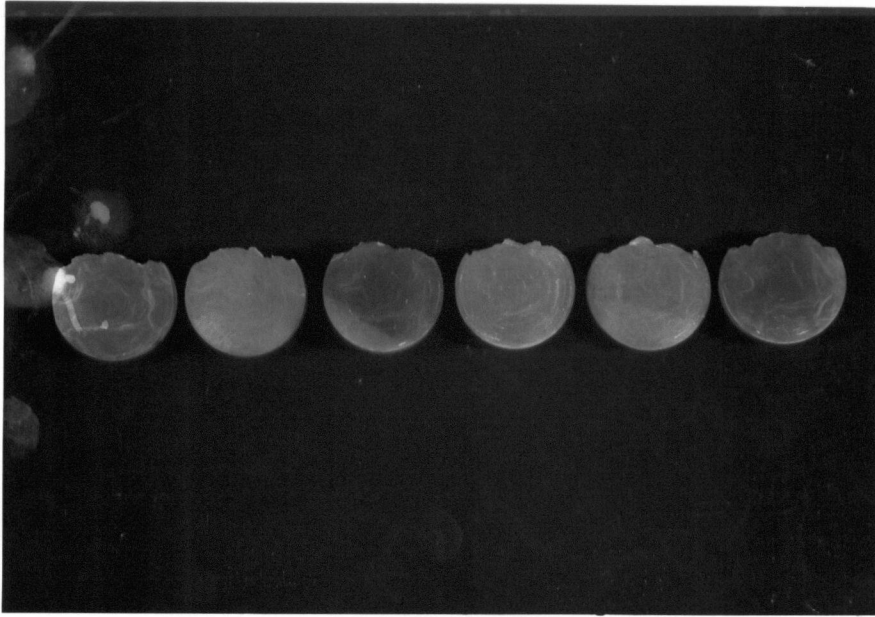


Figure 3.11 Damage profile of type III rod G ($R=0.17$). Cross sections are at 30 mm intervals from the central load point (left) to the maximum extent of longitudinal damage (right).

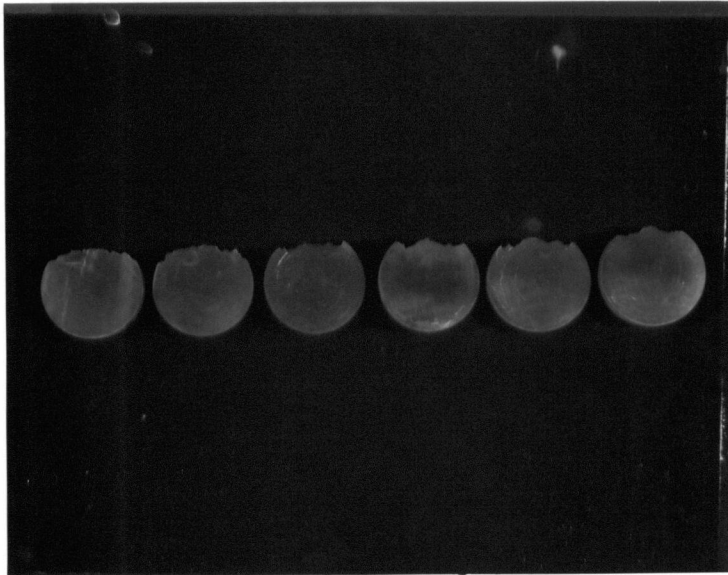


Figure 3.12 Damage profile of type III rod F ($R=0.45$). Cross sections are at 30 mm intervals from the central load point (left) to the maximum extent of longitudinal damage (right).

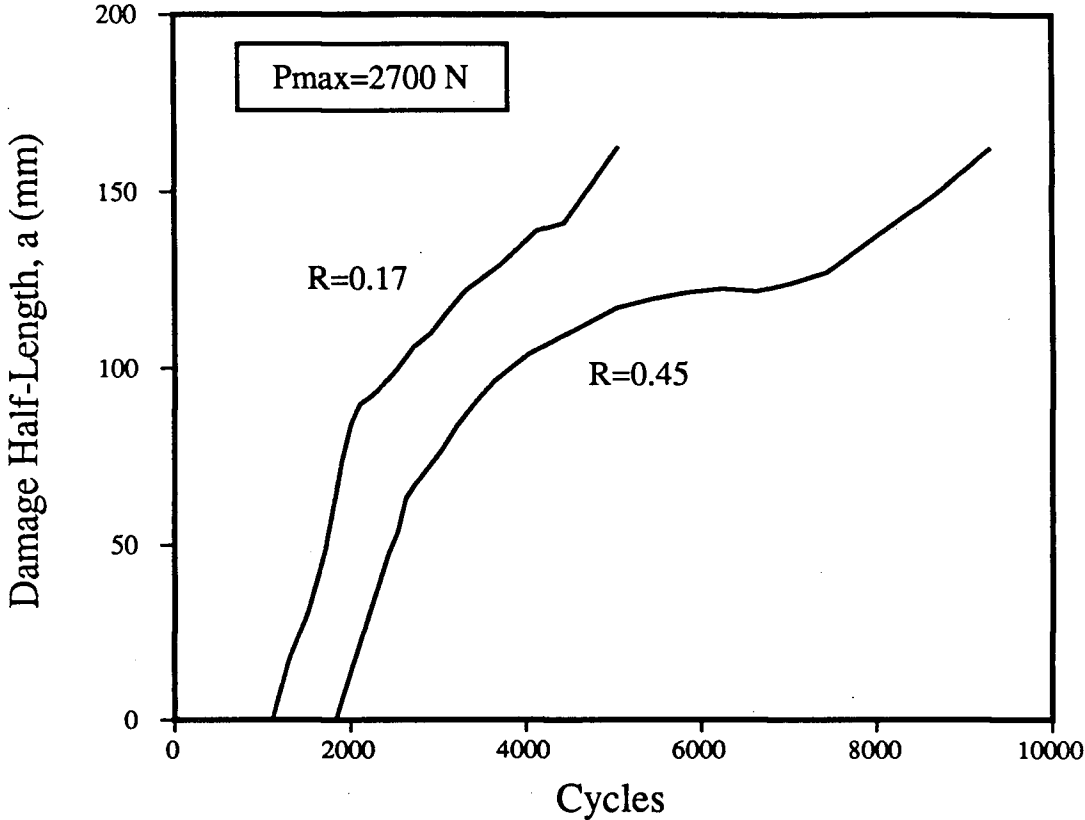


Figure 3.13 Increase in damage length for type III rods F and G as a function of cycles.

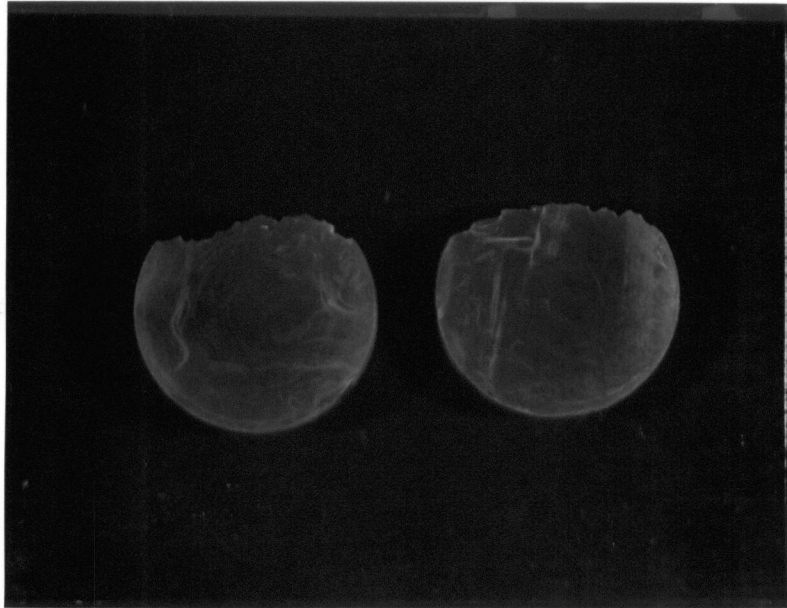


Figure 3.14 Damage profiles at the central load point of type III rods G, $R=0.17$ (left) and rod F, $R=0.45$ (right).

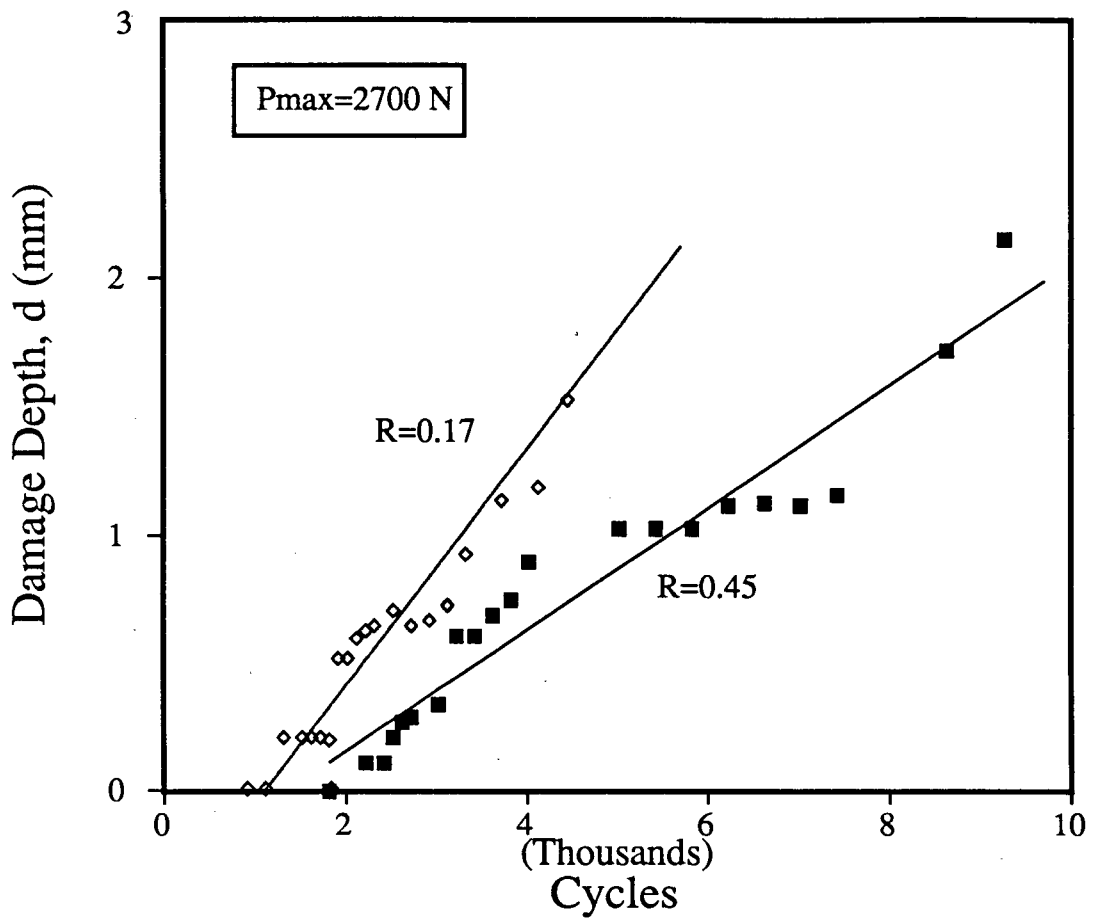


Figure 3.15 Increase in damage depth as a function of cycles for type III rods F and G. Linear regression lines represent constant growth rate.

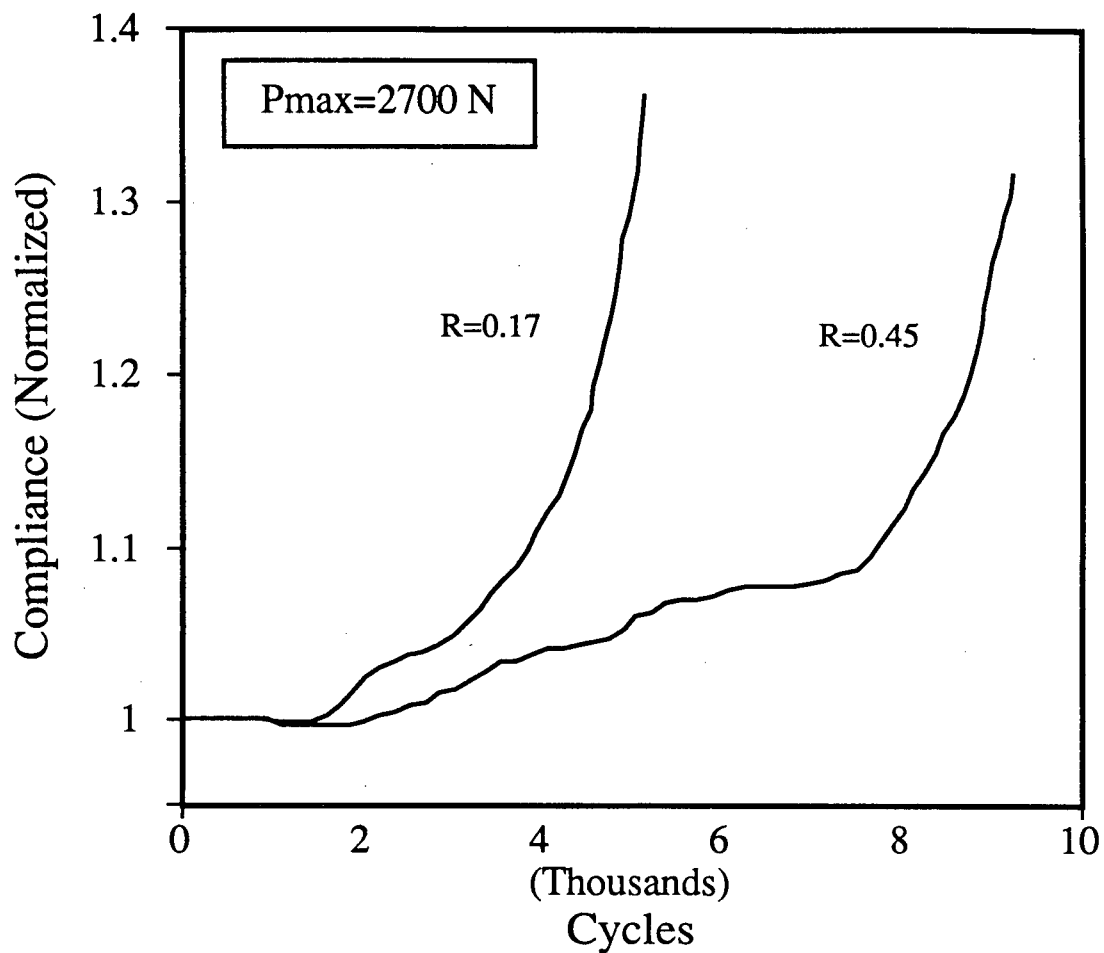


Figure 3.16 Increase in compliance as a function of cycles for type III rods F and G. Compliance values are normalized with respect to initial compliance.

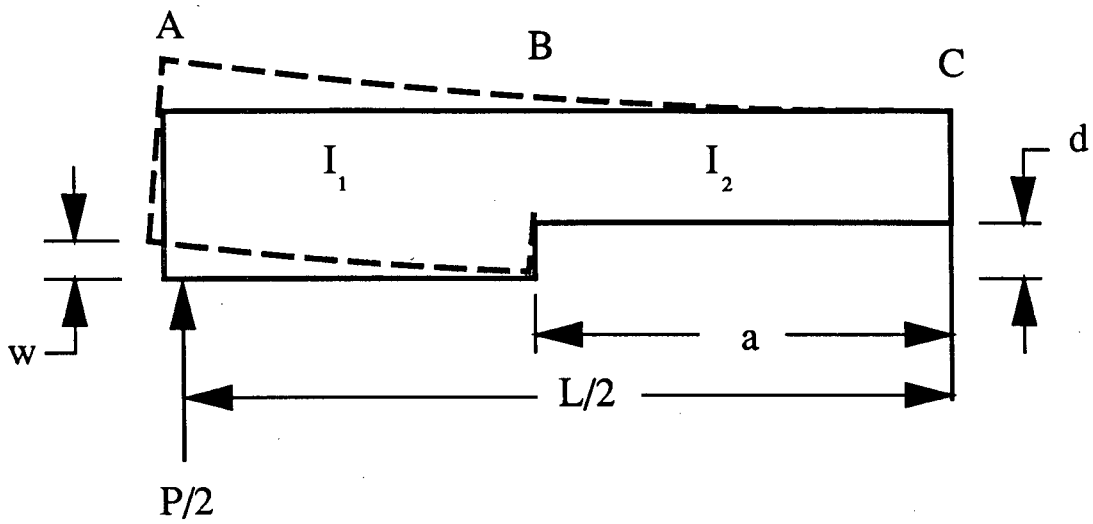


Figure 3.17 Damaged rod modelled as a non-uniform cantilever beam.

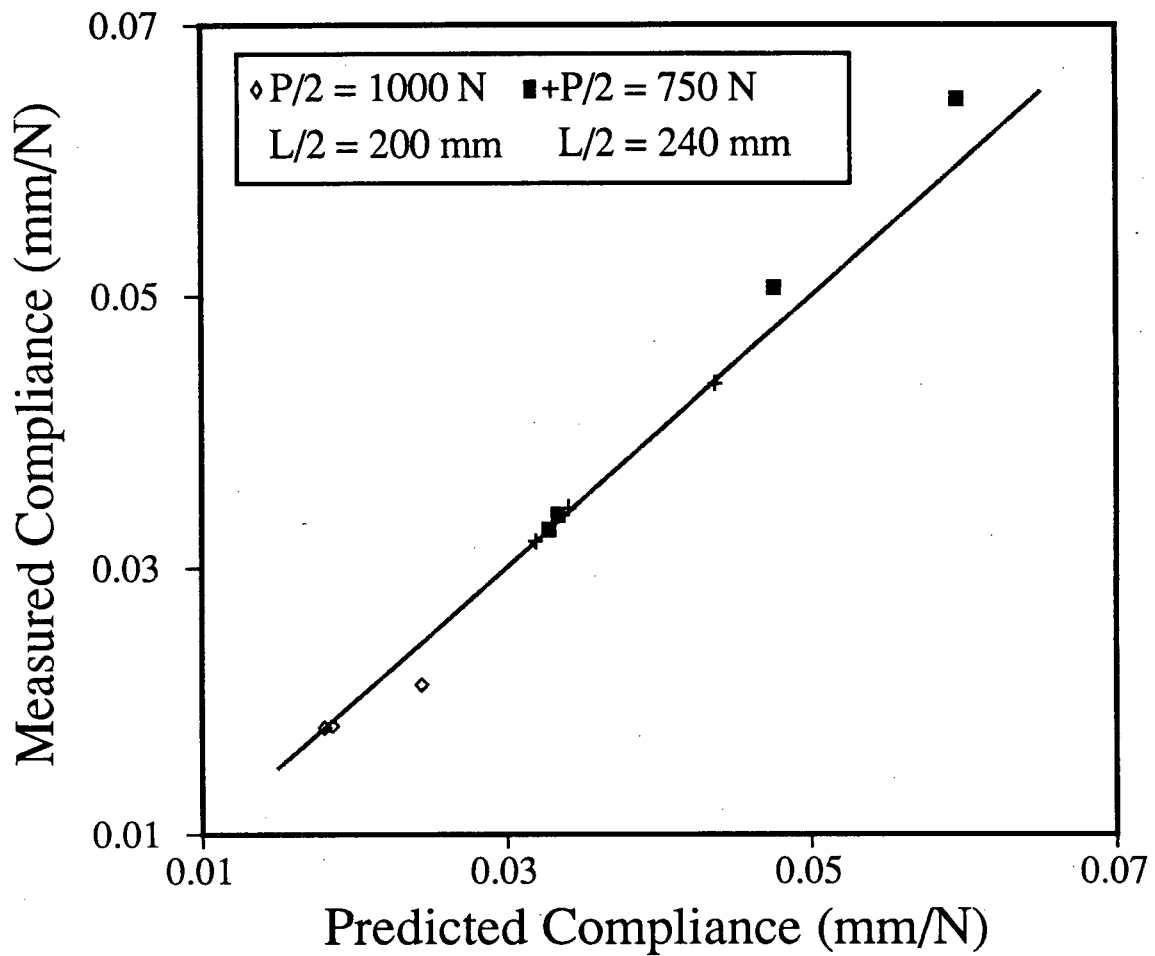


Figure 3.18 Measured vs. predicted compliance for type I rods, static loading. The straight line represents ideal agreement between prediction and experiment.

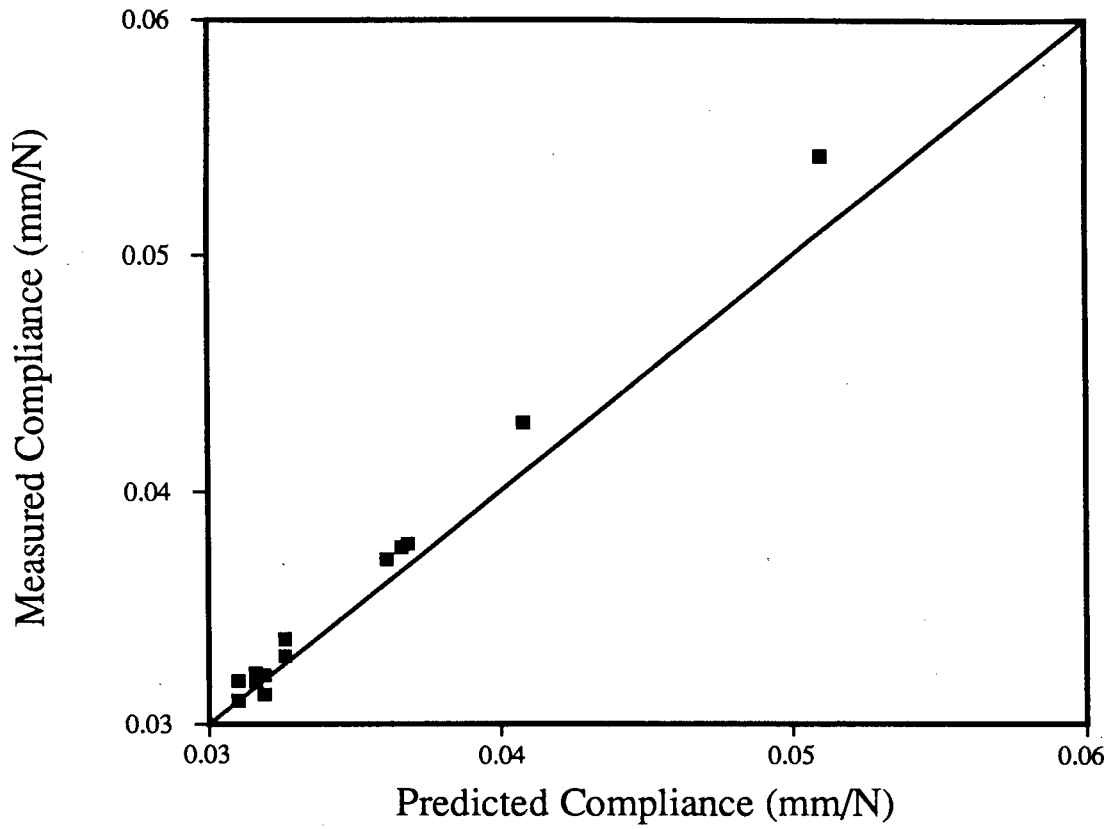


Figure 3.19 Measured vs. predicted compliance for type II rod, static loading. The straight line represents ideal agreement between prediction and experiment.

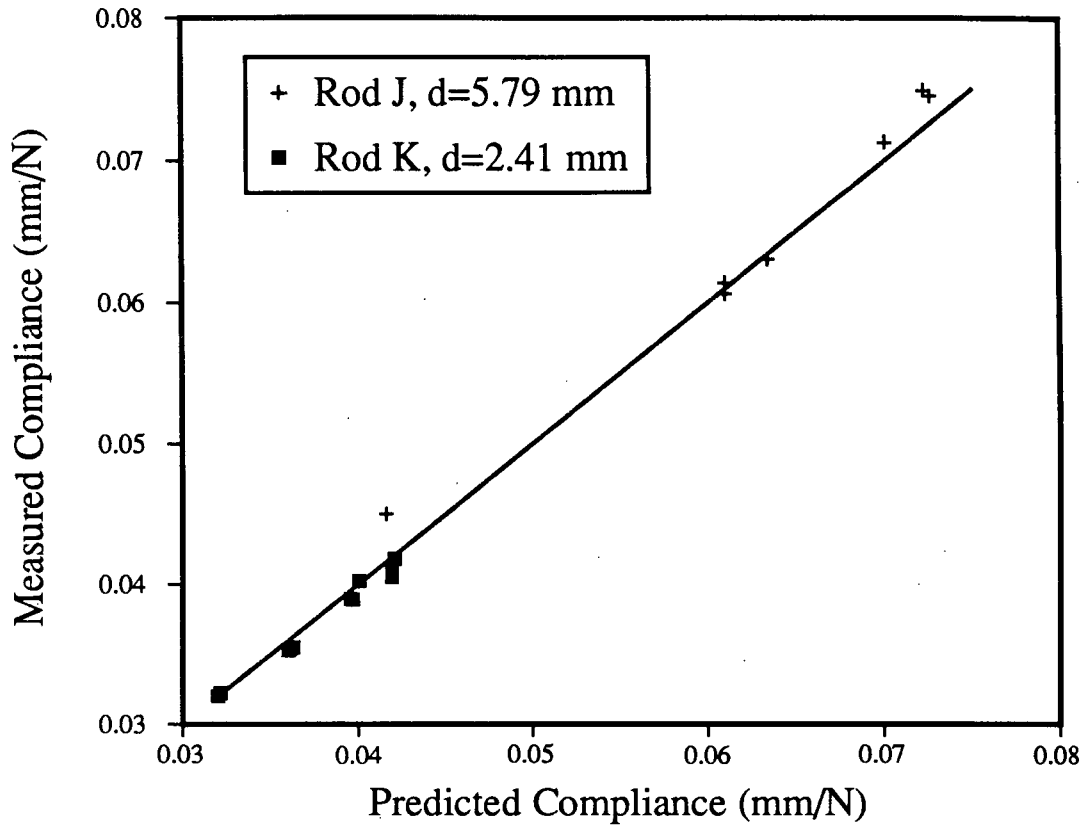


Figure 3.20 Measured vs. predicted compliance for type III rods, static loading. The straight line represents ideal agreement between prediction and experiment.

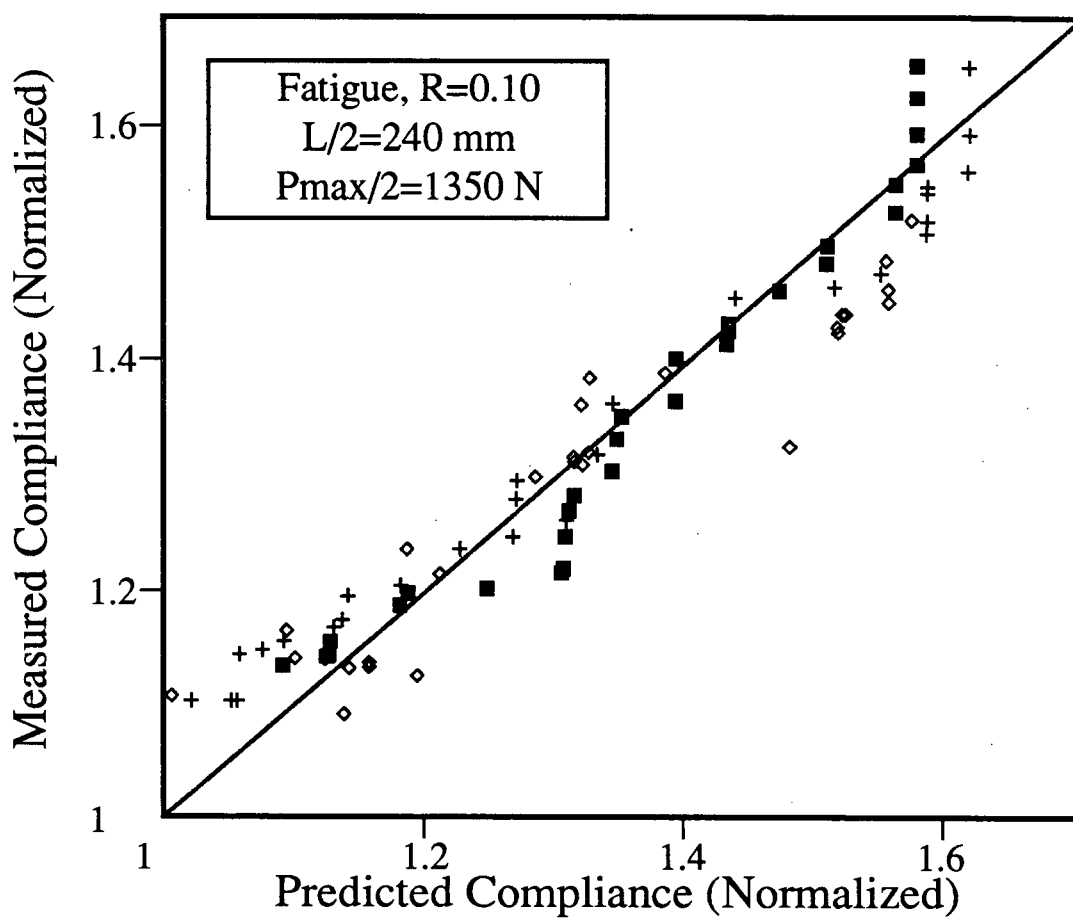


Figure 3.21 Measured vs. predicted compliance for type II rods, $R=0.10$. The straight line represents ideal agreement between prediction and experiment.

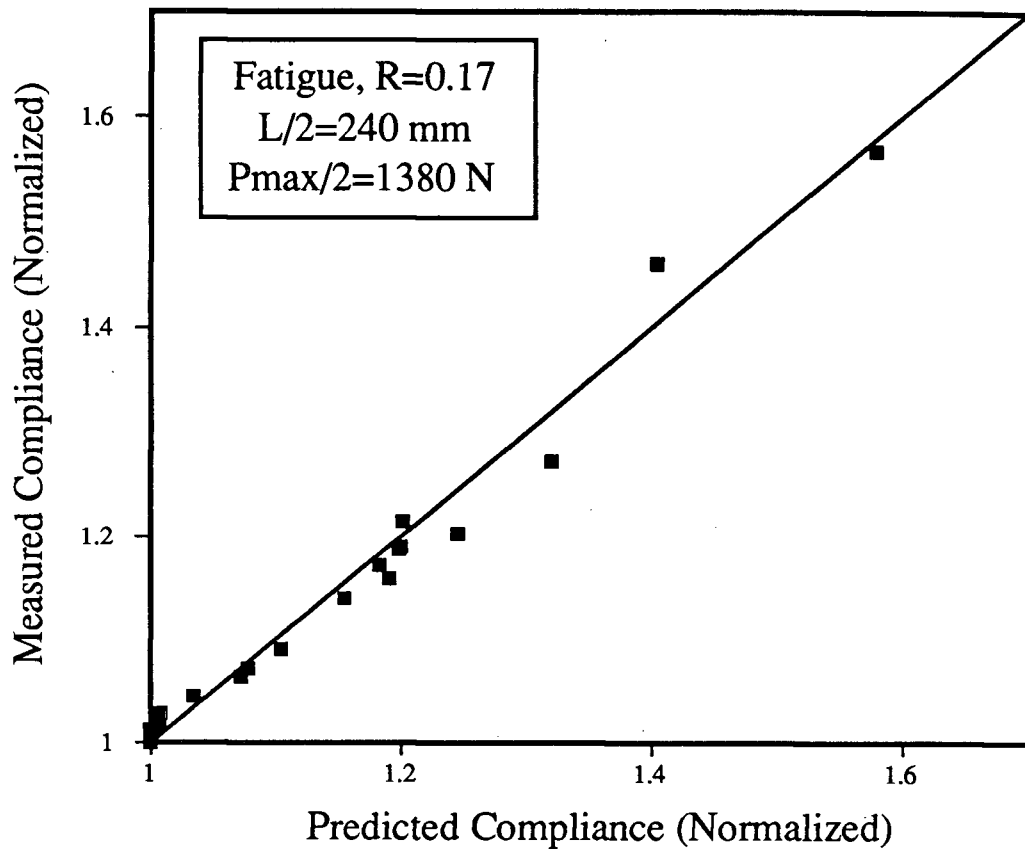


Figure 3.22 Measured vs. predicted compliance for type II rods, $R=0.17$. The straight line represents ideal agreement between prediction and experiment.

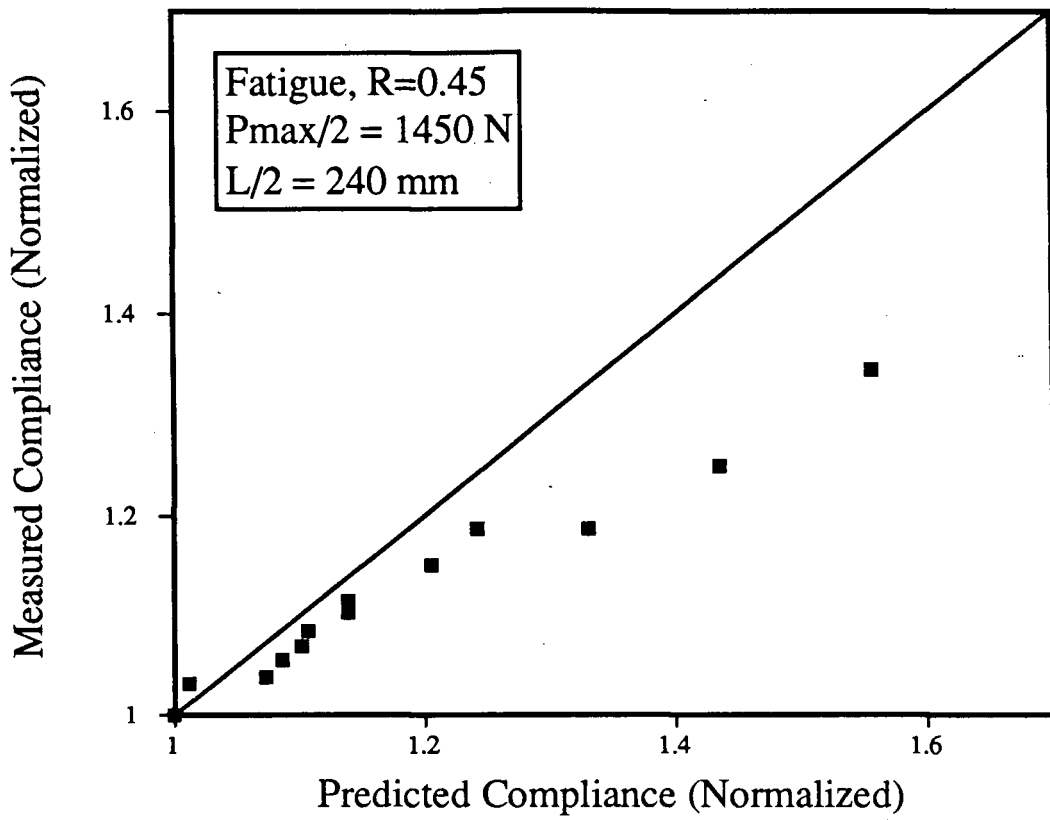


Figure 3.23 Measured vs. predicted compliance for type II rods, $R=0.45$. The straight line represents ideal agreement between prediction and experiment.

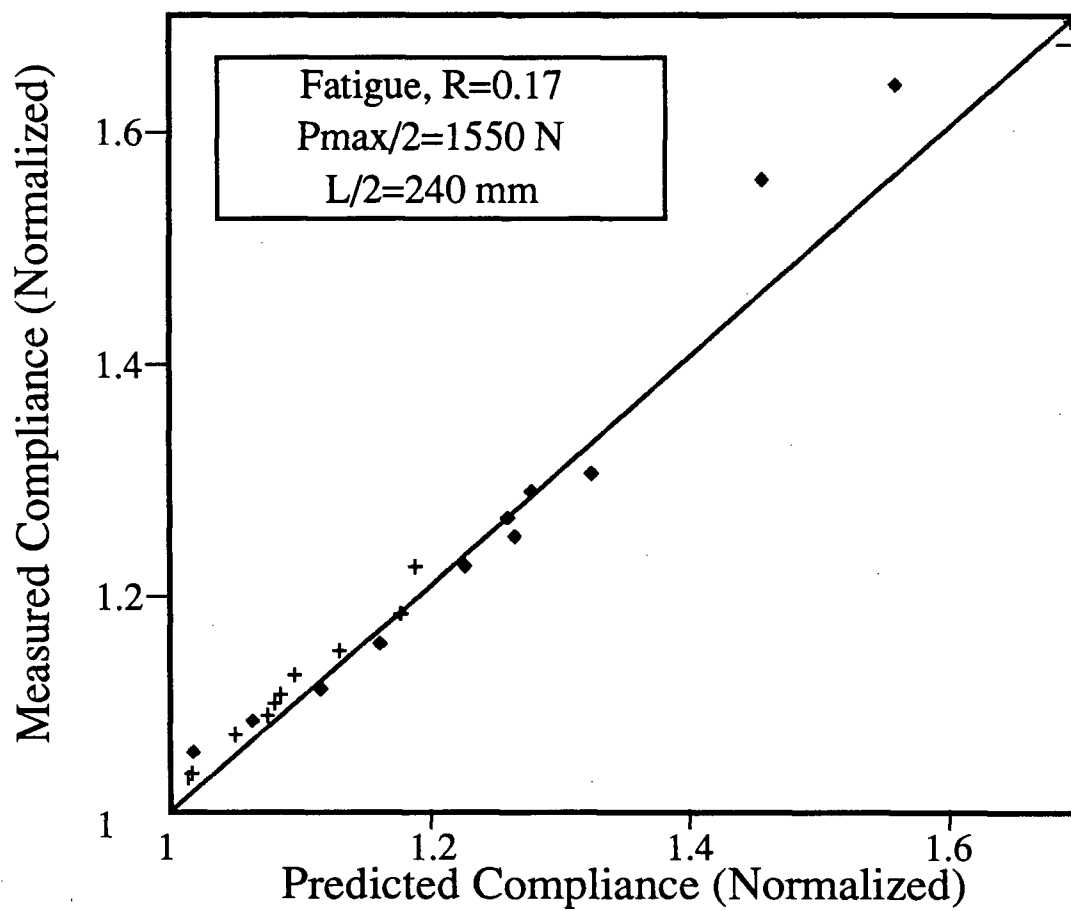


Figure 3.24 Measured vs. predicted compliance for type III rods, $R=0.17$. The straight line represents ideal agreement between prediction and experiment.

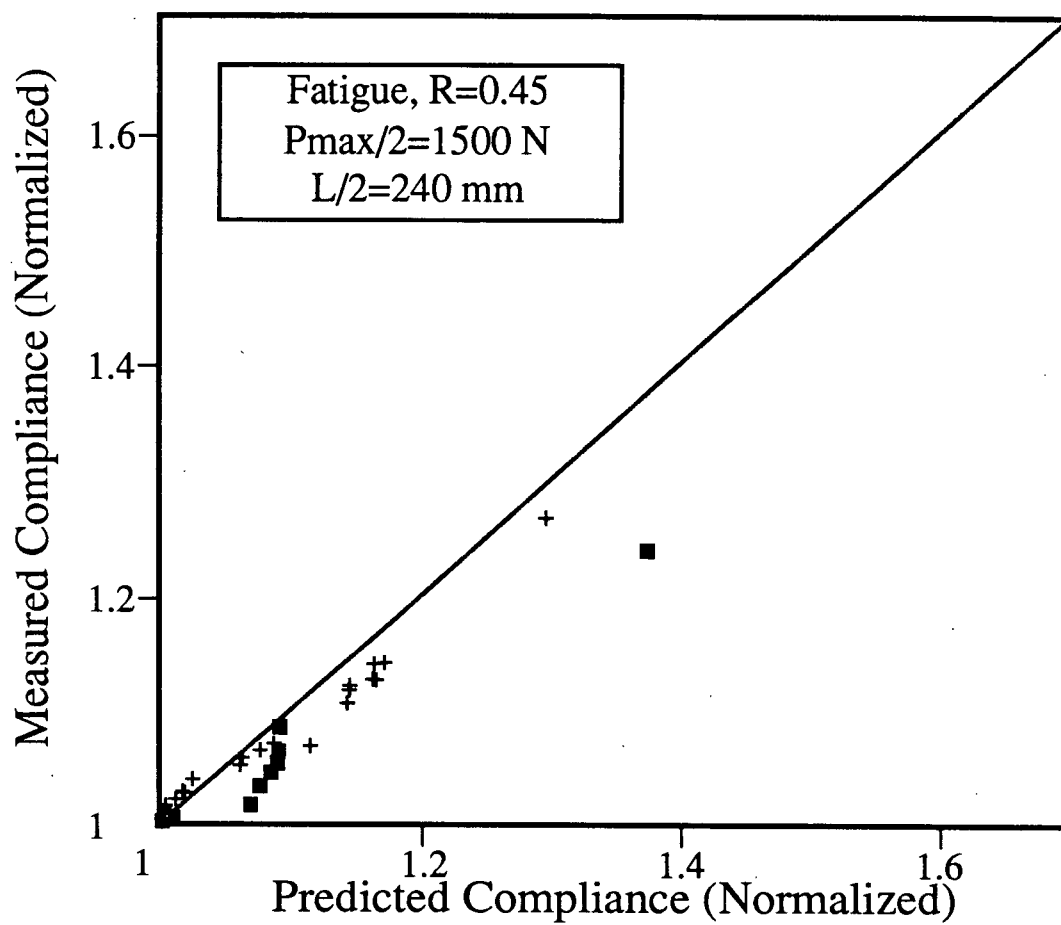


Figure 3.25 Measured vs. predicted compliance for type III rods, $R=0.45$. The straight line represents ideal agreement between prediction and experiment.

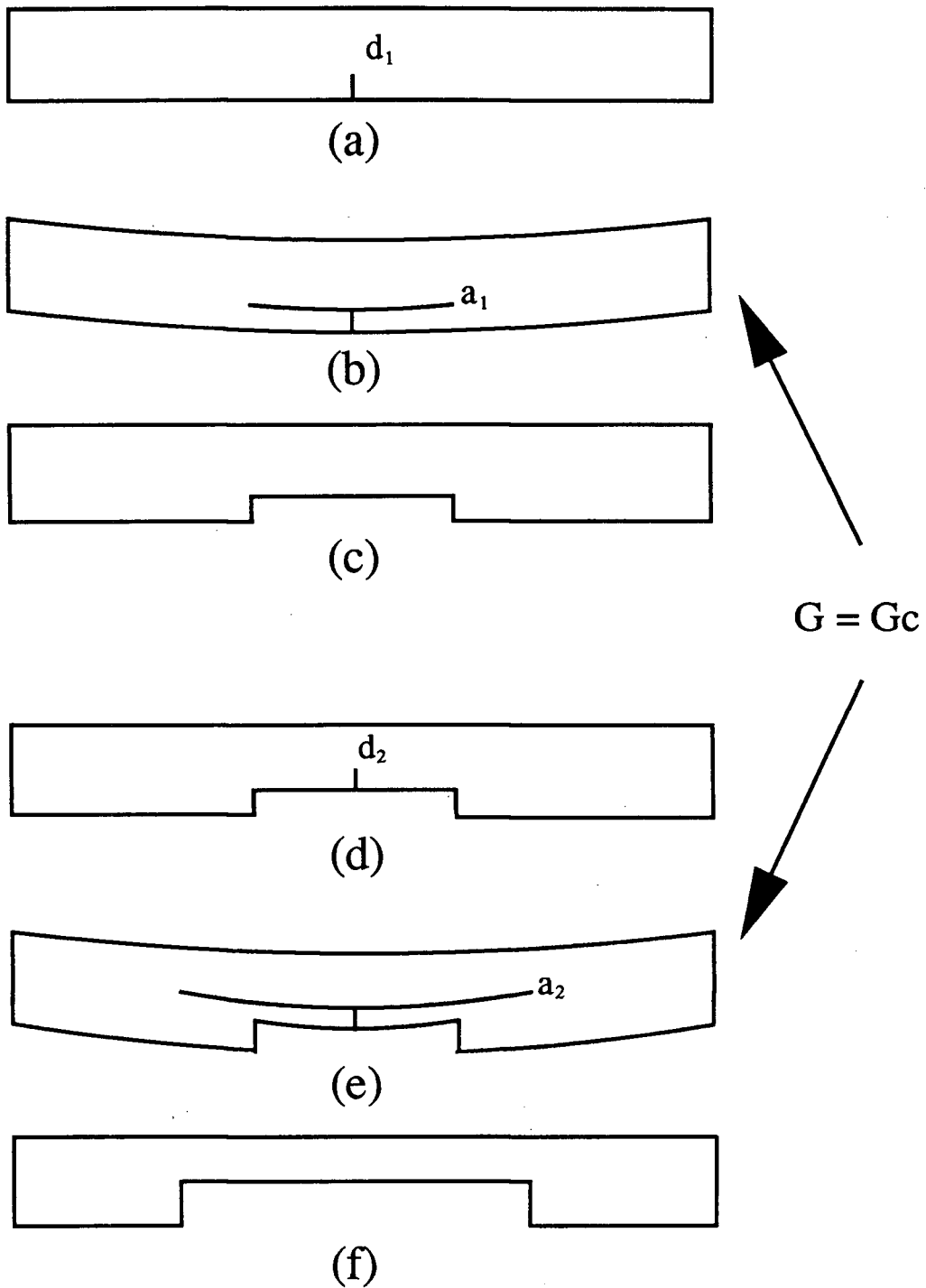


Figure 3.26 Damage growth hypothesis.

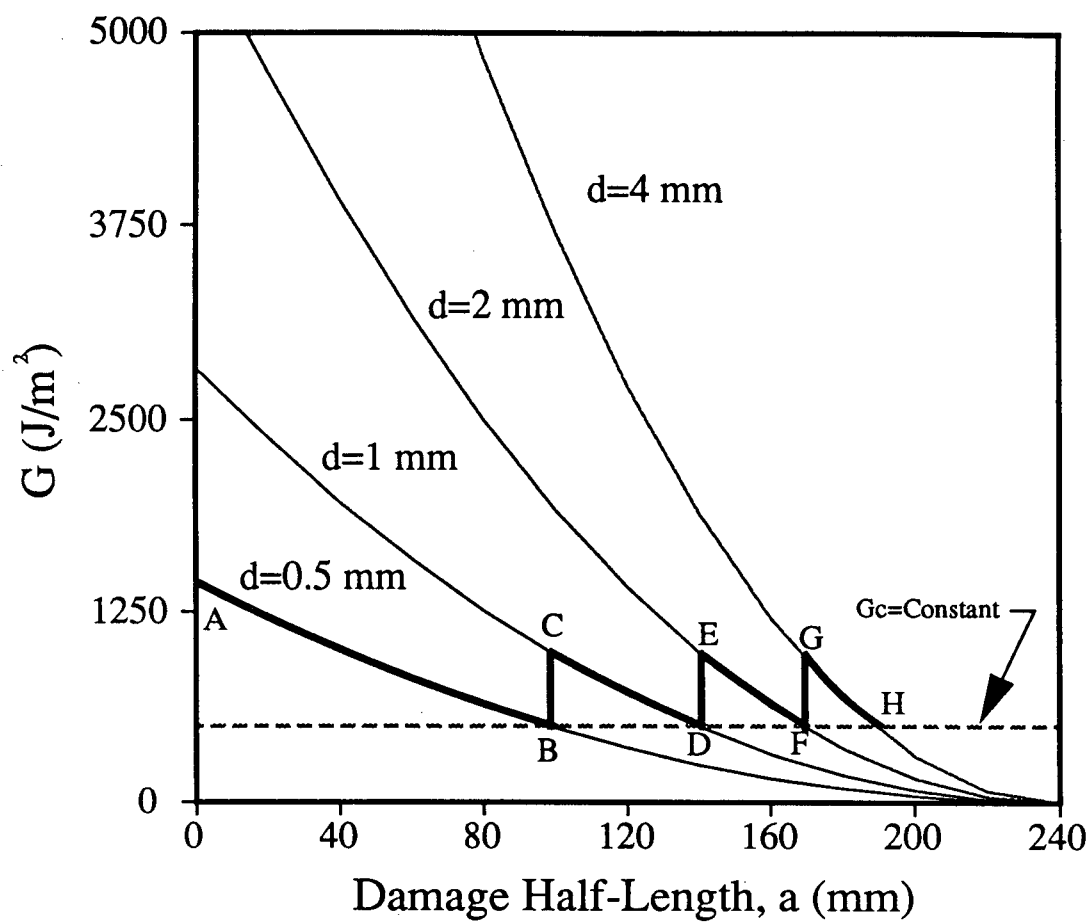


Figure 3.27 Growth in damage length at constant lengthwise crack resistance, G_c .

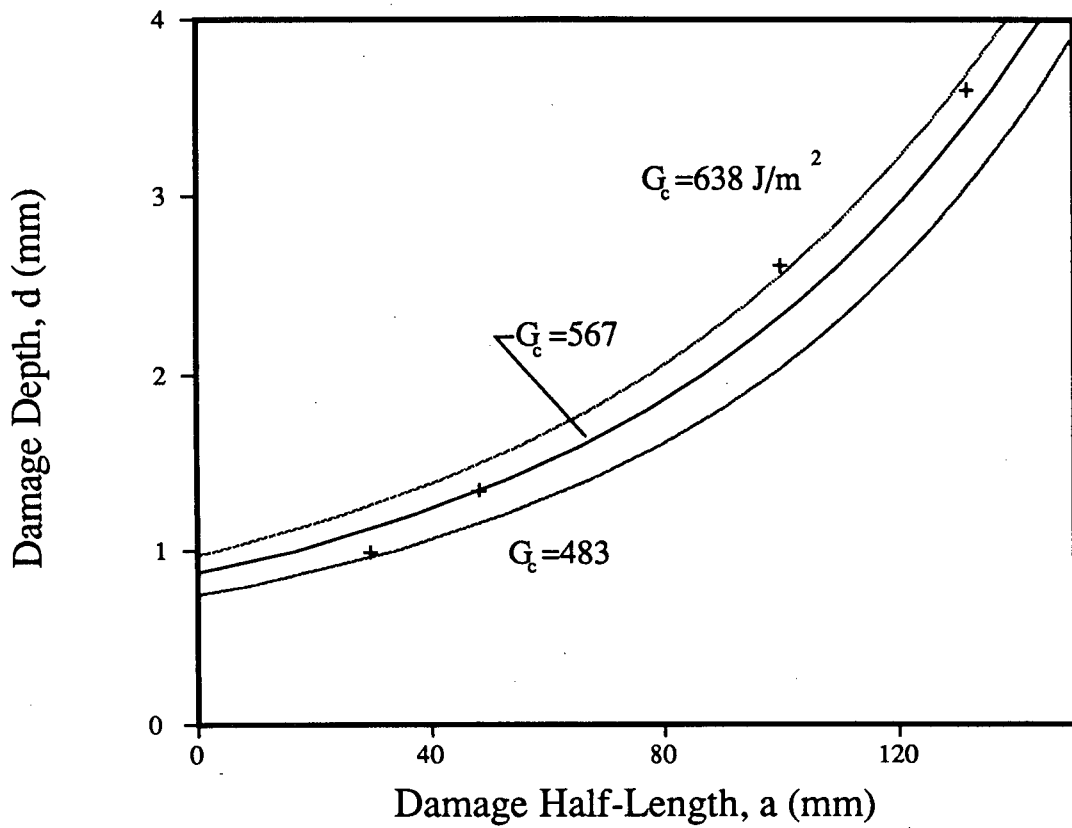


Figure 3.28 Relation between damage depth and length, type I rod, static loading. $P/2=700 \text{ N}$, $l/2=240 \text{ mm}$.

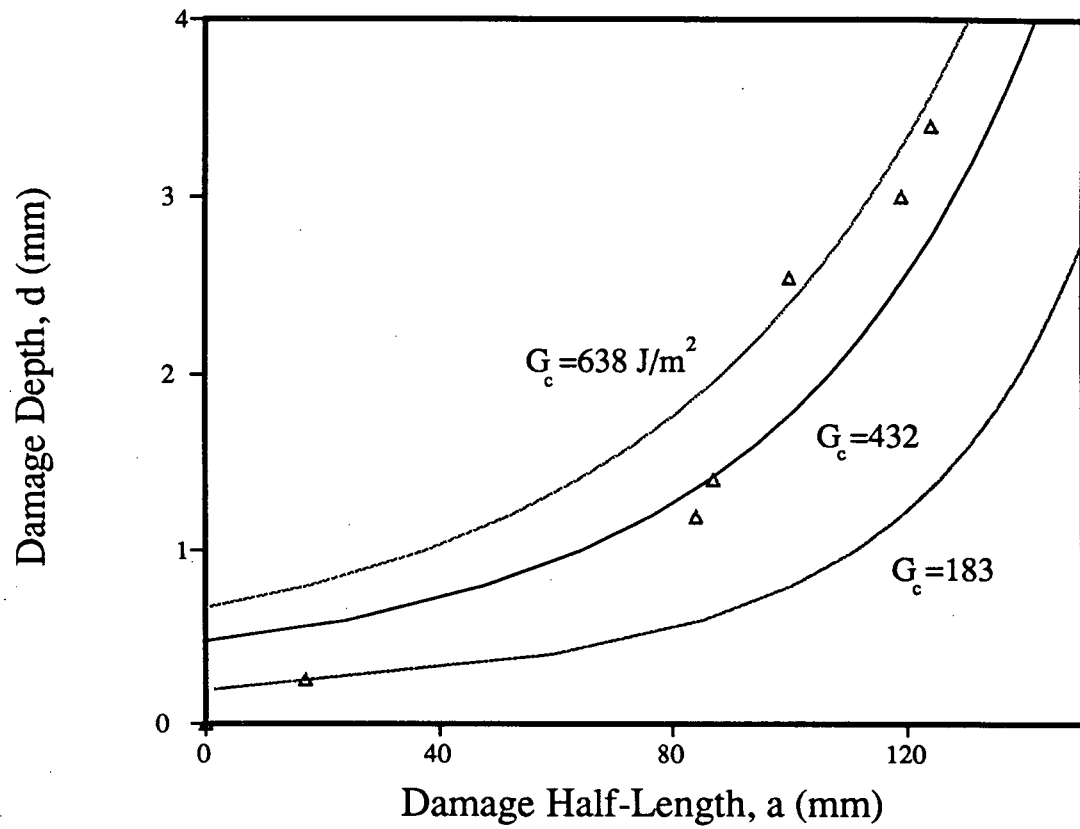


Figure 3.29 Relation between damage depth and length, type I rod, static loading. $P/2=1000 \text{ N}$, $l/2=200 \text{ mm}$.

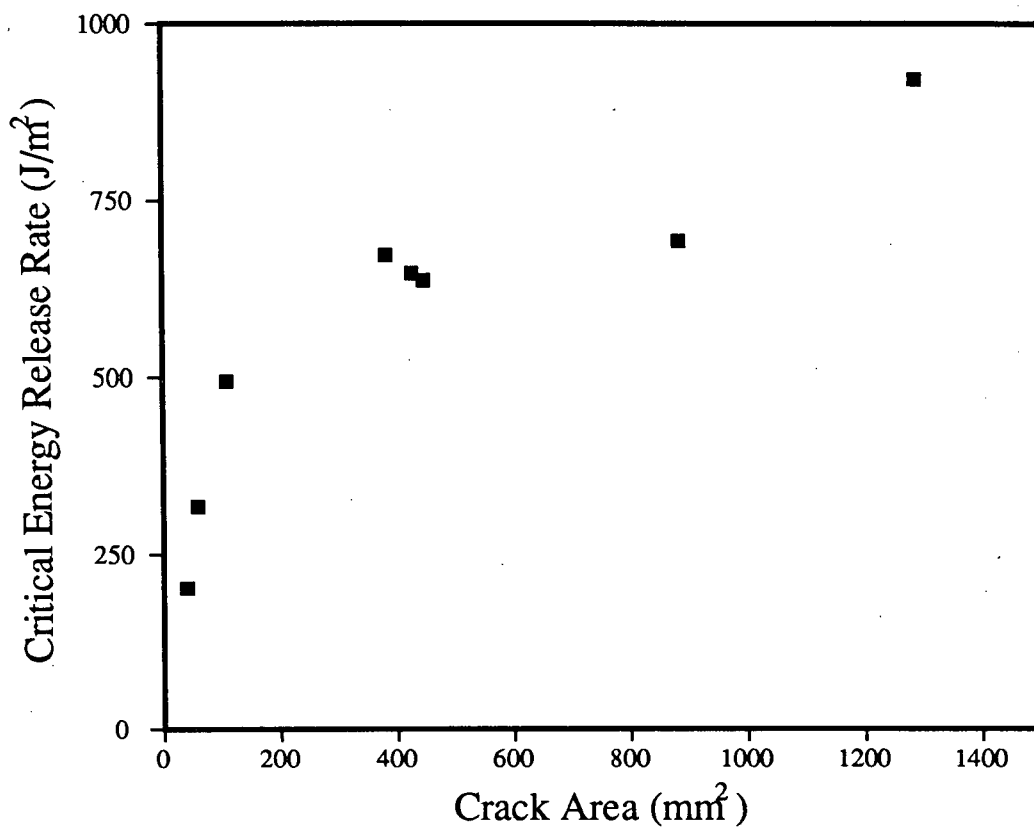


Figure 3.30 Increase in critical energy release rate with increase in longitudinal crack area, type II rod, static loading.

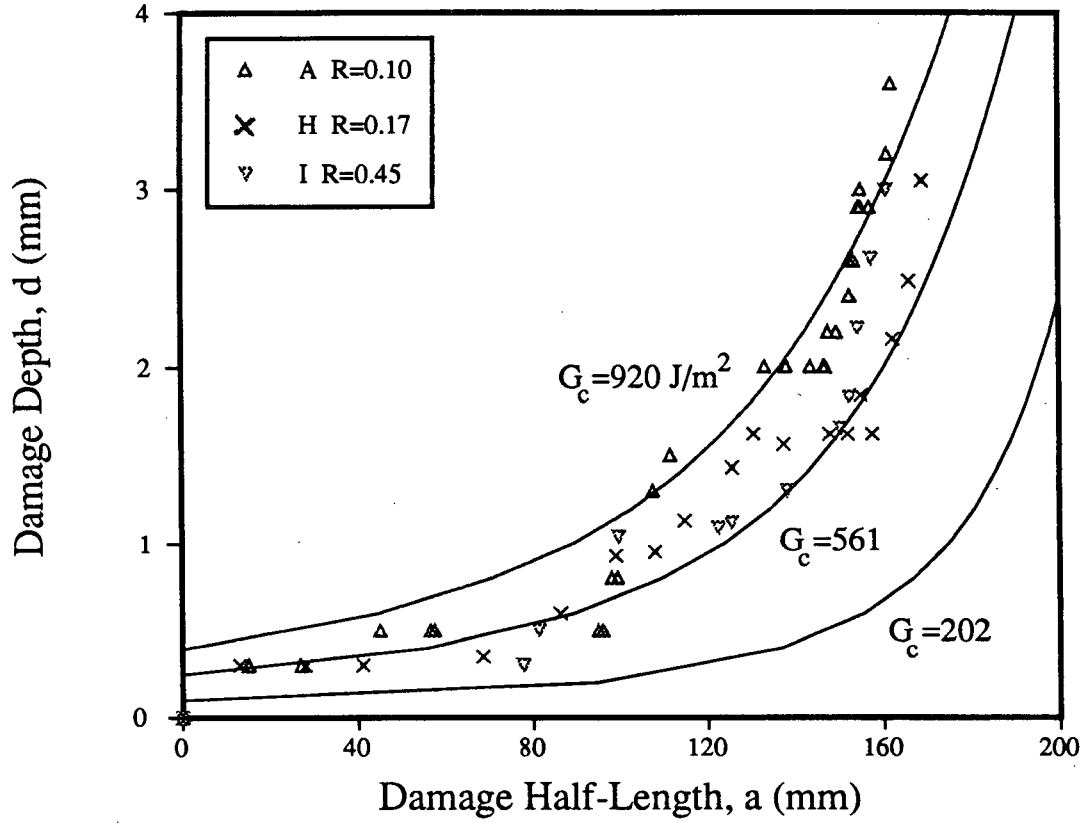


Figure 3.31 Relation between damage depth and length, type II rods, cyclic loading.

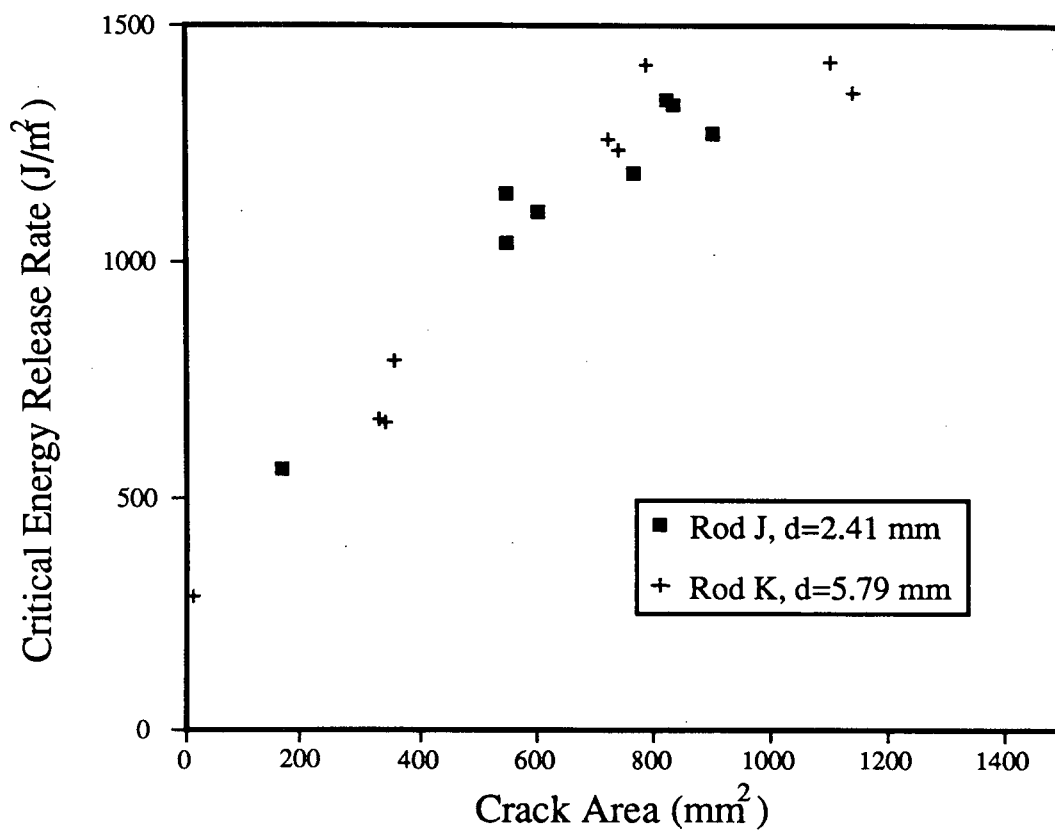


Figure 3.32 Increase in critical energy release rate with increase in longitudinal crack area, type III rods, static loading.

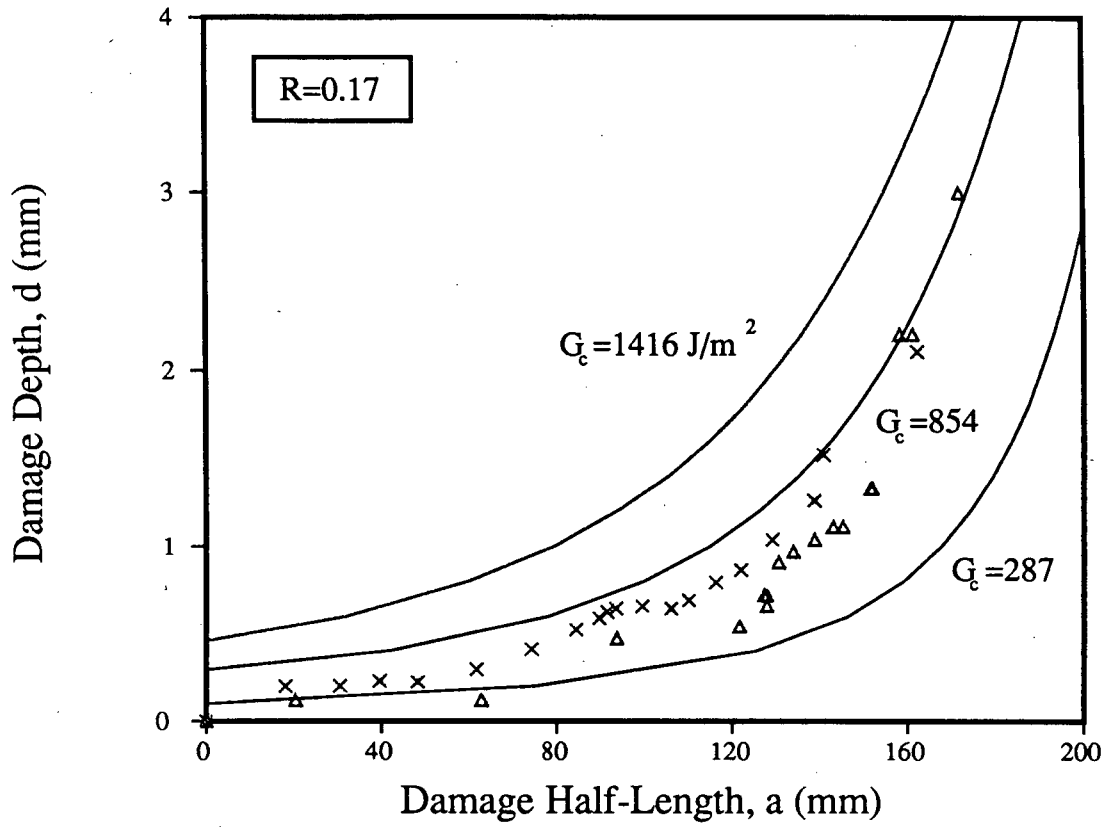


Figure 3.33 Relation between damage depth and length, type III rods, cyclic loading.

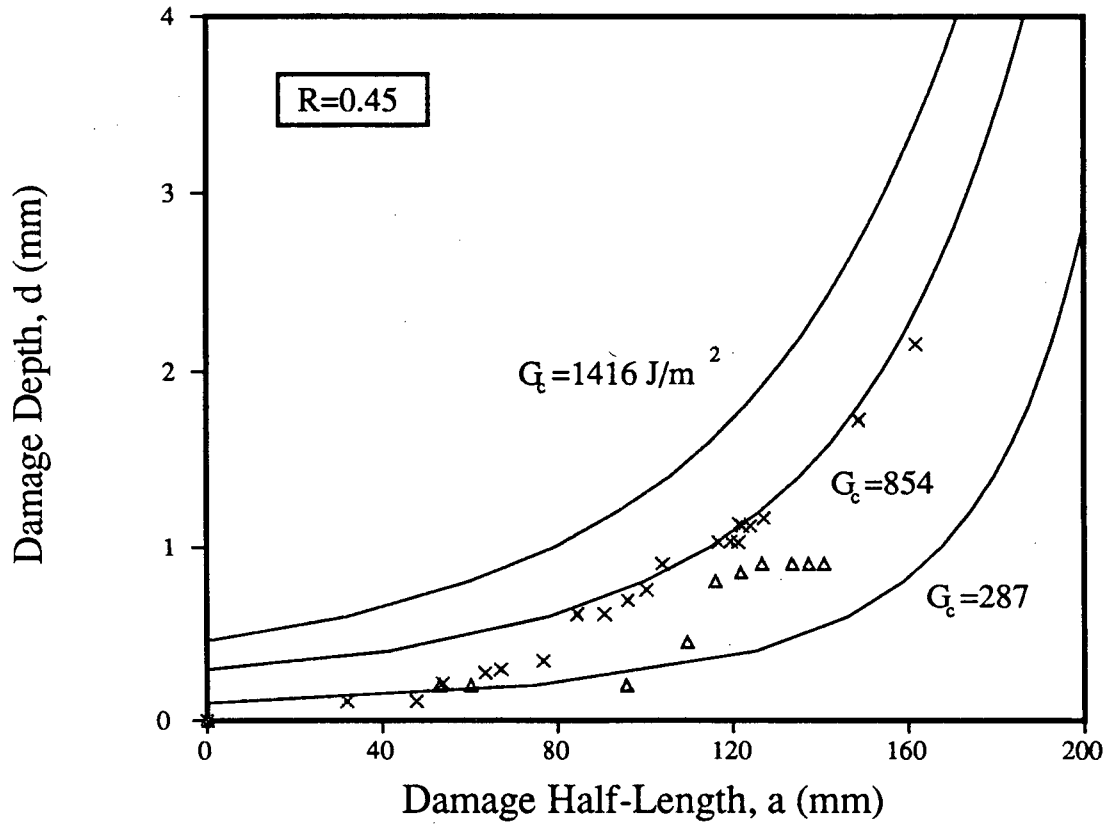


Figure 3.34 Relation between damage depth and length, Type III rods, cyclic loading.

4 FRACTURE AND FATIGUE OF CROSS-PLY COMPOSITE BEAMS

Tests similar to those performed on the rods in chapter three were performed on fibreglass beams sectioned from aerial personnel vehicle booms supplied by B.C. Hydro. The rectangular beams had fibres oriented in directions parallel and perpendicular to the beam longitudinal axis, representing a more general class of composites than the unidirectional rods.

4.1 Experimental Procedure

Boom construction consists of an 18.5 mm layer of E-glass and polyester resin which is built up around a 20 cm by 20 cm square mandrel, cured and removed from the mandrel. A 600 mm long hollow rectangular section of a box beam was cut into 600 mm by 50 mm by 18 mm test samples as shown in figure 4.1. The bottom of the samples (inside of the boom) had a 2.5 mm layer of resin-rich random mat material which was removed by notching this layer, loading the sample notched side down in the bending apparatus and peeling off the ply. All bending was done at a 480 mm span on samples 16 mm deep, thus the span to depth ratio was 30:1.

To determine the stacking sequence accurately a small section was cut transverse to the longitudinal axis, polished and photographed. From the photograph the stacking sequence and individual ply thicknesses were accurately determined, figure 4.2. The stacking sequence was unsymmetric, $[(0/90)_4/0]$; the top four 0 degree plies were each 2.5 mm thick, the bottom 0 degree ply was 3 mm thick and all the 90 degree plies were 0.5 mm thick.

Static and cyclic testing proceeded as in the previous chapter using the MTS servohydraulic fatigue machine controlled by an IBM PC. An 18 mm diameter steel roller was used to apply loads at the central load point which helped prevent crushing on the

compression side. In spite of this precaution some experimental difficulties were encountered. Using such thick samples allowed damage growth in the depth direction to be observed but also lead to considerable loads being applied. Too high a load caused the sample to fail catastrophically, either following degradation of the bottom ply or by crushing beneath the central load point. Conversely, too low a load lead to a formidable amount of acoustic emission data being gathered (see chapter 5). Due to the large deflections and corresponding large ram travel cycling was done at only 0.1 to 0.3 Hz.

4.2 Results

Three laminates were tested under cyclic loading conditions. The tests are summarized in table 4.1.

Table 4.1. Laminate test conditions.

Specimen	P_{\max} (N)	Load Ratio	Cycles
J	2000	0.30	12,000
K	1000	0.25	25,417
L	1200	0.10	450

* Damage depth produced artificially

Laminates J and K were tested under cyclic loading. After 11,000 cycles a longitudinal split on the tension side at one edge initiated in sample J. Initiation in these samples was distinct from the rods as it was not constrained to occur at one single point. Another 1000 cycles grew the damage across the tensile surface from edge to edge and in the length direction. Further cycling caused the sample to crush beneath the central load point followed closely by complete failure.

Sample K took 10,977 cycles to initiate damage on the tension side. This first appeared as a zone 61 mm long, 0.7 mm deep over a width of 4.5 mm starting at one of the bottom edges. At 11,176 cycles crushing damage initiated on top at the central load point. This appeared as a zone 169 mm long 2.5 mm deep (to the bottom of the top ply) from edge to edge. To salvage the experiment the sample was turned over so that the crushing damage was on the tension side. After a 25,417 cycles the damage on the bottom had grown to 318.8 mm in length and 3.4 mm in depth and the damage on the top had not grown. Once turned over the crush zone on the top grew on the bottom; consistent with unidirectional rod behaviour the compliance of the laminate increased as the number of cycles and damage zone size increased, figure 4.3.

From this limited data it appears that there are more than two damage parameters. Damage initiated at one corner and grew towards the opposing edge as well as in length and depth directions. In contrast damage initiated in the circular cross section rods at one point and grew in only two dimensions, suppressing any tendency to grow in another direction, as in the rectangular laminate.

Initiation irregularities were overcome using a technique similar to that used for the static tests on the rods for sample L. Damage depth was induced artificially every 50 to 100 cycles using a hack saw. A shallow notch in the tension side directly beneath the central load point eliminated the tendency of damage to initiate at the bottom edges. Damage grew in the length direction at the depth of the notch root as the sample was loaded slowly to 1200 N. The load cycle was repeated fifty times at $R=0.10$, the notch deepened, and the cycles repeated. At a final notch depth of 5.17 mm and total damage length of 218 mm the laminate could no longer support the load and failed by breaking in half. During each stage the depth remained constant over the entire damage length. The load sequence and damage parameters are shown in table 4.2.

Table 4.2. Damage growth in Laminate L.

Cycles	Half- Length (mm)	Depth (mm)	Compliance (mm/N)
0	0	0	0.0127
50	0	0.49	0.0127
100	33	1.08	0.0133
200	52	1.81	0.0138
300	63	2.94	0.0140
350	218	4.31	0.0269
400	218	5.17	0.0332

As with the rods, it was clear from this test that damage would grow in the length direction once damage in the depth direction was present and a certain load was reached. Also, similar to the rods, damage in the length direction stopped upon reaching a certain length at a certain damage depth and maximum load; the damage length at each damage depth in table 4.2 was reached after only two or three cycles. Very little damage growth was observed until the depth was increased.

4.3 Stiffness Reduction

For the static test and for the cyclic test after some initial damage, the damage state can once again be described by a length a and a depth d . Based on these two parameters the compliance may be predicted by an analysis similar to the analysis of the rods. However, since the laminates are orthotropic an isotropic solution cannot be used. Instead, four independent material constants (E_L , E_T , G_{LT} , ν_{LT}) must be taken into account for the

compliance model. Classical laminated plate theory [62] provides the link between the four independent material constants, the applied load, the bending geometry and compliance.

For plates, of which the beams are a special case, it is customary to deal with plate curvatures k . Deflections w are found in one dimension from

$$\frac{d^2w}{dx^2} = k_x \quad (4.1)$$

From the contracted notation of Jones [69], the constitutive equation relating strains, curvatures and loading conditions is

$$\begin{pmatrix} e^0 \\ k \end{pmatrix} = \begin{pmatrix} A' & B' \\ B' & D' \end{pmatrix} \begin{pmatrix} N \\ M \end{pmatrix} \quad (4.2)$$

where e^0 is a 3x1 matrix of mid-plane strains, k is a 3x1 matrix of plate curvatures, N and M are 3x1 matrices of load and moment per unit width and A' , B' and D' are 3x3 matrices dependent on stacking sequence and the four independent material constants. Since only the plate curvatures are of interest

$$\begin{pmatrix} k_x \\ k_y \\ k_{xy} \end{pmatrix} = B'N + D'M \quad (4.3)$$

Since no forces act in the horizontal plane of the laminate $[N]$ reduces to zero. The curvatures are related to the applied moments by expanding the D' matrix

$$\begin{pmatrix} k_x \\ k_y \\ k_{xy} \end{pmatrix} = \begin{pmatrix} D'_{11} & D'_{12} & D'_{16} \\ D'_{12} & D'_{22} & D'_{26} \\ D'_{16} & D'_{26} & D'_{66} \end{pmatrix} \begin{pmatrix} M_x \\ M_y \\ M_{xy} \end{pmatrix} \quad (4.4)$$

From Eq. (2.2) $M_x = Px$ and both M_y and M_{xy} are zero. Thus, from Eq. (4.4) and (4.1)

$$k_x = D'_{11}M_x \quad (4.5)$$

$$\frac{d^2w}{dx^2} = D'_{11}M_x \quad (4.6)$$

As mentioned M_x is the moment per unit width, M/b . Equation (4.6) then becomes

$$\frac{d^2w}{dx^2} = \frac{D'_{11}}{b}M \quad (4.7)$$

This result is identical to Eqs. (3.1) and (3.5) with D'_{11}/b replacing $1/EI$. Therefore the compliance of the laminates may be written

$$C = \frac{1}{b}(a^3 - 3la^2 + 3l^2a)D'_{11} + (l-a)^3D'_{11} \quad (4.8)$$

In the above equation ${}_1D'_{11}$ and ${}_2D'_{11}$ represent values from the undamaged and damaged sections of the beam. For the undamaged part, the original stacking sequence is used. For the damaged part the depth alters the original stacking sequence by removing part of it.

4.3.1 Comparison with Experiment

For each measured damage depth the value of ${}_2D'_{11}$ was calculated using the dimensions of figure 4.1 and laminated plate theory. For a cross ply laminate three independent material constants are incorporated into D'_{11} : E_{11} , the extensional modulus, E_{22} , the transverse modulus and ν , the Poisson's ratio. From one initial value of compliance all three parameters cannot be determined. The values shown in table 4.3 were estimated from the overall fibre volume fraction (38%), the mechanical properties of E-glass and the principles of micromechanics (see Appendix C).

Table 4.3. Material properties used to determine D'_{11} .

Quantity	Symbol	Value
Extensional Modulus	E_{11}	31.0
Transverse Modulus	E_{22}	9.1
Poisson's Ratio	ν	0.3

These values and the damage length were input to Eq. (4.8) for the two laminates that tested successfully. The predicted values are compared to the measured values in figure 4.4. For both tests the experimental and predicted values agree closely. For the cyclic loading test the values include compliance changes that occurred only after the laminate was turned over so that the crushing damage was on the tension side.

4.4 Energy Release Rate

The energy release rate for crack extension follows the same derivation as in chapter three and is the same as Eq. 3.22 with $1/EI$ replaced by D'_{11}/b

$$G = \frac{P^2(l-a)^2}{2b^2} (D'_{11} - \frac{1}{2}D'_{11}) \quad (4.9)$$

As in chapter three the crack is assumed to extend when G from Eq. (4.9) exceeds the lengthwise crack resistance G_c . For these laminates the crack plane may grow through plies with fibres parallel to the longitudinal axis, as with the rods, or through plies with fibres perpendicular to the longitudinal axis. Thus the value of G_c is expected to vary with damage depth, corresponding to the ply type through which the longitudinal crack grows, and with the length due to fibre bridging.

Numerical values of G_c were evaluated as in chapter three, by use of Eq. (4.9) with the relevant values of material and damage parameters for laminate L. In all plies the crack grew longitudinally allowing measurement of G_c for these plies. Four out of five damage depths extended into 0 degree plies; only one damage depth reached part way into a 90 degree ply. Figure 4.5 shows the critical energy release rate as a function of crack area. The critical energy release rate for crack growth in the 0 degree plies began at $G_c=200 \text{ J/m}^2$, increased as damage length increased, and levelled off at about 400 J/m^2 . The energy release rate in the 90 degree ply was higher, approximately 600 J/m^2 , as indicated in the figure.

4.5 Damage Development

From the limited amount of data it is difficult to draw any firm conclusions regarding the relation between damage parameters in the laminated beams. G_c increases as a function of crack length, and as plies at different angles become part of the damage zone. In this case the length happened to grow beyond the previous length as the depth increased; however, if G_c increases as depth increases the crack length may be shorter at increasing depths which would invalidate the two parameter non-uniform cantilever beam model.

Maximizing life under given cyclic loading conditions is equivalent to minimizing the rate of increase of compliance. The minimum increase in compliance is achieved with the slowest growth in depth and length. From previous studies of unidirectional composites [15] it is clear that damage will grow rapidly in the depth direction for 90 degree plies and slowly for 0 degree plies. However from these results it is apparent that the longitudinal crack resistance is higher for 90 degree plies than for 0 degree plies. Therefore simultaneous slow growth in the depth direction and length direction cannot be achieved with 0 or 90 degree plies. Plies at angles other than 0 and 90 degrees may minimize the rate of increase in compliance if they do not introduce interply delamination. It may be

worth noting that the major manufacturers and users of composite beams to date, the automobile manufacturers, use only unidirectional beams with the fibres in the longitudinal direction for leaf spring applications.

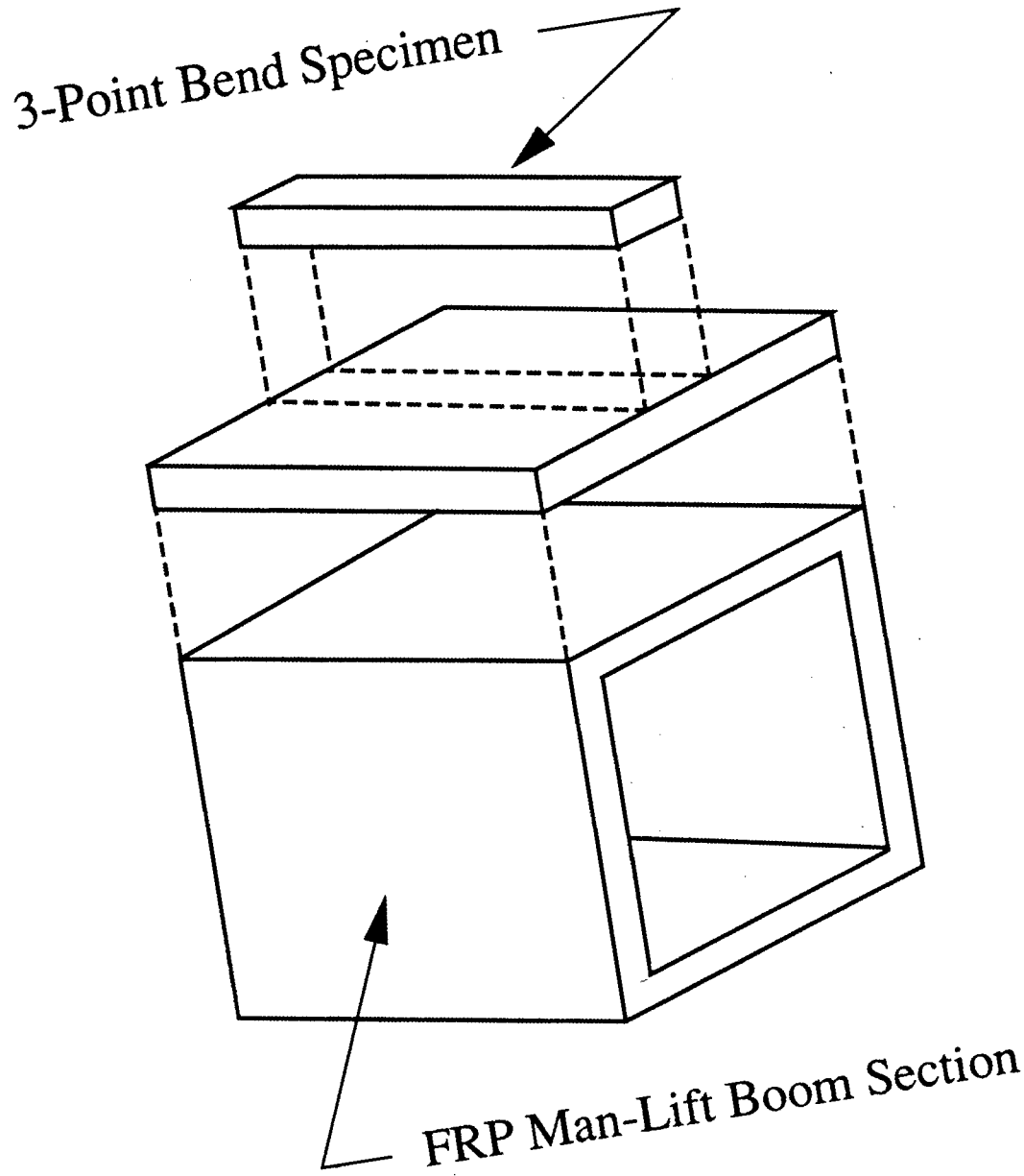


Figure 4.1

Test sample cut from glass reinforced polyester man-lift boom.

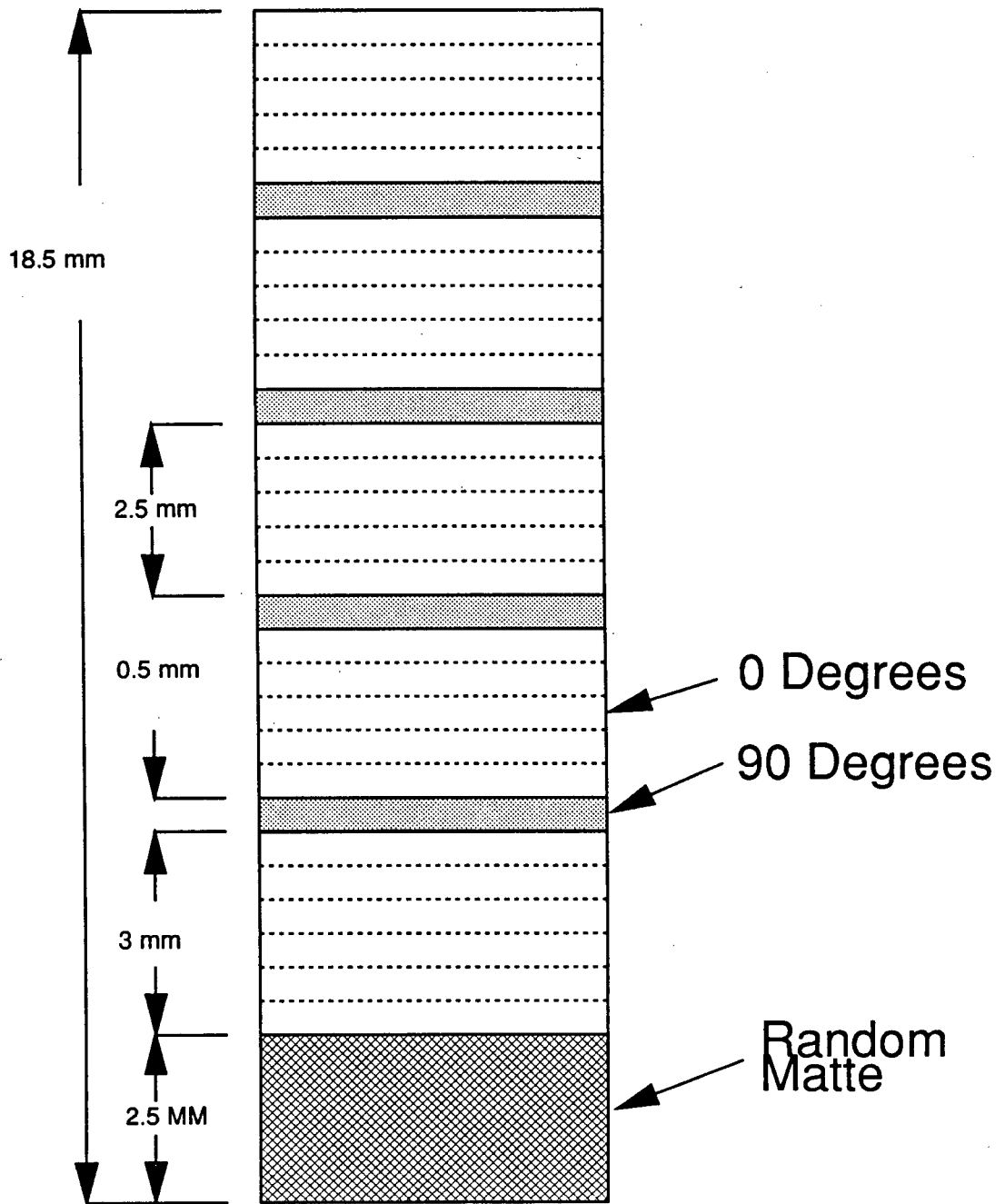


Figure 4.2 Laminate edge.

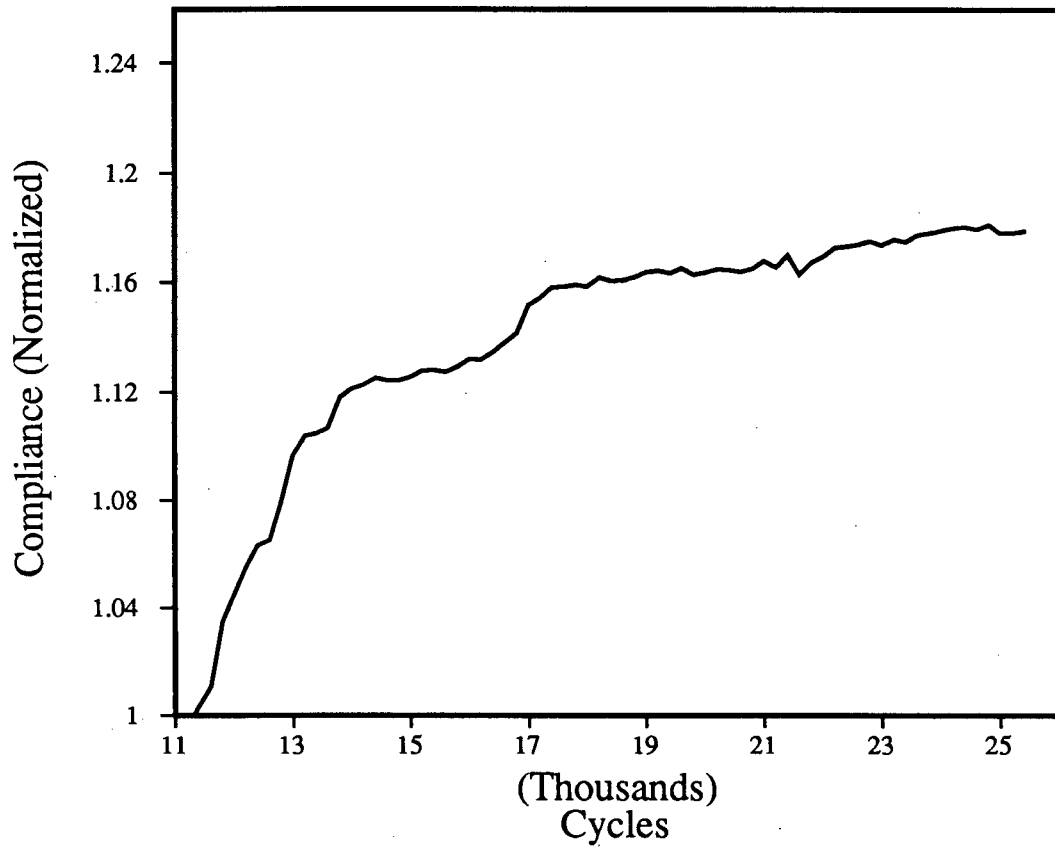


Figure 4.3

Increase in compliance as a function of cycles, laminate K.

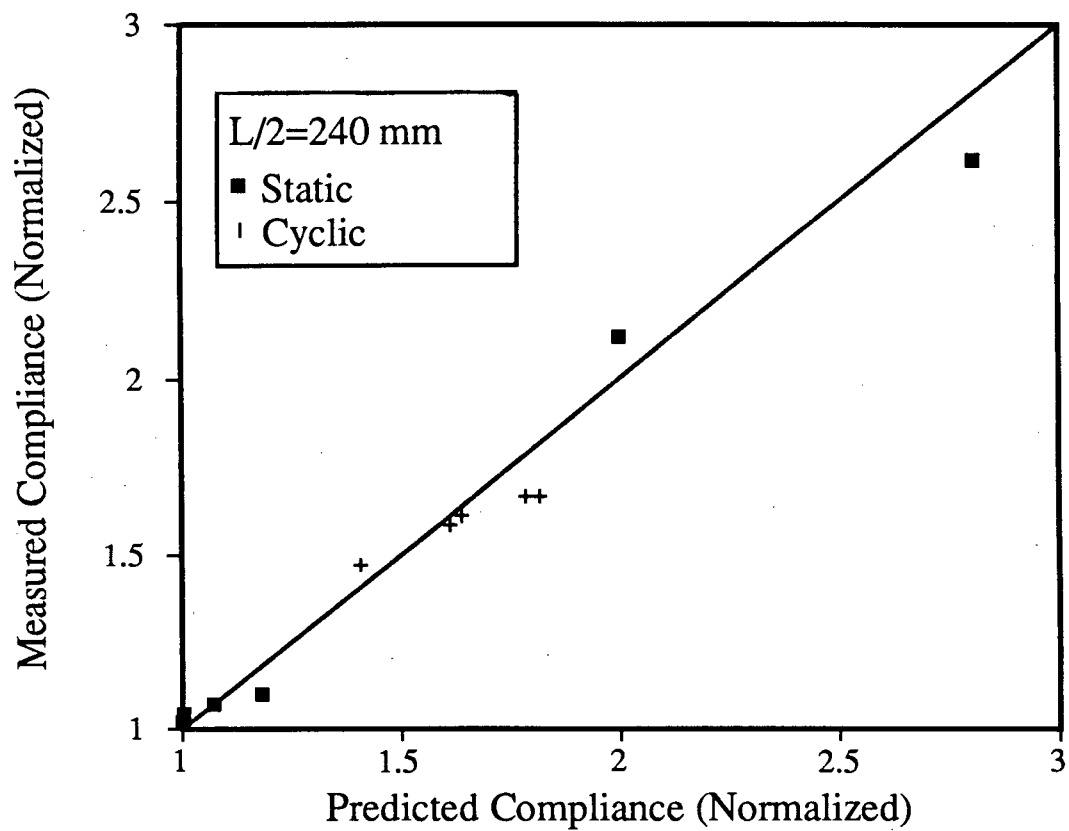


Figure 4.4 Measured vs. predicted compliance, laminates K and L. The solid line represents ideal agreement between theory and experiment.

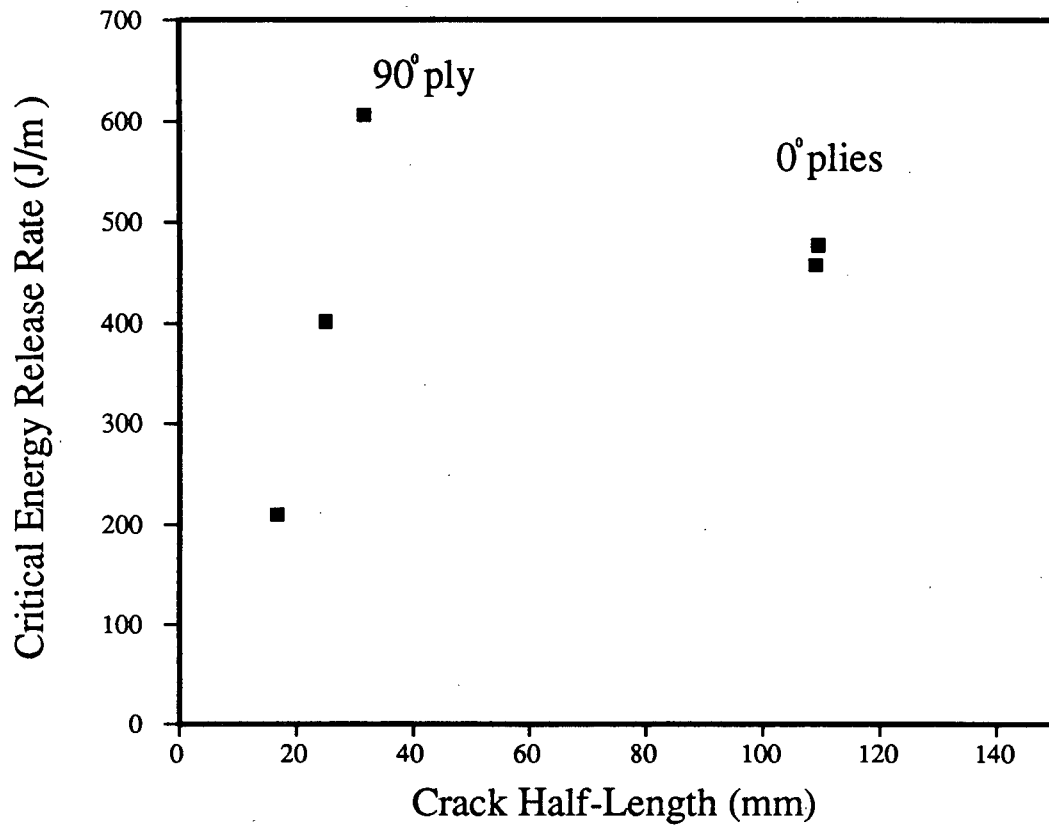


Figure 4.5 Critical energy release rate as a function of damage length, Laminate L.

5 DAMAGE DETECTION

Up to this point only the damage mechanisms have been discussed for static and cyclic bending. The damage state, in most cases, can be measured by a crack length, a crack depth and the compliance. However the visual methods of measuring the damage dimensions and the procedure for measuring compliance may not always be applied in service. Acoustic emission (AE) has received attention as a method of detecting damage in composites and is the subject of this chapter.

Much of the previous work on damage monitoring with AE concerns correlations between AE activity and damage mechanisms. For instance many of the examples cited in chapter 2 made use of the five AE signal parameters or other descriptors to discriminate fibre fracture, delamination and matrix cracking. In contrast, AE will be used in this chapter to indicate damage initiation, compliance, damage length and damage depth.

5.1 Experimental Procedure

Acoustic emissions were recorded for each of the rods during cyclic loading tests in chapter 3 and both laminates in chapter 4 with a Physical Acoustics Corporation 3004 system. Figure 5.1 shows the experimental setup schematically. One, two or three PAC R15 150 kHz resonant transducers were used, depending on the test. The transducers were attached to each specimen with standard grease couplant. Contact pressure between the sample and the transducer, essential in obtaining reliable results, was maintained by rubber bands and specially fabricated teflon holders. Each transducer was connected to its own preamplifier operating at 40 dB gain with a 100-300 kHz band-pass filter. Only signals in the 100-300 kHz range were recorded; machine noise, which occurs at a much lower frequency, was not recorded. A second amplifier, one on each channel, allowed a further

gain of 3 to 49 dB. This variable gain in conjunction with a threshold voltage setting combine to define the threshold setting in dB. All tests were run at either 60 or 71 dB threshold.

All waveforms received by the system had the five AE parameters (amplitude, duration, counts, energy, rise time) extracted and stored on floppy or hard disk for post-test analysis. The analysis was done after testing with the PAC equipment by plotting events, cumulative events, logarithm of cumulative events, etc., versus any of the five AE parameters. Events versus location was also possible when two sensors were used. Post-processing programs were used to discard or "filter" unwanted events, such as those below a certain amplitude or energy.

5.2 Damage Initiation

In all cases damage initiation could be observed by the onset of acoustic emissions, appearance of visual damage and an increase in compliance. Rods A, E and I and laminate J were chosen as representative of the samples tested. The cycle number and event rate (events per cycle) for each of the three indicators of initiation are summarized in table 5.1.

Table 5.1 Damage Initiation.

Sample	AE Threshold (dB)	Initiation					
		First AE Events		Visual (matrix crazing)		Compliance Increase	
		Cycle	Event Rate	Cycle	Event Rate	Cycle	Event Rate
Rod A	71	1100	0.60	1500	0.36	1700	7.92
Rod E	60	1600	0.18	1600	0.18	2000	2.31
Rod I	60	600	0.15	800	0.64	1000	29.30
Laminate J	60	1400	0.17	10902	0.34	11114	0.45

A type II rod, sample A, was tested using one sensor and a threshold of 71 dB. Figure 5.2 shows cumulative acoustic emissions and percent increase in compliance as a function of cycles. Acoustic emissions first appeared between 1000-1100 cycles where 27 events were recorded. At 1500 cycles damage was observed visually in the form of four light colored spots in the area beneath the central load point, all less than 1 mm in length. The first increase in compliance was recorded at 1700 cycles when two of the four spots grew into longitudinal splits with the associated fibre breaks. The first events were not correlated with either visual damage or compliance change and their source is therefore uncertain, but even at this low sensitivity AE provided an early warning that damage was occurring. At the onset of emissions the event rate was approximately 0.60 events per cycle. At the onset of visual damage the rate dropped to 0.48 events/cycle. The increase in compliance was marked by an increase in event rate to 7.92 events/cycle. For the rods damage grew as longitudinal splits with separation of fibres and creation of new damage surfaces. It is likely that the increase in event rate was due to friction between the newly created damage surfaces.

Sample I, also type II, was tested at a 60 dB threshold. Here the onset of emissions occurred at 600 cycles and 0.15 events/cycle, figure 5.3. Visual damage followed 200 cycles later at 0.64 events/cycle. Compliance increased after a further 200 cycles with an increase in event rate to 29.3 events/cycle. The loading conditions differed for samples A and I so little can be said regarding the intervals between first emissions, visual damage and increase in compliance for the two samples. In both cases, however, AE was successful in detecting damage initiation.

One of the type III rods, sample E, was tested at a threshold of 60 dB. Both the onset of emissions and visual damage coincided at 1600 cycles. An increase in compliance was recorded 400 cycles later, figure 5.4. Between initiation and change in compliance the event rate jumped from 0.18 events/cycle to 2.31 events/cycle.

Useful initiation data was recorded for only one of the laminates tested. Using a threshold of 60 dB the first emissions occurred at 1400 cycles, followed by visual damage at 10,977 cycles and a change in compliance at 11,176 cycles, figure 5.5. The event rate, 0.17 to 0.45 events/cycle, was nearly constant throughout, even following the increase in compliance. With this sample the damage initiated by crushing at the central load point. The damage grew in large clumps rather than the smaller fibre bundles observed in the rods. This clump-like failure lead to an absence of new damage surfaces, even though a large damage volume was created. The lack of new damage surfaces likely lead to a corresponding absence of friction noise which may be the reason that the event rate did not increase.

5.3 Compliance

Figure 5.6 shows a series of amplitude distributions for sample A. Each histogram represents the events recorded at a specific one hundred cycle interval. The first events were recorded between 1000 and 1100 cycles. As the threshold was 71 dB, no events below this value were recorded. Most events were centred around 75 dB with a few high amplitude events. Hereafter, the distribution changed in size as the event rate increased up to 3500 cycles. Except for a few more high amplitude events the distribution is relatively unchanged in shape.

Figure 5.7 shows the same series of histograms for AE energy. For the initial one hundred cycle interval most events were low in energy. For successive intervals the number of high energy events increased, with some very high energy events recorded after 3500 cycles. Intervals (d,e,f) in figure 5.9 have in excess of 10,000 events with an energy value less than 5. In general there were a large number of events recorded with energies less than 20, but these events appeared to be due to friction between broken fibres as they rubbed each other during cycling. In figure 5.8 only those events with an energy level above 100 are counted in a simple attempt to discard events caused by friction. The cumulative number of events having an energy greater than 100 will be referred to as N_{100} . In figure 5.8 the number of events remaining is only a small fraction of the number recorded.

By retaining only those events with high energy values it was hypothesized that only events associated with fibre fracture would remain such that all remaining events could be considered as single fibre fracture events. In the present geometry, fibre fracture occurs

predominantly under the central load point and thus the cross-sectional area of the damage is proportional to the number of fibre breaks. The cross section area damaged was discussed in chapter 3 and is represented by

$$A_d = \frac{r^2}{2} \left(\pi - 2 \sin^{-1} \left(\frac{r-d}{r} \right) \right) - (r-d) \sqrt{2rd - d^2} \quad (5.1)$$

AE events with energy greater than 100 are plotted as a function of Eq.(5.1) in figure 5.9. The relation is linear, supporting the assumption that high energy events are associated with fibre fracture. That is, the number of fibre breaks is directly proportional to the damaged cross-section area and to the number of events with energy greater than 100. The damaged area is a linear function of the number of fibres broken if one assumes a uniform dispersion of fibres in the matrix. Thus figure 5.9 shows that the cross section area damaged is a linear function of N_{100} , leading to the preliminary conclusion that the number of fibres broken is proportional to N_{100} . A linear regression line for sample A in figure 5.9 yields the following relation:

$$N_{100} = 62.02A_d - 322 \quad (5.2)$$

If the emissions above a certain energy level are proportional to the number of fibres broken then the constant term in Eq. (5.2) should be zero. Apparently the choice of 100 as the energy below which to discard events was too high. Had it been lower there would have been more events at the low values of area damaged in figure 5.9 and the straight line would have gone through the origin. However Eq. (5.2) adequately describes the relation between area damaged and number of AE events.

To further substantiate the relation between N_{100} and cross section area damaged the relations developed in chapter 3 may be used. For the samples in question, rods A, B and C, area damaged as a function of normalized compliance is plotted in figure 5.10. This is done by calculating C_0/C from Eq. (3.18) and (3.25) and A_d from Eq. (5.1) for given values of d . A_d values computed for rods A, B and C from Eq. (5.2) and the measured compliance value corresponding to N_{100} are also plotted in figure 5.10. These points fall on the theoretical curve representing the relation between A_d and C_0/C . Since the relation between A_d and C_0/C and between N_{100} and A_d are linear it is expected that the relation between N_{100} and C_0/C should also be linear. Figure 5.11 shows that this is the case for all three samples.

Two conclusions can be made from this. One, N_{100} is almost certainly proportional to the number of fibres broken. This has been shown in terms of area damaged and compliance increase. Two, although the 100 in N_{100} may be too high a value (the intercept in Eq. (5.2) is not zero), the compliance and area can still be measured provided one sample (here sample A) is used to correlate A_d versus N_{100} .

5.4 Damage Length

Source location of AE events can be done in one or two dimensions with the PAC equipment using two or four sensors. Planar location over large areas is possible using several sensors and more complex equipment [56]. In one dimension (the longitudinal axis in the samples tested) location is straightforward.

It has been shown that the crack length grows to approximately 400 mm a few thousand cycles after initiation. Since AE events may be generated all along this length, accurate source location may be used to determine the crack length at intervals during the test. Events, from whatever mechanism, will be recorded from points between each crack

tip and also at each crack tip. If the emissions from each crack tip can be located, the distance between them will be the damage length. However, for reasons to be discussed below, a number of factors cause events to be located erroneously. In particular events can be located outside the damage zone. Therefore it is necessary to discriminate between events detected as being inside the damage length and those detected as being outside the damage length.

Referring to figure 5.12 it is desired to determine the distance vt where v is the wave velocity and t is the time taken by the wave to reach the first-hit sensor. This is the distance from the source to the channel hit first by the event. When the first channel is hit a timing circuit within the monitoring equipment is triggered. When the signal from the same event hits the far sensor the timing circuit closes and a time Δt is measured. Since the wave is assumed to travel at the same speed in opposite directions, Δt is the time taken for the wave to travel a distance $l-2vt$ (figure 5.12). Thus

$$vt = \frac{l}{T} \left(\frac{T - \Delta t}{2} \right) \quad (5.4)$$

The AE equipment used for these experiments records a Δt value for each event. At the start of the test a value for T is obtained from a calibration using a third sensor as a pulser to send a wave from one sensor to the other. This value depends on the wave speed of the material under investigation. In these tests the value is typically 150 μs over 600 mm.

Rod G was selected for location analysis. Two sensors were positioned on the ends of the rod, one with the face perpendicular to the longitudinal axis, the other with the face parallel to the longitudinal axis. This had to be done to accommodate the pulser whose

face was perpendicular to the longitudinal axis, figure 5.13. During the test location was monitored by an events versus location histogram. This is a record of the number of events, regardless of characteristics, generated along the rod axis. Approximately every one hundred cycles the histogram was stored and the system reset to record events from the next one hundred cycles. If the histogram was not reset at these intervals the large number of events recorded after several thousand cycles would have obscured information obtained at the start of the test.

Figure 5.14 is an events versus location histogram for the interval $2600 < N < 2700$ for sample G. A total of 2321 events were generated during this interval. Some events were located along almost the entire length of the specimen (600 mm) even though the damage length at the end of the interval was 214 mm. There appears to be three distinct peaks in the histogram. The outside two peaks may correspond to the two crack fronts. The centre peak may correspond to the central load point where events were generated from fibre breakage and friction. To establish that the two outside peaks do locate the crack front a one to one correlation between the peak to peak distance and visually measured damage length must be made for several of these intervals. In this particular histogram the two peaks stand out. In other cases the peaks may not be so obvious and therefore the resolution of the peaks must be improved.

To improve the resolution of the peaks, and to ultimately determine the proper width over which to measure the distance between crack fronts, it is assumed that events from the crack fronts can be distinguished from those outside the damage zone. The data for each of the 2321 events was printed out. This includes, for each channel, the Δt value, the channel first hit and the event duration, counts, energy, amplitude and rise time. From the good agreement between the peak to peak width (223 mm) and actual damage length (214 mm)

in figure 5.14 it is assumed that the peaks correspond to the two crack fronts. From the initial timing value T (104 μ s) the Δt values for each peak were determined from Eq. (5.4). From the print out of all events, events at the two peaks were isolated. This was done by noting that the left peak had Δt values of 30 μ s and the right peak had Δt values of 55 μ s (the sensors were located unsymmetrically about the damage zone, figure 5.13, accounting for the difference in Δt times). Of 2321 events 71 were located at the left peak and 57 were located at the right peak. Each of these events were scrutinized to determine what they had in common in terms of the event parameters. The results are summarized in table 5.2.

Table 5.2 Event Parameters at Crack Fronts.

Event Parameter	Channel Closest to peak	Channel farthest from peak
Duration	54-237	>0
Energy	4-50	>0
Counts	-	>0
Amplitude	68-78	64-71

All the data were filtered by excluding all events that did not meet the first three of the above four criteria (the majority of events fell within the amplitude range). The resulting histogram is plotted in figure 5.15. As was hoped for, only the events at the two peaks remain. This has sharpened the peaks making a width measurement much less subjective. The same process, using the criteria of table 5.2, was used on five other intervals, figure 5.16. The width of the histograms increased with increasing cycles indicating damage growth in the length direction. The width is taken as the maximum extent of the histograms. The exact length of damage, however, is consistently overestimated, figure 5.17.

AE source location was performed for laminate L with the transducers attached to the ends. A notable increase in signal travel time was observed as the damage progressed beyond 60 mm in length and 3 mm in depth. Since source location depends on signal travel time, location accuracy will suffer at this stage. Laminate L was tested by sawing a series of progressively deeper notches on the tension side beneath the central load point. Each time the notch was deepened fifty cycles were applied and AE recorded. At the end of fifty cycles the damage length was measured. Here all emissions must have been from damage growth in the length direction or friction between damage surfaces and not from growth in the depth direction. Growth in the depth direction was simulated by the saw notch with the AE equipment turned off. Once the AE was recorded the data was filtered according to the criteria established in table 5.2. The results for five successive histograms are shown in figure 5.18. As with the rods the width of the histograms spreads out with increasing cycles, indicating damage growth in the length direction. The length in this case is also consistently overestimated, as would be expected from the increase in signal travel time, especially after a depth of 2 mm. For this sample a depth of 2 mm corresponds to a length of only 50 mm. In figure 5.19 the relation between visually measured length and source location shows that source location consistently overestimates the damage length, even at 50 mm, and more so at longer lengths.

In the literature two reasons can be found for the inaccuracy of source location. The first is attenuation, the second is an increase in travel time due to an altered signal path through damaged areas. Workers using planar location schemes on aerospace structures

discovered large differences in wave velocity and high attenuation in certain directions [55,56]. Depending on the underlying wing structure and material direction attenuation ranged from 1.1 to 2.9 dB/cm and wave velocities were measured at 500 to 730 cm/s. According to Hamstad [47] the accuracy of source location by first penetration of the threshold suffers from attenuation of the first half-cycle of the AE wave before it hits the farthest sensor. This means that the wave actually travels at the same speed, but because the first few cycles are reduced in amplitude they do not penetrate the threshold. This causes the timing circuit to be open longer than it should be. If the timing circuit is open too long the Δt time will also be too long. This results in an apparent increase in travel time. That is, the wave speed is unchanged, but because of the way it is measured it appears to have increased. Thus it appears that attenuation and a reduction in wave speed are related. In a one dimensional structure (i.e. a beam) an apparent increase in travel time has the effect of locating the source nearer to the nearest sensor than it actually is. Referring once again to figure 5.13, an emission leaving point A reaches sensor 1 in time t . The same wave reaches sensor 2 in time $t + \Delta t$. Because this wave must travel a greater distance and through a damaged area it is subject to some attenuation. If the first few half cycles of the wave are attenuated the time $t + \Delta t$ will be overestimated. From Eq. 5.2 the source will be located closer to sensor 1 than it actually is. The same occurs for emissions coming from the opposite end of the sample. Assuming that attenuation increases with increasing distance travelled and increasing damage zone size, location accuracy will get worse as the damage zone size increases. Since attenuation causes the sources to be located nearer to the nearest sensor than they actually are, the damage length will be overestimated. Since attenuation increases with damage zone size, the magnitude of the overestimate will increase as

damage length increases. This is consistent with the results for rod G and laminate L, figures 5.17 and 5.19 where the damage length is consistently overestimated, and increasingly so as damage length increases.

Mitchell and Miller [51] have proposed that an AE wave will take a different path through undamaged and damaged material. The path length will be longer through a damaged material as the wave scatters and reflects off several material boundaries. They show significant increases in travel time for simulated acoustic emissions travelling through undamaged and impacted areas of CFRP cylinders. They also observe significant reductions in amplitude for the same emissions travelling through the same impacted areas, but do not make the connection between attenuation and increase in travel time. Their results do show, however, that travel time increases as damage severity increases.

For whichever reason, attenuation or a longer wave path, it appears that a measured increase in travel time by an acoustic emission leaving a crack front causes the damage length to be overestimated.

5.5 Damage Depth

It has been shown by Mitchell and Miller [51] that attenuation can give a measure, and perhaps a quantitative one, of the damage state of the material. A series of simulated AE events are pulsed through the sample by attaching a third, active, transducer to the specimen and forcing an acoustic wave from one end of the sample to the other. By placing this "pulser" at one end of the sample and pulsing a signal past the damage zone to a sensor, any change in magnitude of the waveform parameters from their initial values may give some indication of the damage state.

Previous work using a pulser and a single transducer on type II rods [23] has shown that AE energy transmitted decreases as damage grows, figure 5.19. Plotted is the average energy measured by the receiver normalized by the energy measured in the undamaged state as a function of damage depth. In this manner, the normal losses associated with signal propagation through the length of the rod remain constant, at least to a first approximation. There is little attenuation in the transmitted energy until about 2400 cycles. As damage is visible at 1400 cycles, attenuation of the signal appears to be insensitive to small amounts of damage.

Important considerations are the positioning of the pulser and transducers, the AE threshold and the waveform parameters to be monitored. Tests on rods D through I and laminate L were performed to investigate the attenuation of amplitude, energy, duration, counts, rise-time and increase in travel time at three different thresholds and three transducer orientations.

Figure 5.20 shows results for rod D. Plotted is the increase in travel time and decrease in amplitude, duration and energy as a function of compliance. Rod D shows a high degree of scatter in all AE values at very small changes in compliance. Since this sample sustained very little damage the changes in all four parameters must be attributed to measurement. This may be due either to the threshold (60 dB) or transducer position (compression surface).

The following sample, rod E in figure 5.21, was tested with the same transducer orientation but a lower threshold (51 dB). The scatter is still present. The travel time is seen to remain constant while amplitude, duration and energy are reduced with energy showing the greatest change at the maximum compliance values.

Rod F, figure 5.22, was tested at the same threshold (51 dB) but with a different transducer orientation. Here the transducers were placed on the tension side. This eliminated some of the scatter in the data for all except the energy values. Even with the reduced scatter, however, there is little change in any of the values from their initial value to indicate a change in amount of damage.

The test on rod G, figure 5.23, was carried out with a threshold of 71 dB and the transducers on the ends. The travel time remained constant for a compliance increase of 1.4 times the original value. The amplitude showed a slight drop to slightly more than 80% of its original value, with very little scatter. Similarly the duration decreased, with some scatter, to approximately 40% of its original value. Thus reduction in duration in this case is twice as sensitive to changes in compliance as reduction in amplitude. The most sensitive measurement was the decrease in energy transmitted. This decreased to nearly 20% of its original value with very little scatter.

Rod H (type II), figure 5.24, shows similar behavior, except that there is a travel time increase near the end of the test. This was not observed for rod G (type III). Similar to rod G the amplitude decreased only slightly at a compliance increase of 1.6 times its original value. The duration and energy are again more sensitive than the amplitude, with energy showing the greatest sensitivity to a change in compliance.

Rod I, figure 5.25, although at a higher load ratio, showed nearly identical behaviour to rod H for increase in travel time and reduction in amplitude. The reduction in duration and energy transmitted are also nearly the same, but with some scatter.

From these figures it appears that positioning the pulser and receiving transducer on the ends of the sample affords the best indication of change in compliance of the three

orientations tested. It is also evident that energy is the parameter most affected by damage growth. It is unclear whether damage depth, length or some combination of the two account for the attenuation. For rods F and G the attenuation of energy is plotted as a function of length in figure 5.26 and depth in figure 5.27. Rod F, with the transducers on the tension side, is relatively insensitive to damage length or depth. For rod G, with the transducers on the ends, there is attenuation with respect to both length and depth. Attenuation is more sensitive to the depth dimension as can be seen from the figures. Although length and depth are inseparable, it appears that a correlation with depth is more useful.

Laminate L was tested with the transducers on the ends. This sample was tested by cutting a notch with a hack saw to create artificial damage in the depth direction. Every 50 cycles the notch was deepened. Before and after the notch was deepened attenuation measurements were made. After the notch was deepened cycling was resumed and the damage grew to a new length at the new depth. This way the effect of notch depth was separated from damage length. Figure 5.28 shows the results for travel time, amplitude, duration and energy. A vertical line represents a change in the AE parameter being measured with no change in depth. A horizontal line represents a change in depth with no change in AE parameter. For the last two depths the travel time increases only after the damage has grown to a new length at the new depth. When the notch has been cut to a new depth (with the width of the saw blade) the travel time does not increase. This indicates that attenuation is sensitive to volume of damage and not just depth. The other three parameters show similar behavior. Each depth increase does not affect the AE parameter. Each volume increase (product of length and depth at constant width) attenuates the parameter significantly, especially duration and energy.

Since the increase in travel time is accompanied by attenuation of the amplitude, and since the depth alone does not result in a travel time increase, these results seem to support Hamstad's idea and not Mitchell and Miller's. Mitchell and Miller [51] claim that propagating waves will reflect off material boundaries and take a longer path to the sensor. Therefore their travel time is longer. If this is true, a travel time increase should have been detected after the depth was increased and before the length was increased. Hamstad, however, claims that an increased travel time is due to attenuation of the amplitude of the first half cycle. If the first half cycle is reduced to an amplitude below the threshold value, the next half cycle will trigger the timing circuit causing an increase in travel time. Here the peak amplitude has been reduced as well as the duration. The reduction in duration of the repeatable source signal indicates that part of the signal, the leading and trailing cycles, have been attenuated below the threshold value, accounting for the shorter duration. If the leading cycles of the event were attenuated below the threshold then the travel time would have increased, as observed.

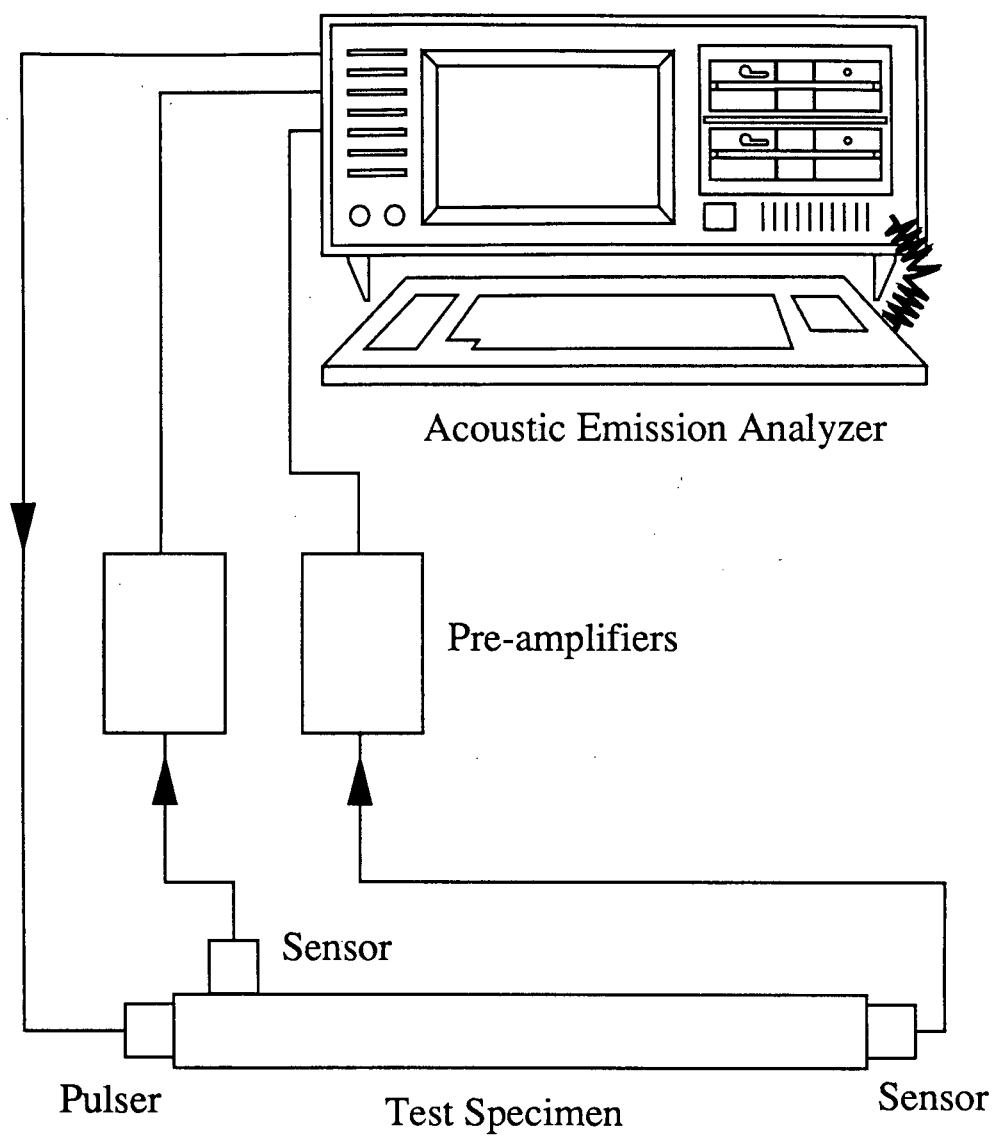


Figure 5.1 Acoustic emission monitoring.

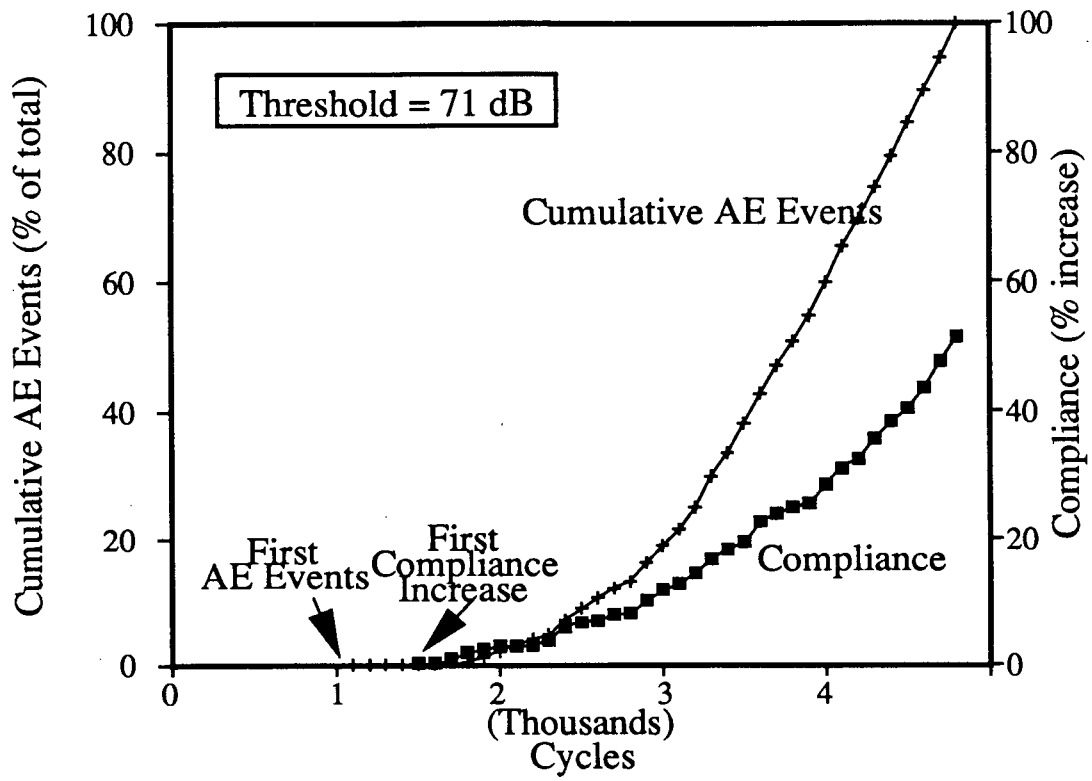


Figure 5.2

Damage initiation, rod A.

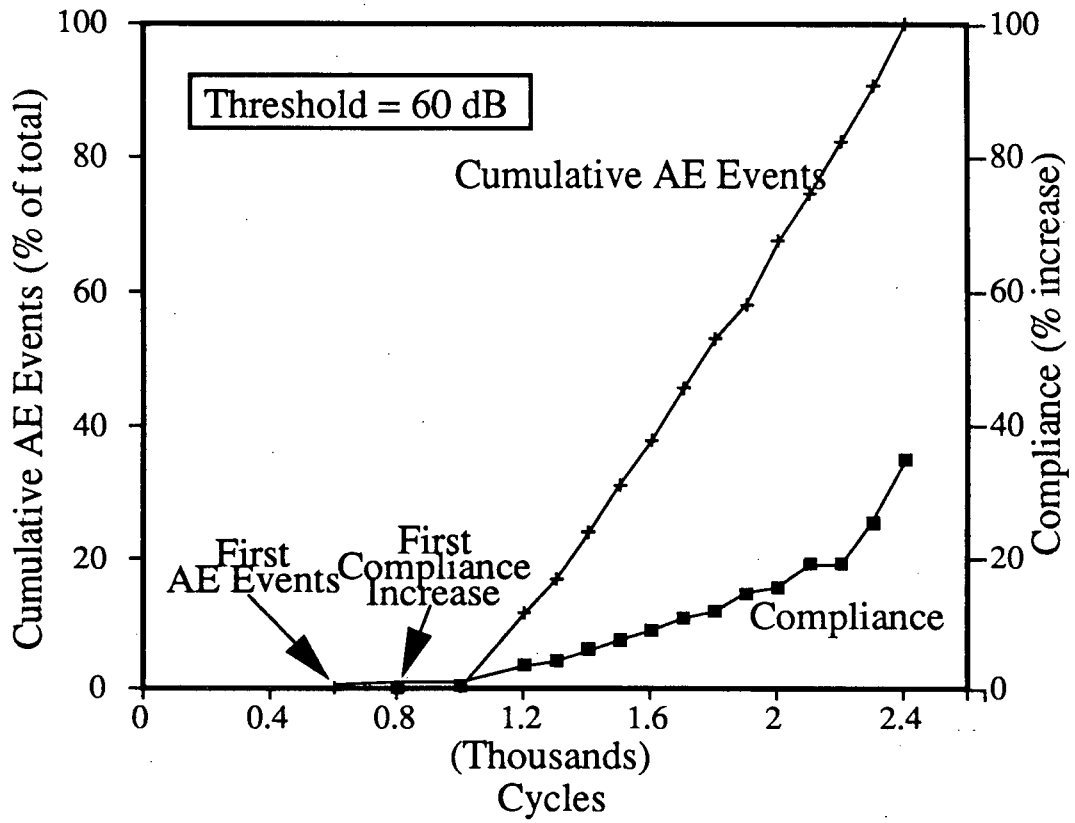


Figure 5.3

Damage initiation, rod I.

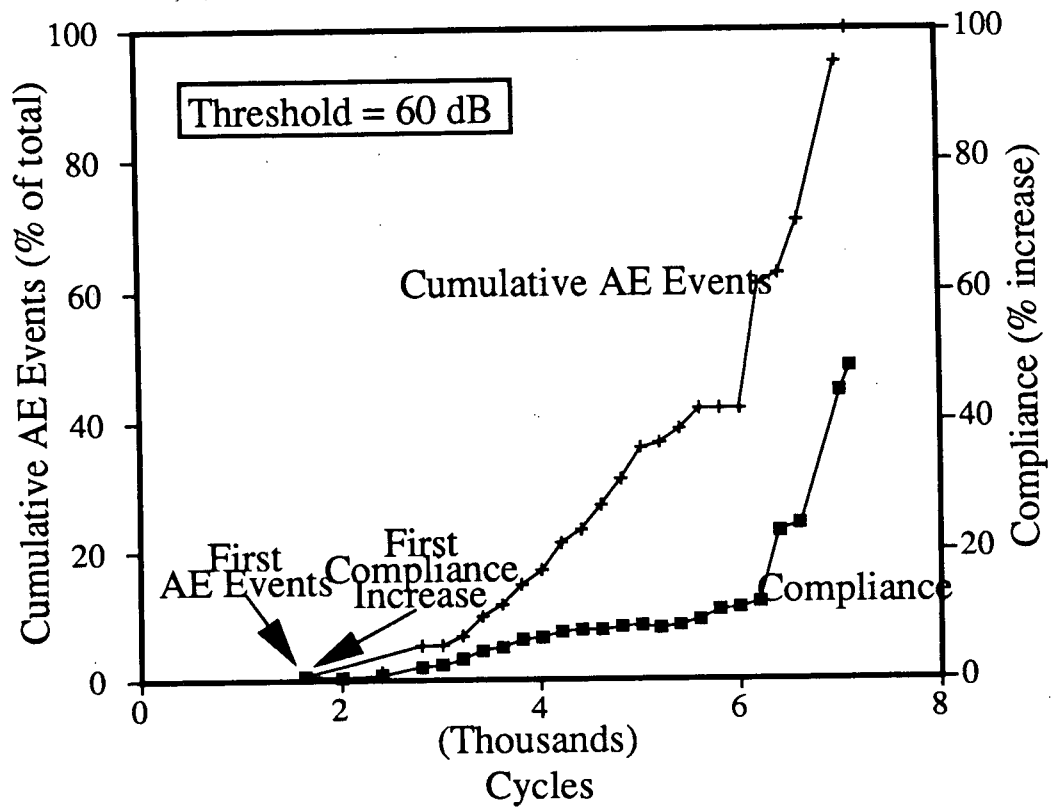


Figure 5.4 Damage initiation, rod E.

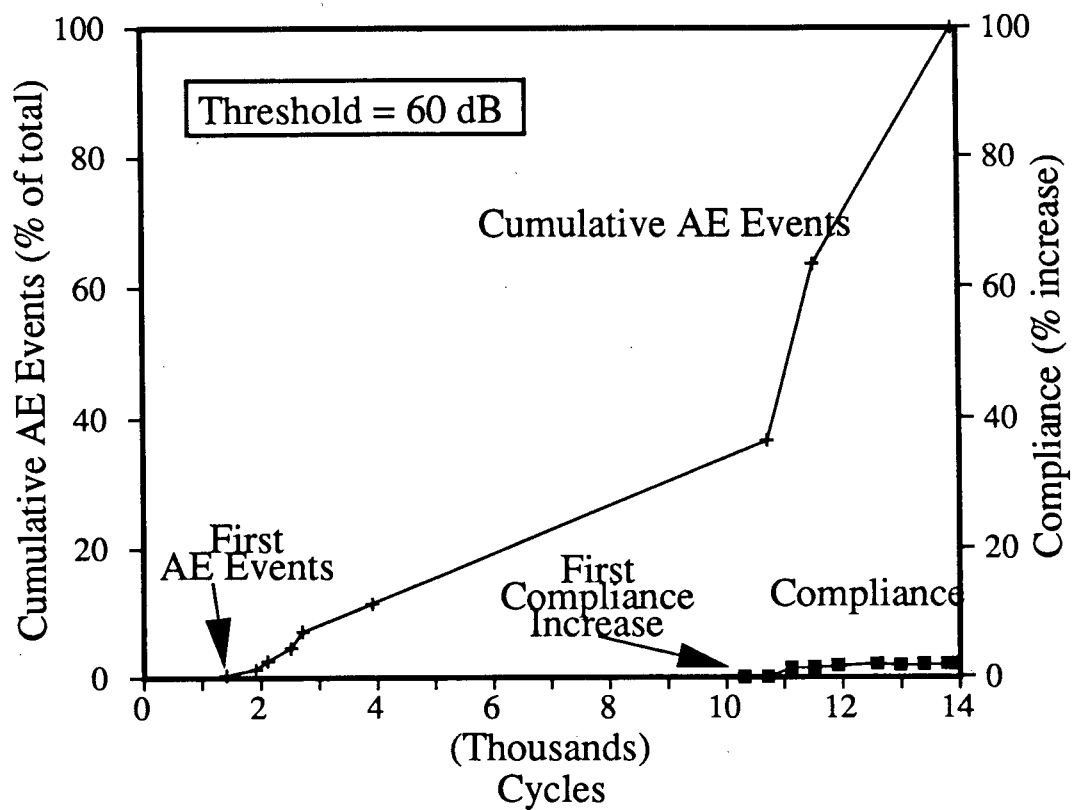


Figure 5.5 Damage initiation, laminate J.

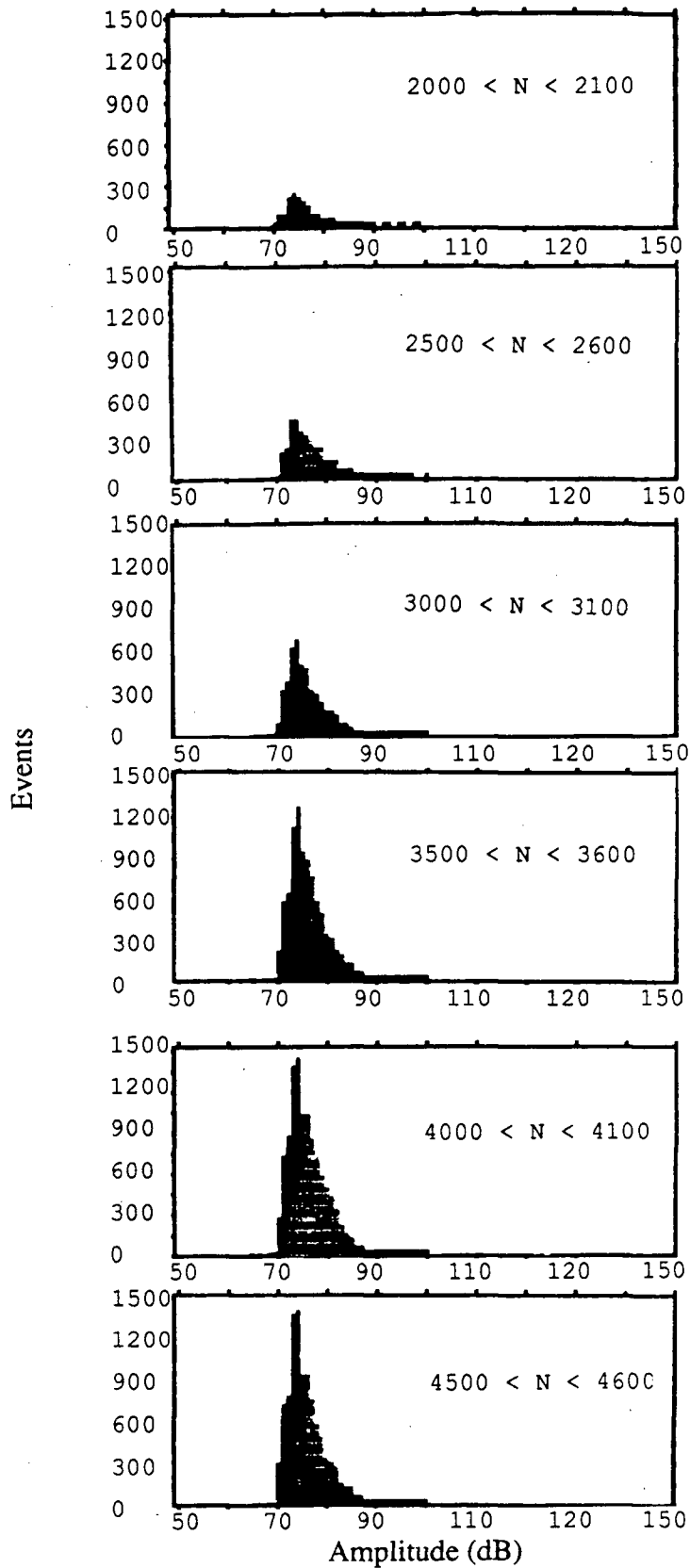


Figure 5.6

Amplitude distribution histograms for rod A for increasing cycles.

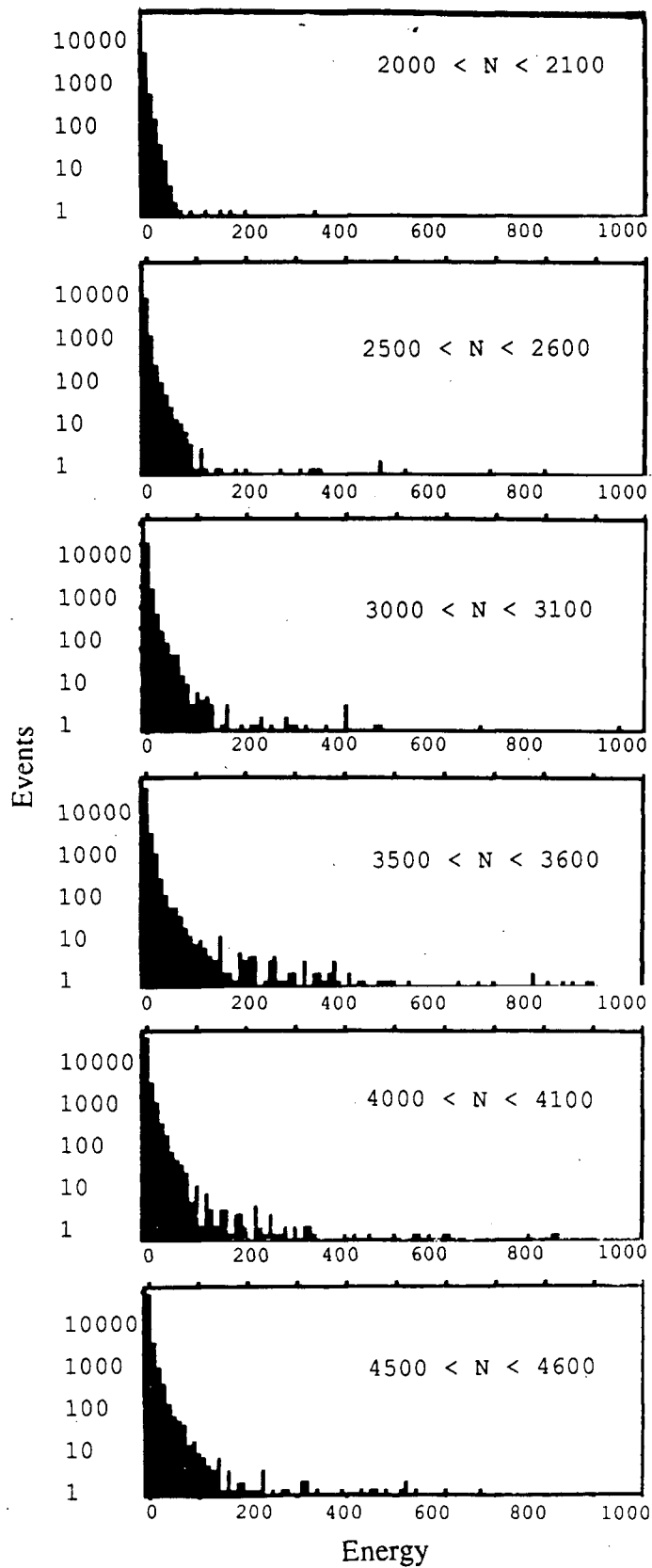


Figure 5.7

Energy distribution histograms for rod A for increasing cycles.

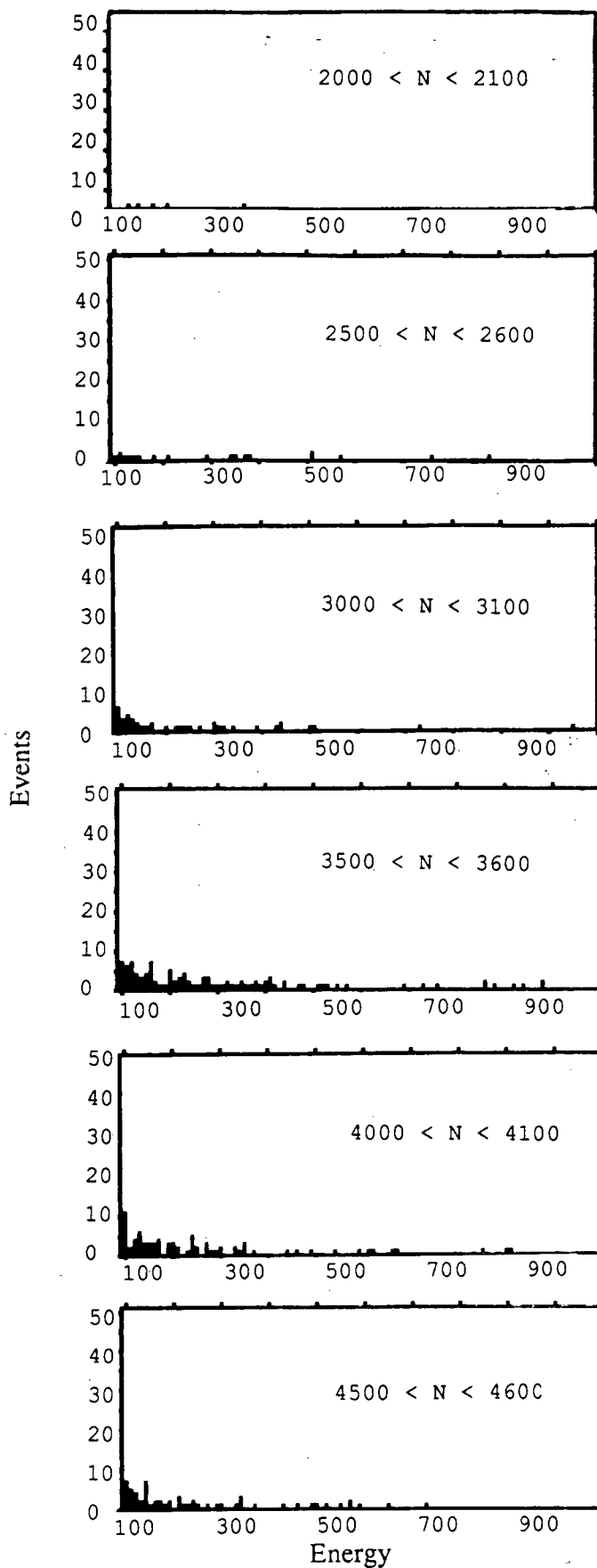


Figure 5.8 N_{100} (Energy > 100) distribution histogram for rod A for increasing cycles.

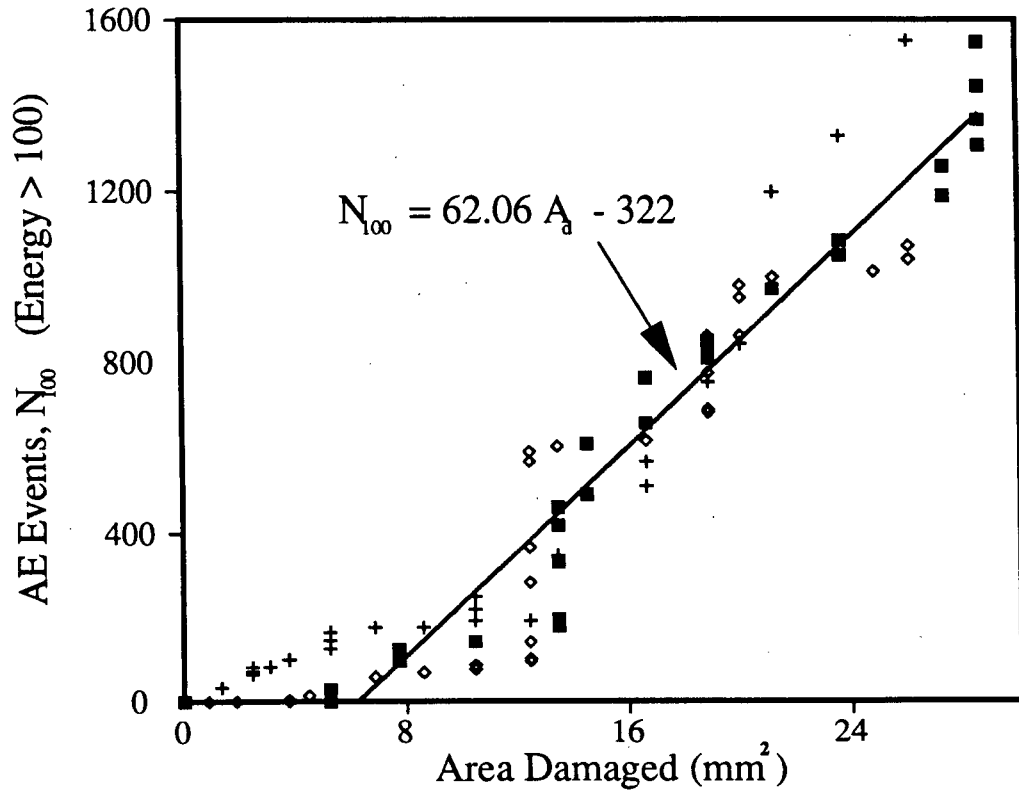


Figure 5.9

Cumulative AE events with energy greater than 100 (N_{100}) as a function of damaged cross sectional area, rods A, B and C.

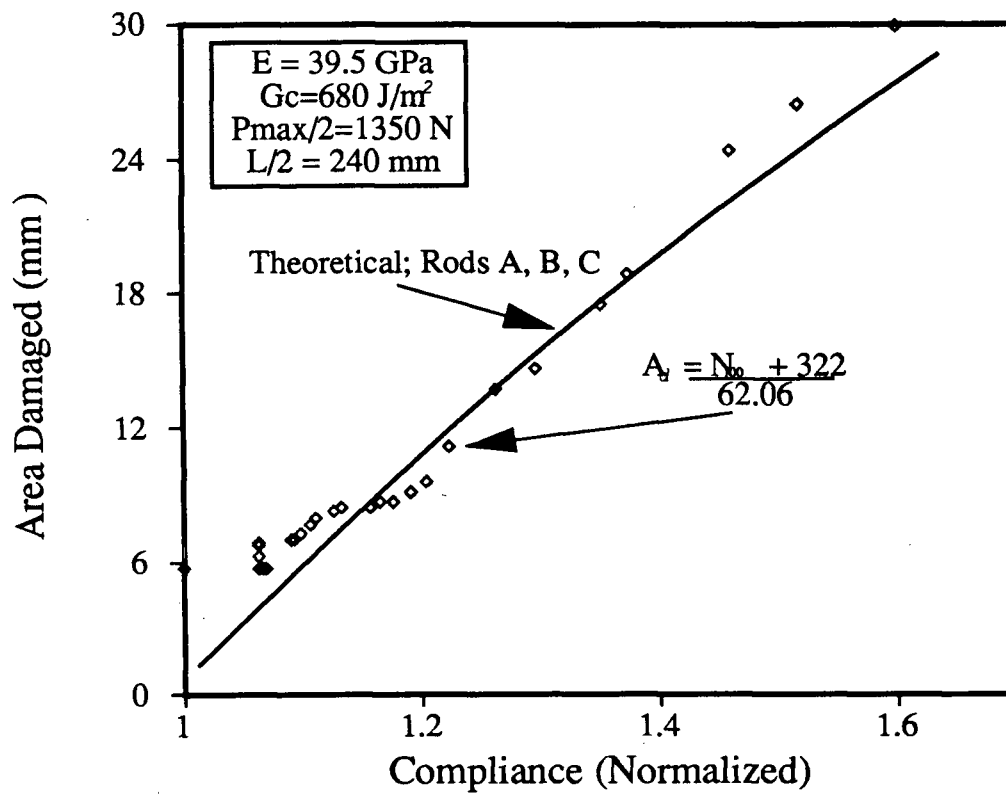


Figure 5.10

Cross sectional area damaged as a function of compliance for rods A, B and C from theory (chapter 3) and experiment (A_d predicted from N_{100}).

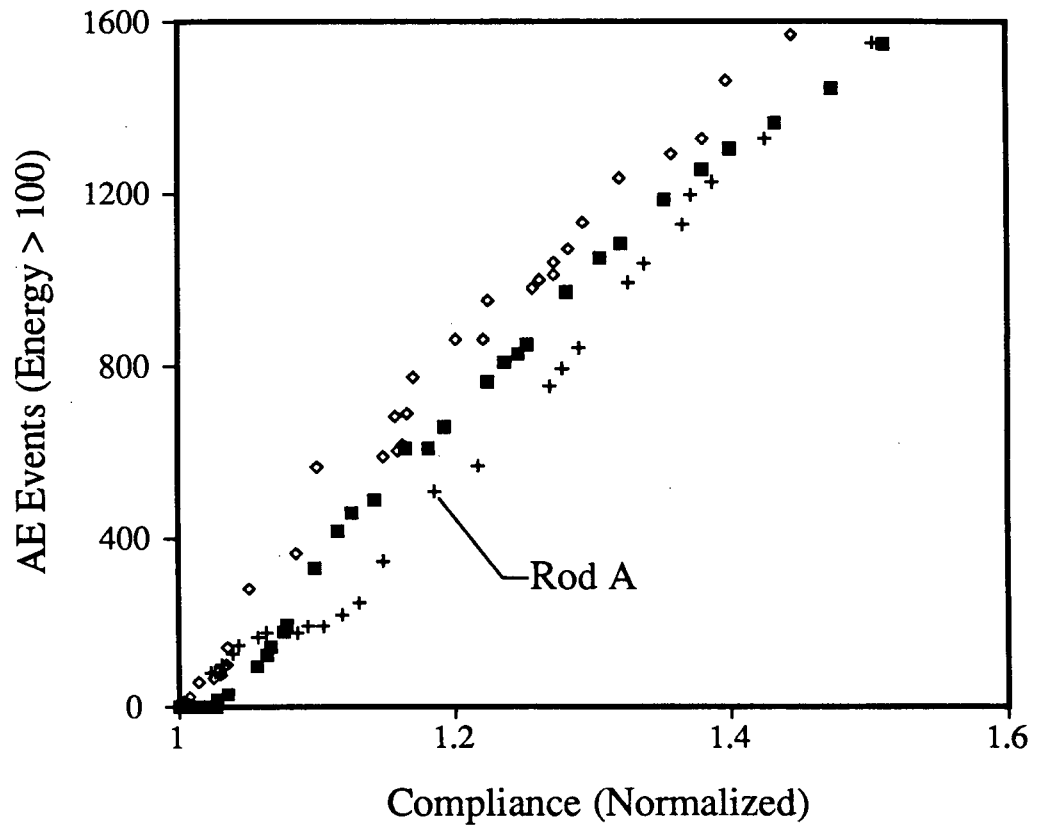


Figure 5.11 AE events as a function of normalized compliance, rods A, B and C.

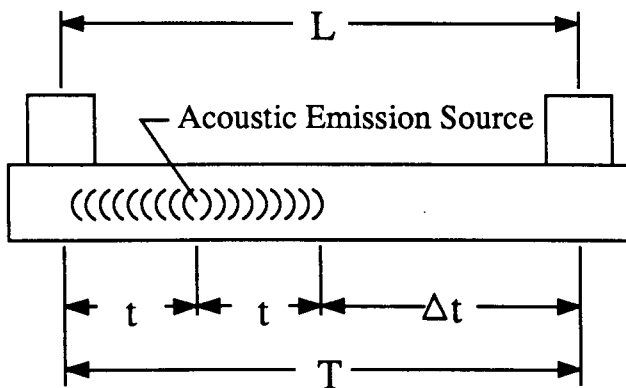


Figure 5.12 One dimensional AE source location.

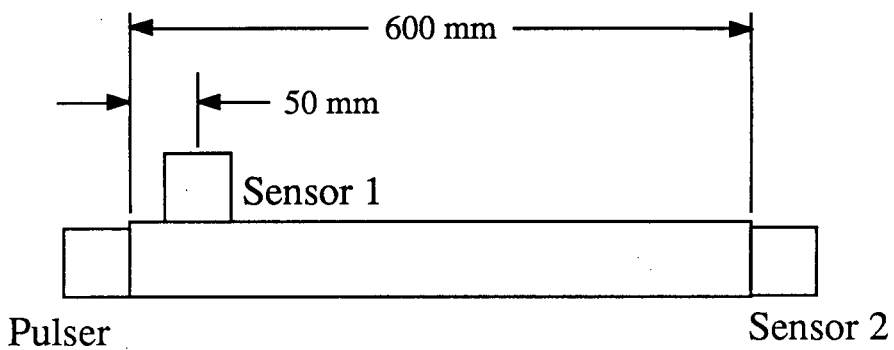


Figure 5.13 Transducer positioning.

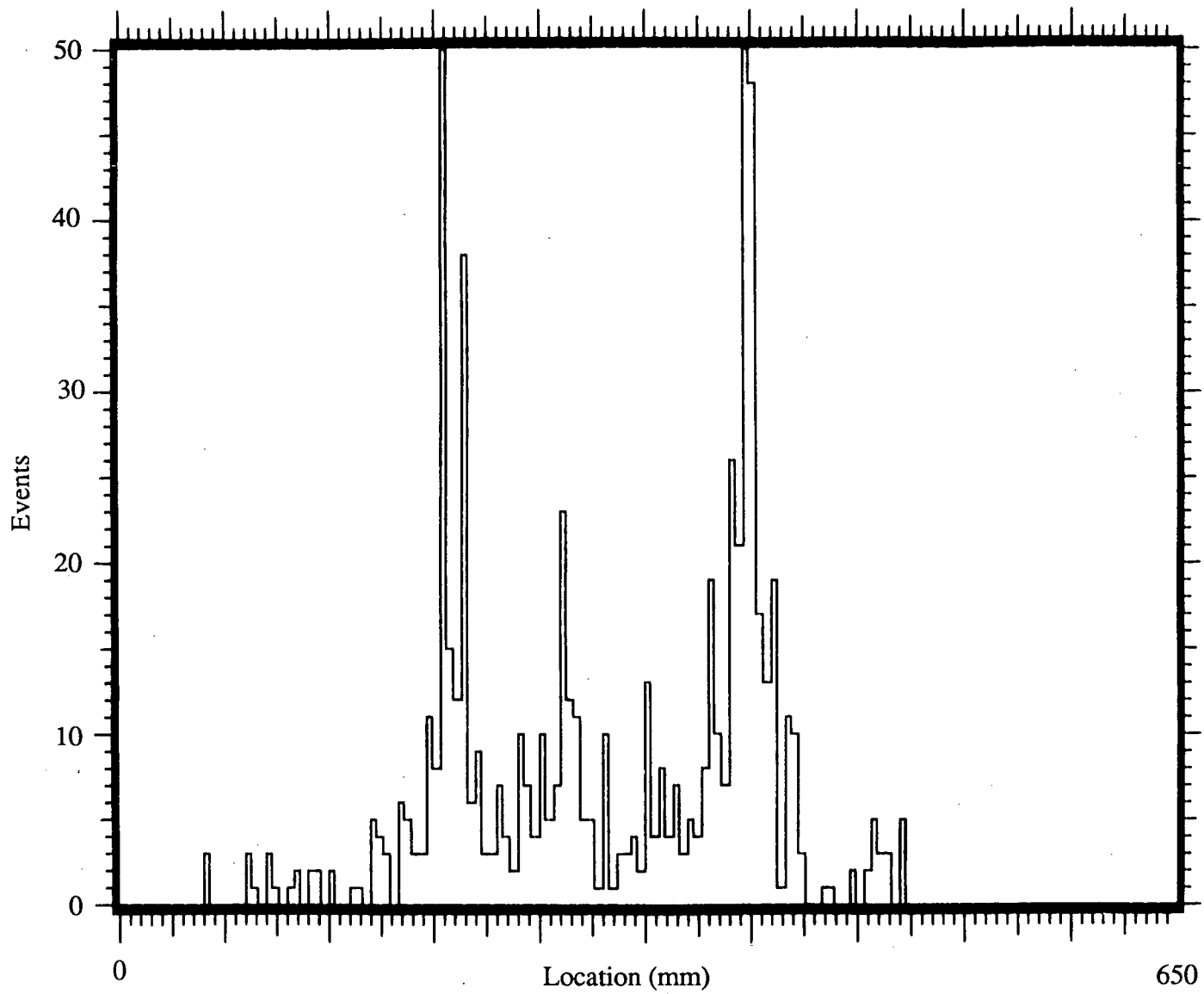


Figure 5.14

Location histogram between 2600 and 2700 cycles, rod G.

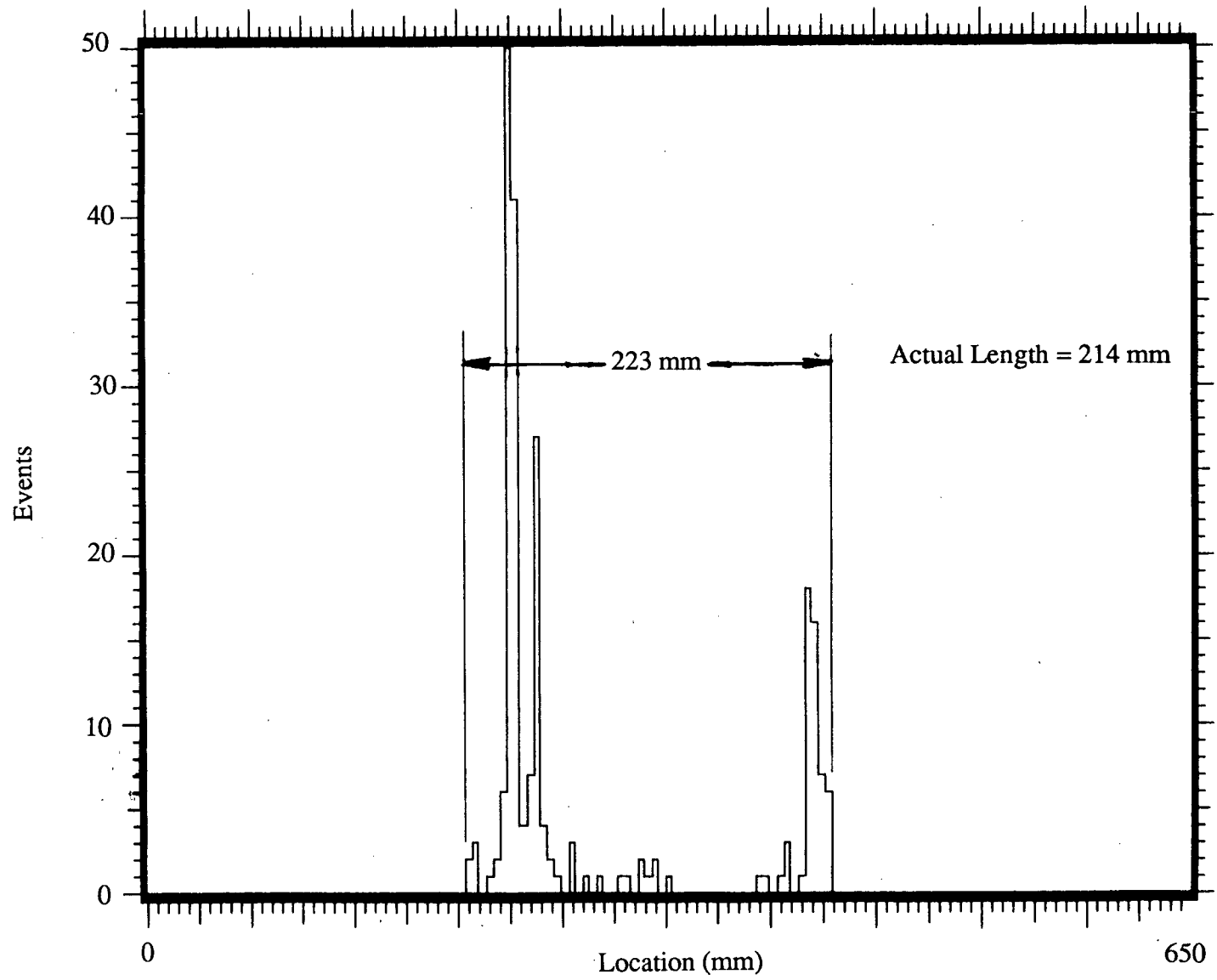


Figure 5.15 Location histogram between 2600 and 2700 cycles with events outside of values in table 5.2 removed, rod G.

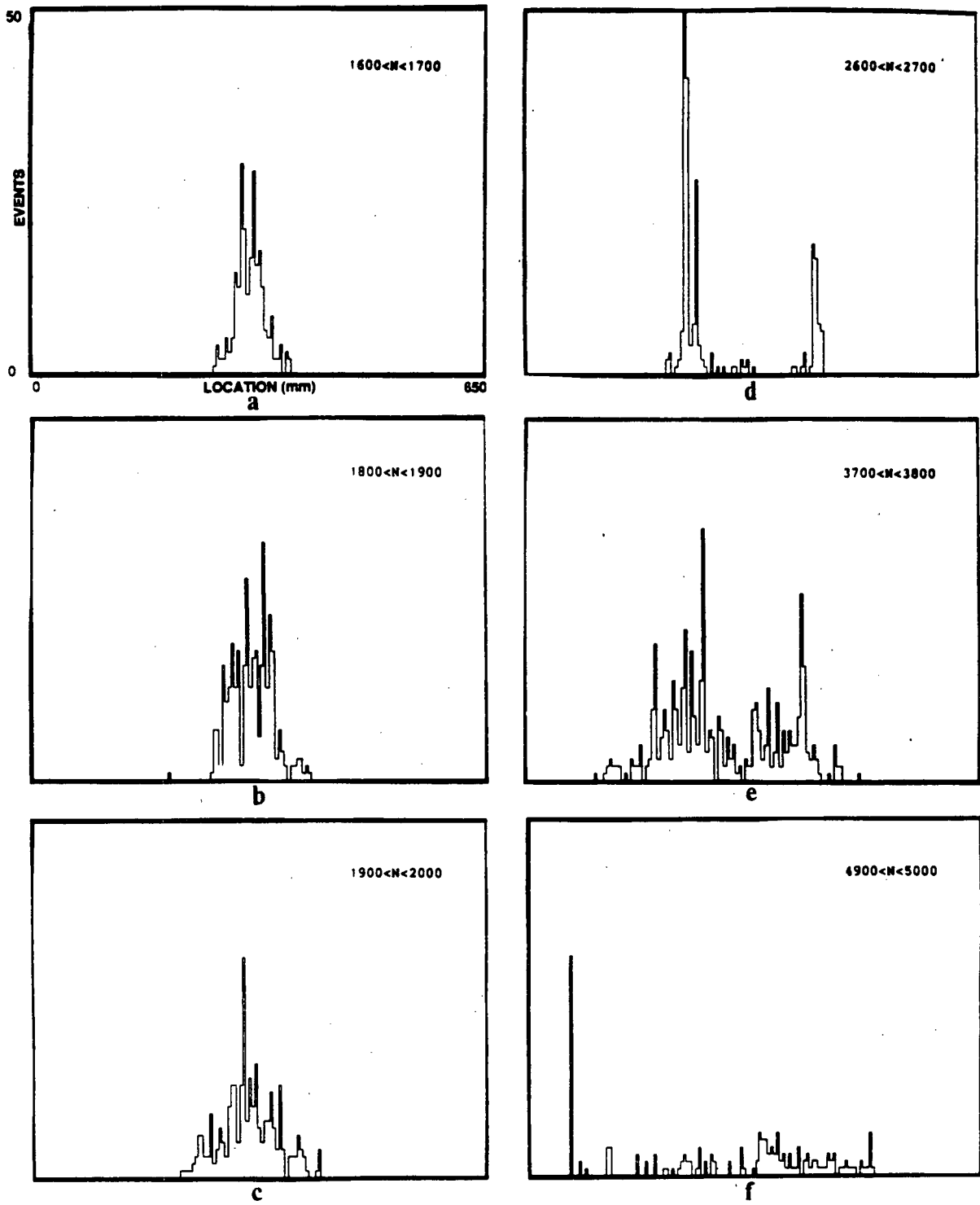


Figure 5.16 Series of location histograms for rod G. Width of histograms increases with increasing cycles indicating damage growth in length direction.

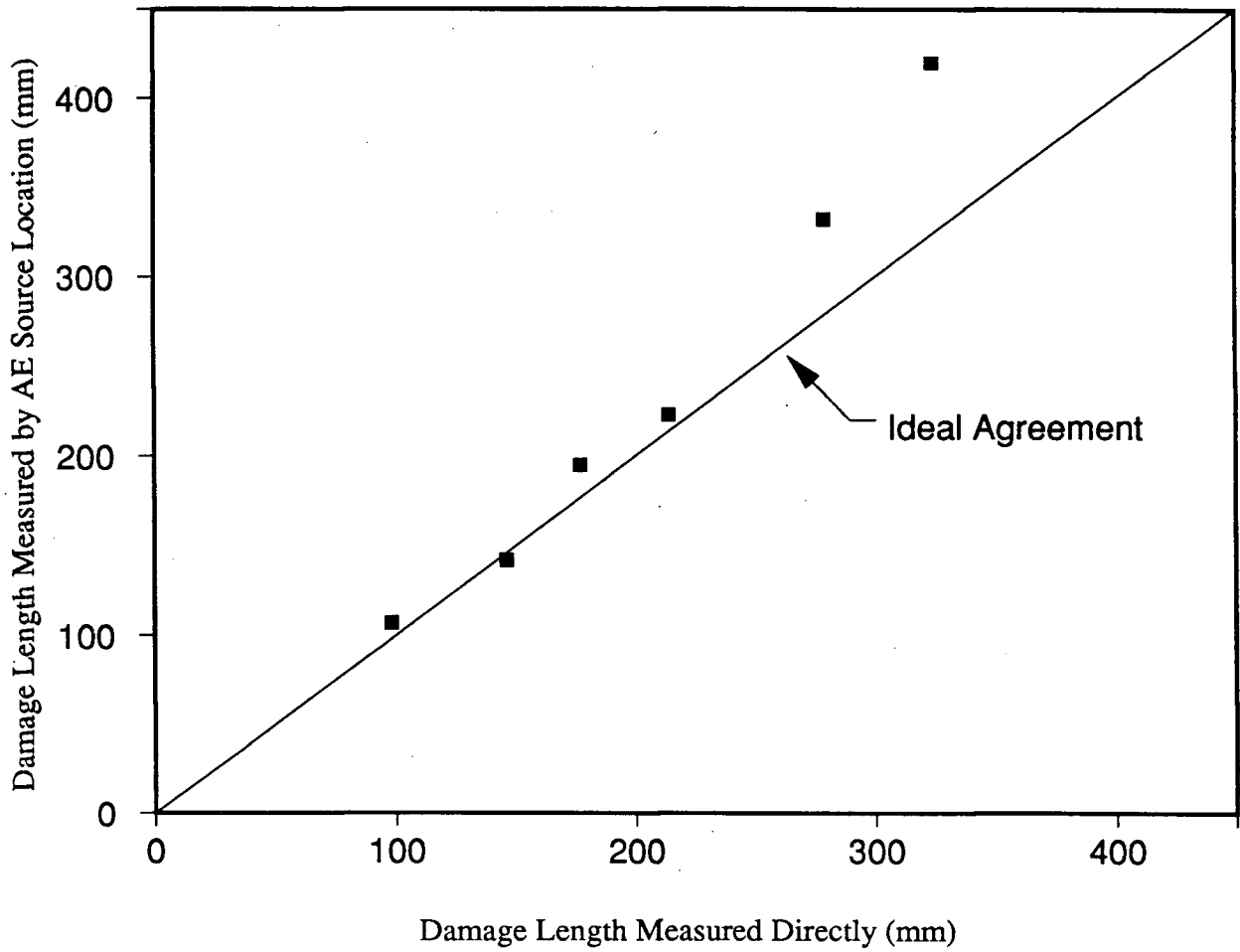


Figure 5.17

Damage length measured by source location as a function of actual damage length, rod G.

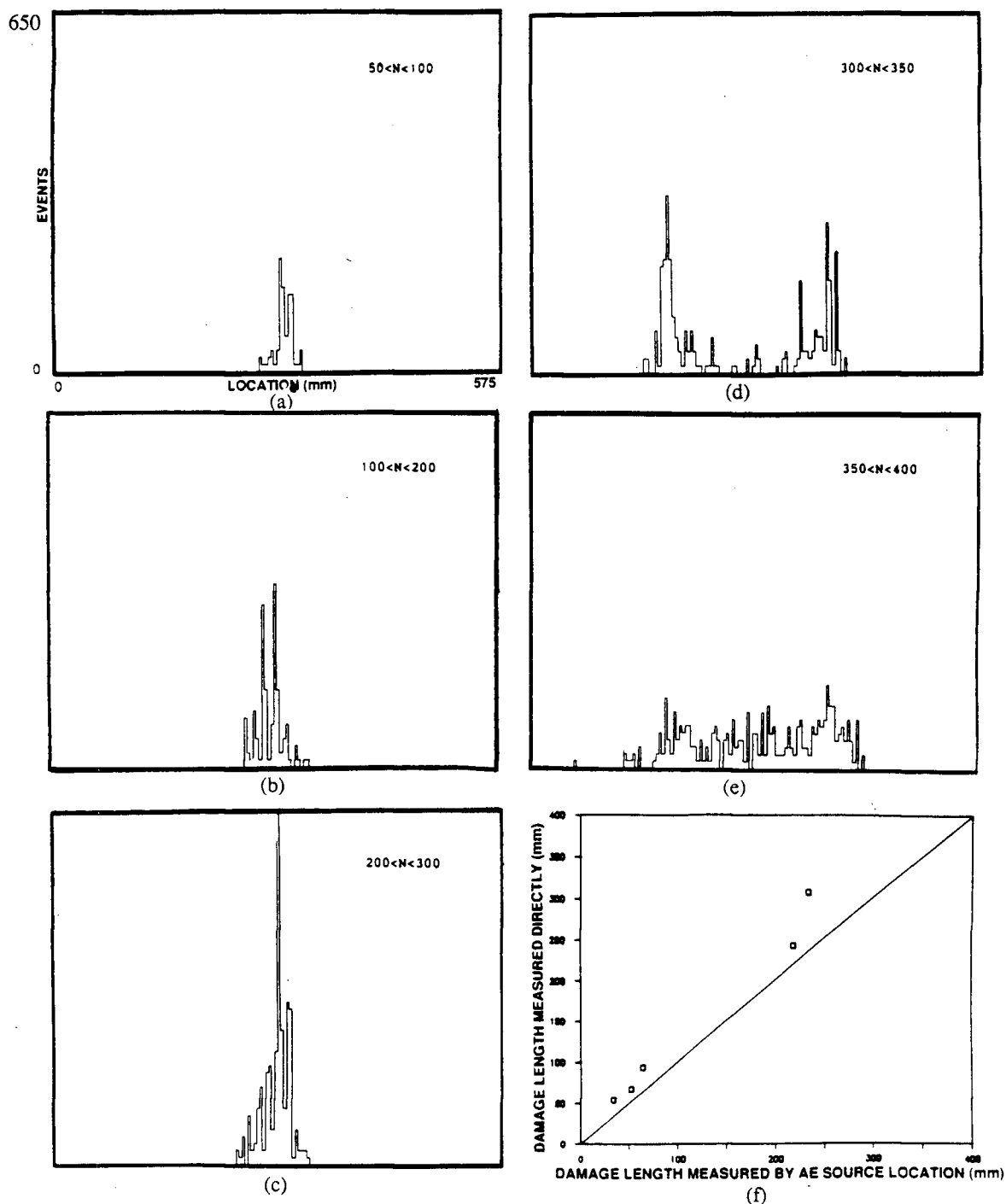


Figure 5.18

(a-e) Series of location histograms for laminate L. Width of histograms increases with increasing cycles indicating damage growth in length direction. (f) Damage length measured by AE source location as a function of actual damage length, laminate L.

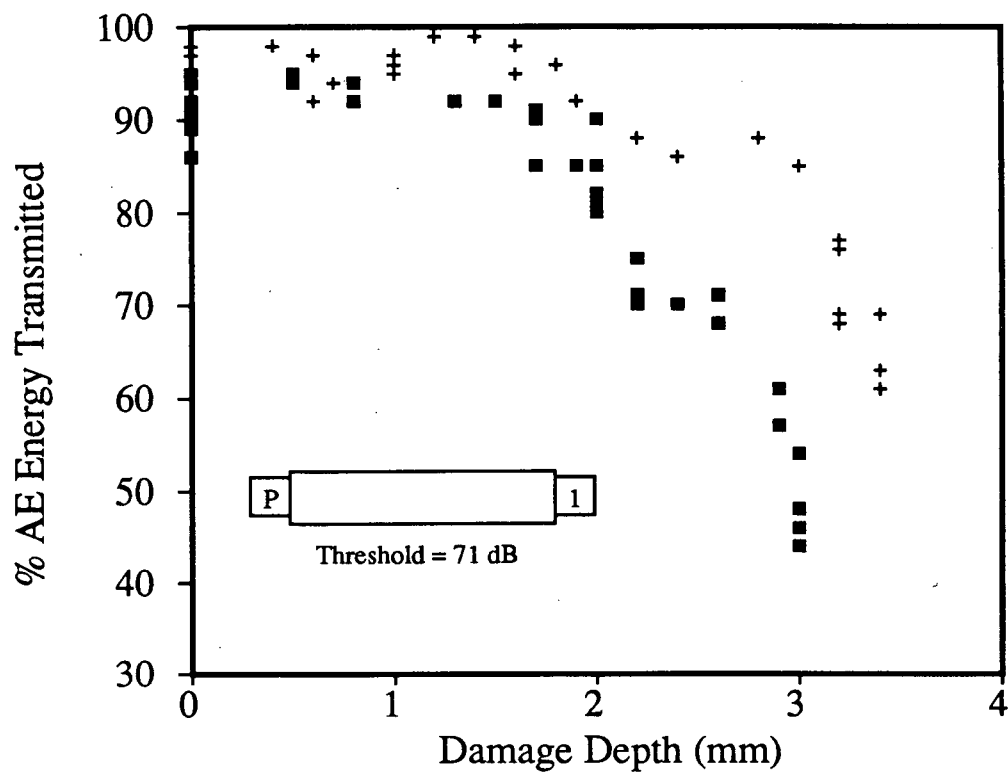


Figure 5.19

Attenuation of energy transmitted by pulser as a function of damage depth, rods A and B.

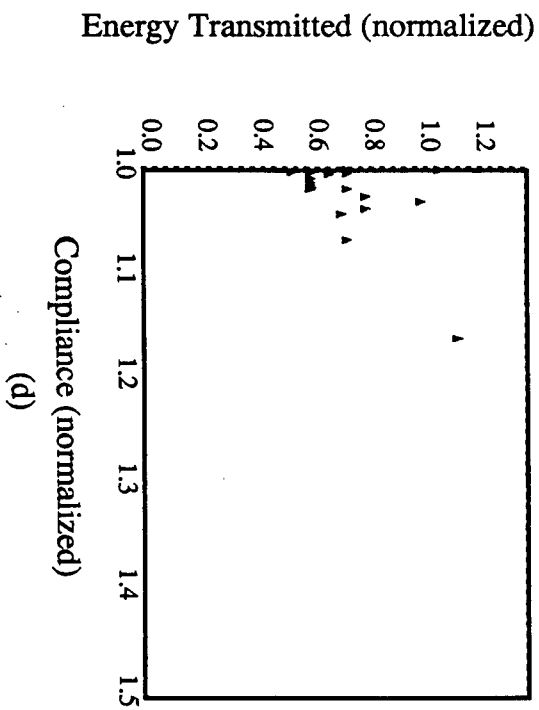
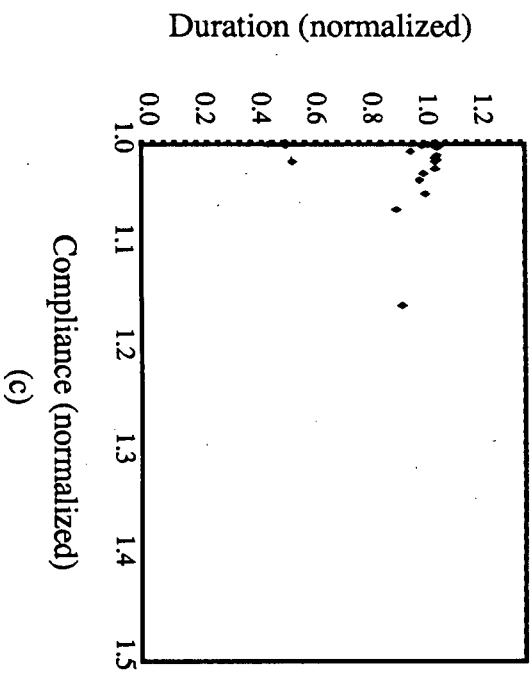
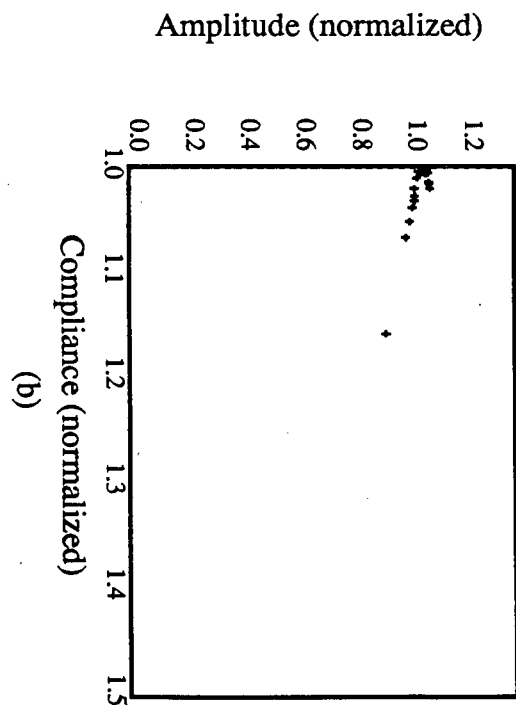
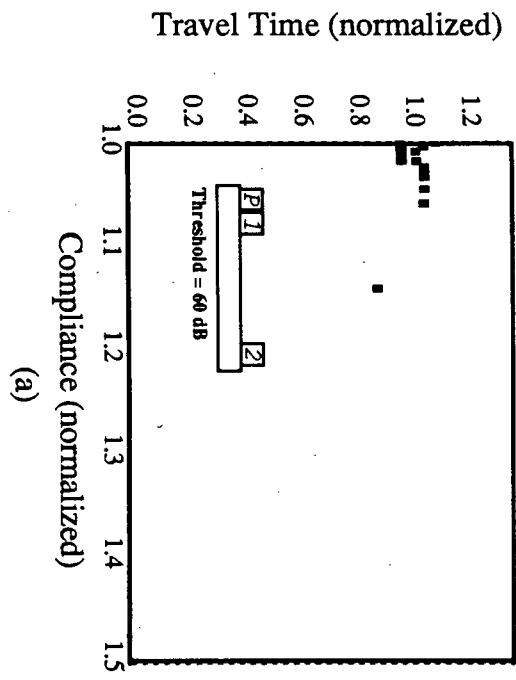


Figure 5.20 Change in AE parameters from pulser as a function of normalized compliance, rod D. (a) change in travel time. (b) change in amplitude. (c) change in duration. (d) change in energy.

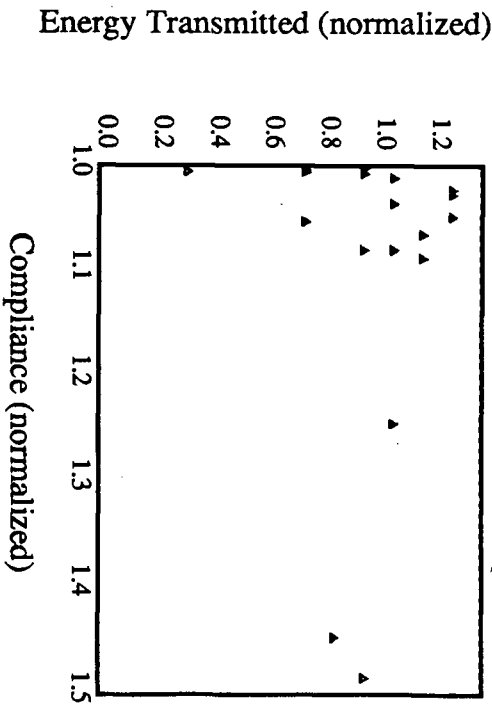
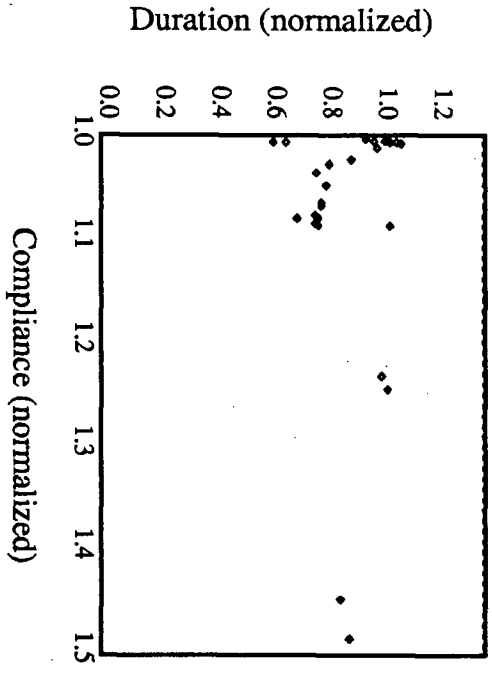
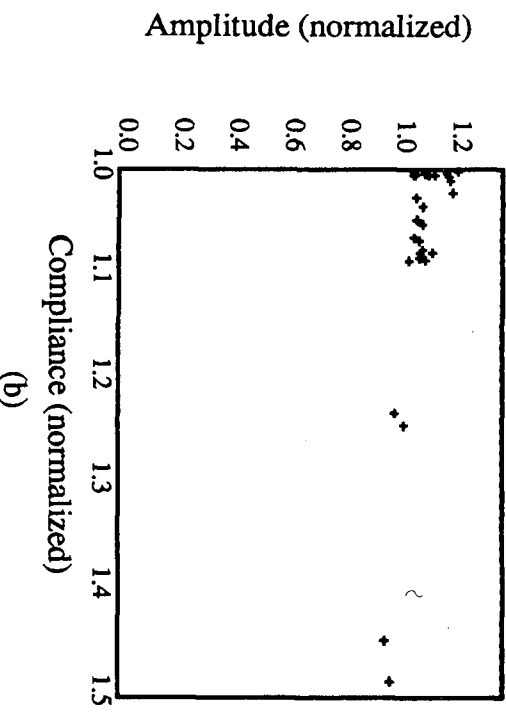
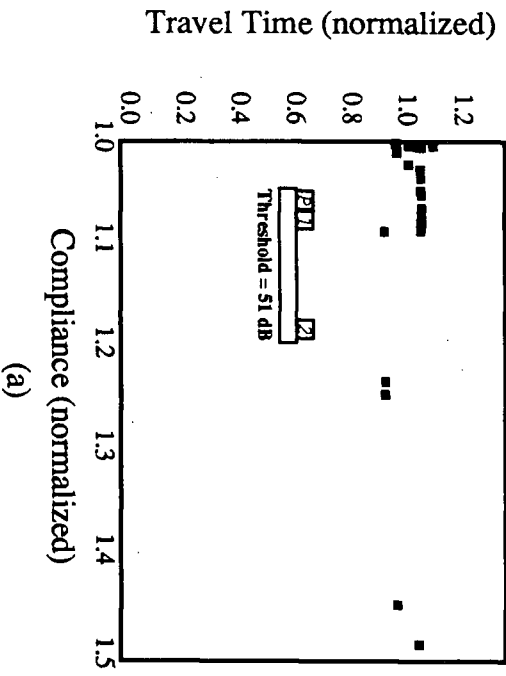


Figure 5.21 Change in AE parameters from pulser as a function of normalized compliance, rod E. (a) change in travel time. (b) change in amplitude. (c) change in duration. (d) change in energy.

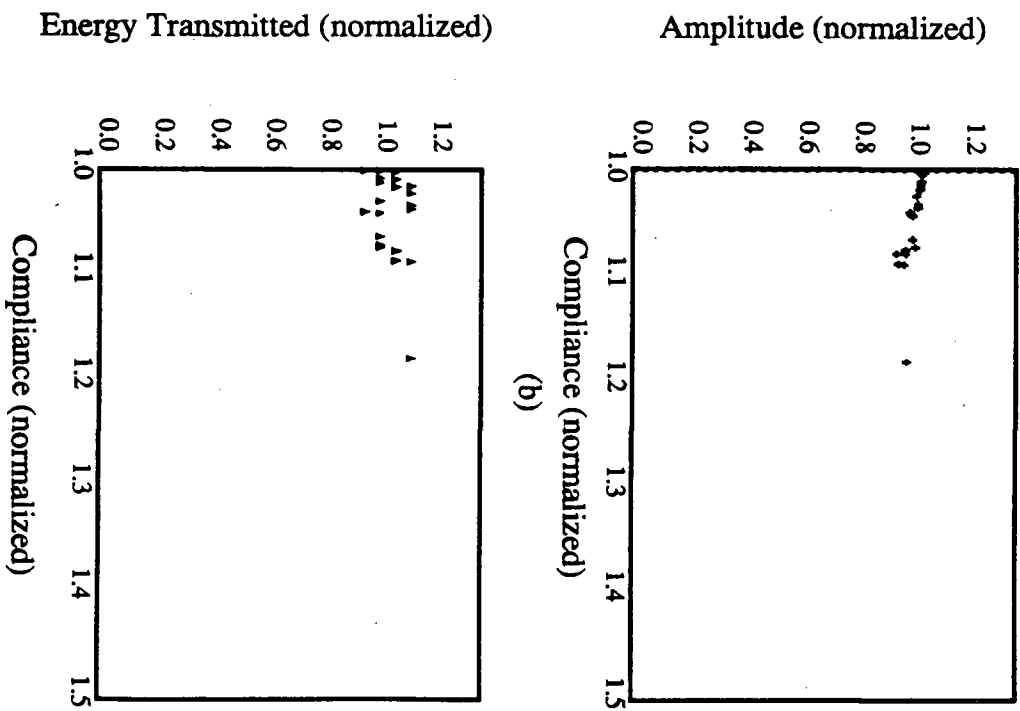
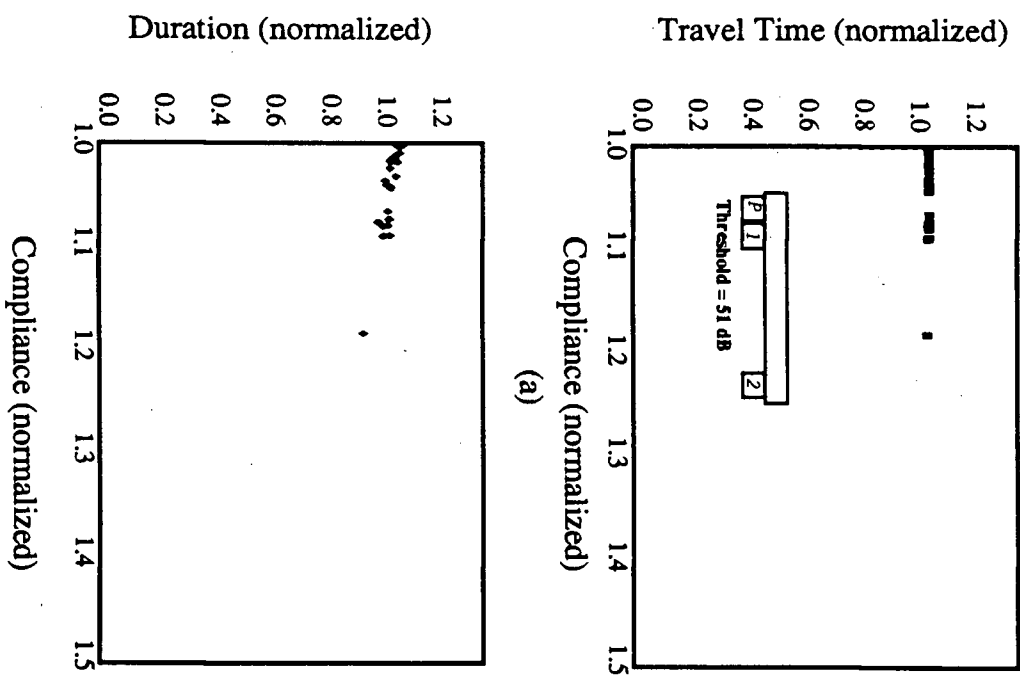


Figure 5.22 Change in AE parameters from pulser as a function of normalized compliance, rod F. (a) change in travel time. (b) change in amplitude. (c) change in duration. (d) change in energy.

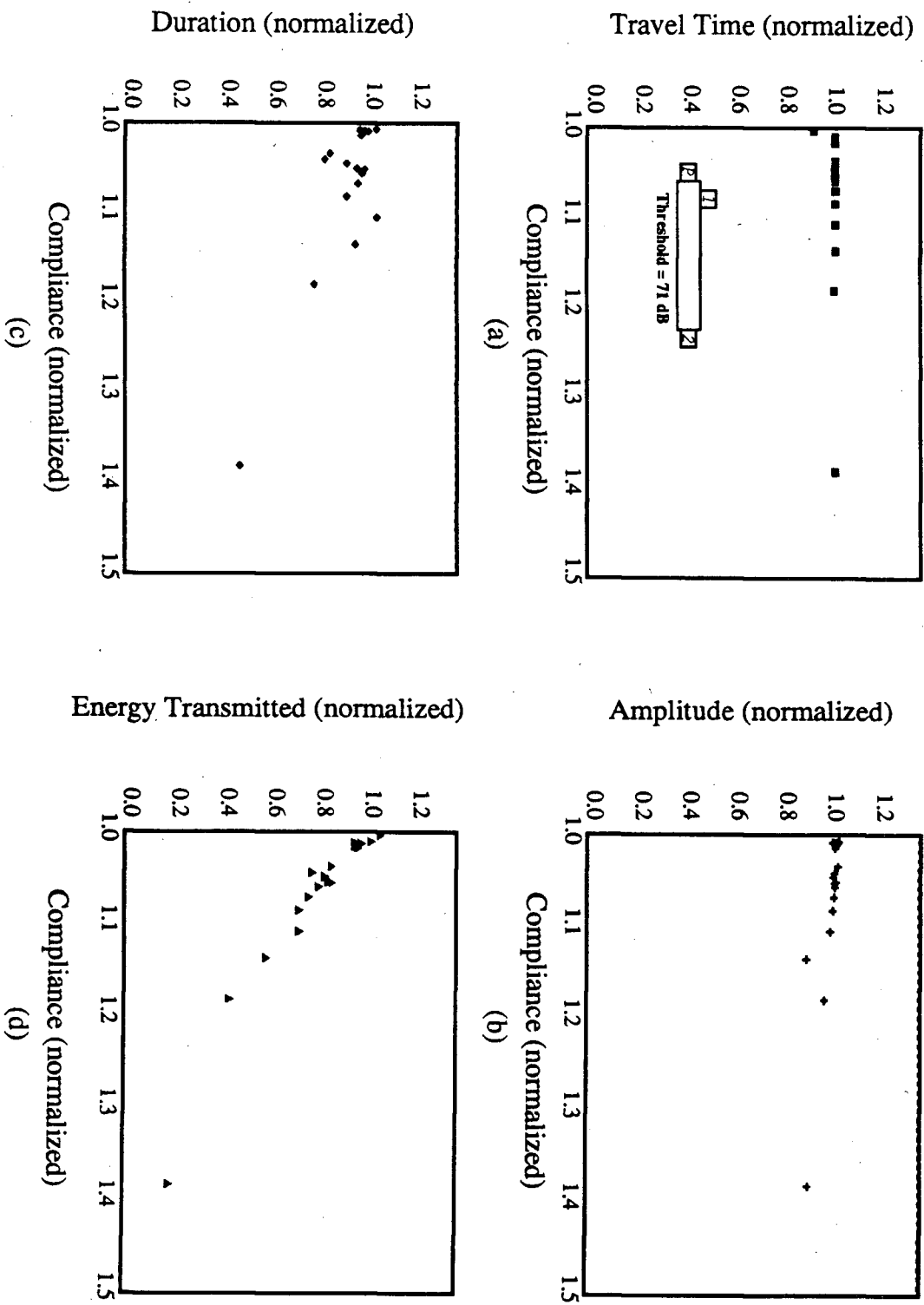
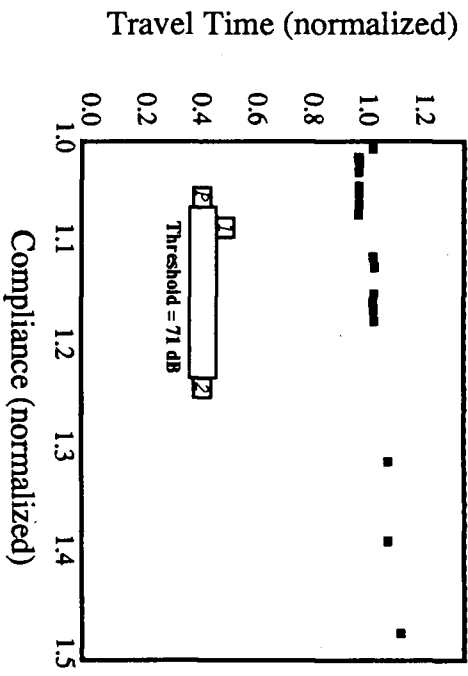
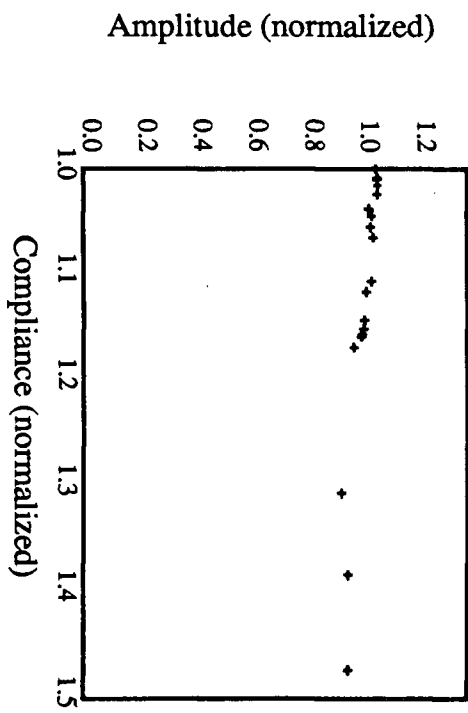


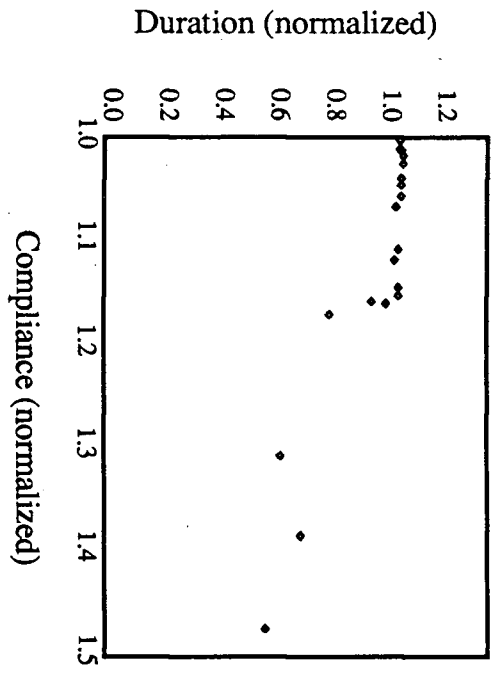
Figure 5.23 Change in AE parameters from pulser as a function of normalized compliance, rod G. (a) change in travel time. (b) change in amplitude. (c) change in duration. (d) change in energy.



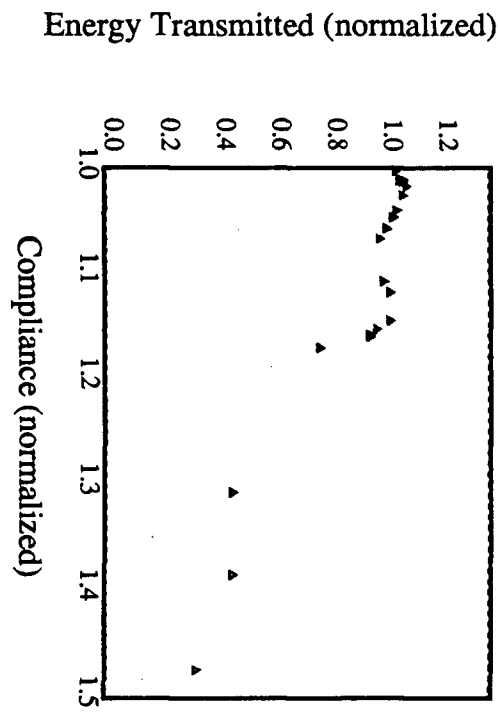
(a)



(b)



(c)



(d)

Figure 5.24 Change in AE parameters from pulser as a function of normalized compliance, rod H. (a) change in travel time. (b) change in amplitude. (c) change in duration. (d) change in energy.

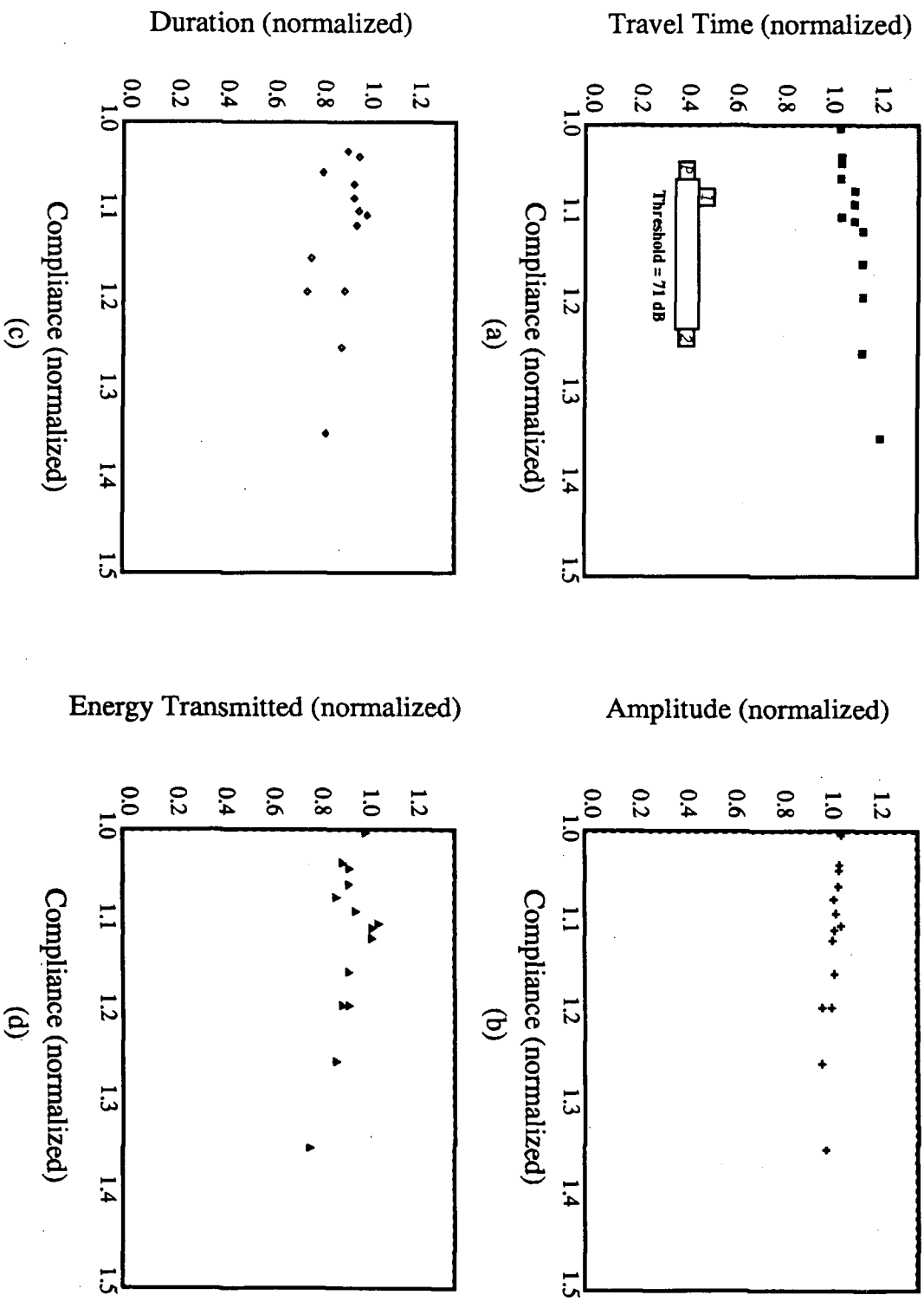


Figure 5.25 Change in AE parameters from pulser as a function of normalized compliance, rod I. (a) change in travel time. (b) change in amplitude. (c) change in duration. (d) change in energy.

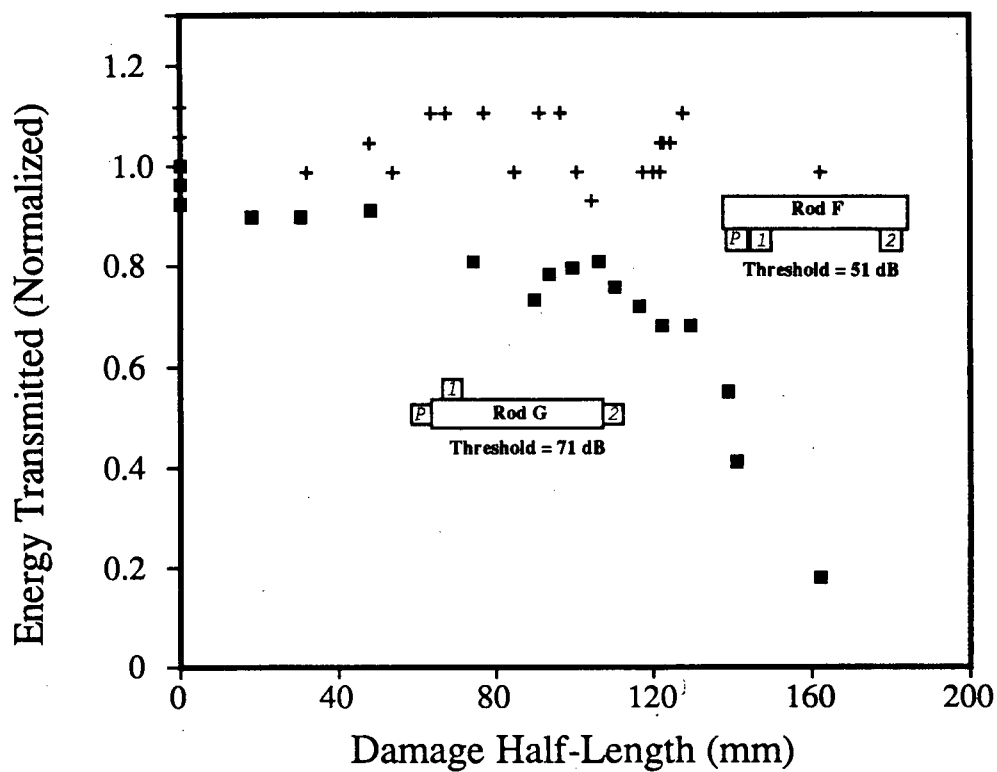


Figure 5.26 Attenuation of energy transmitted as a function of damage length, rods F and G.

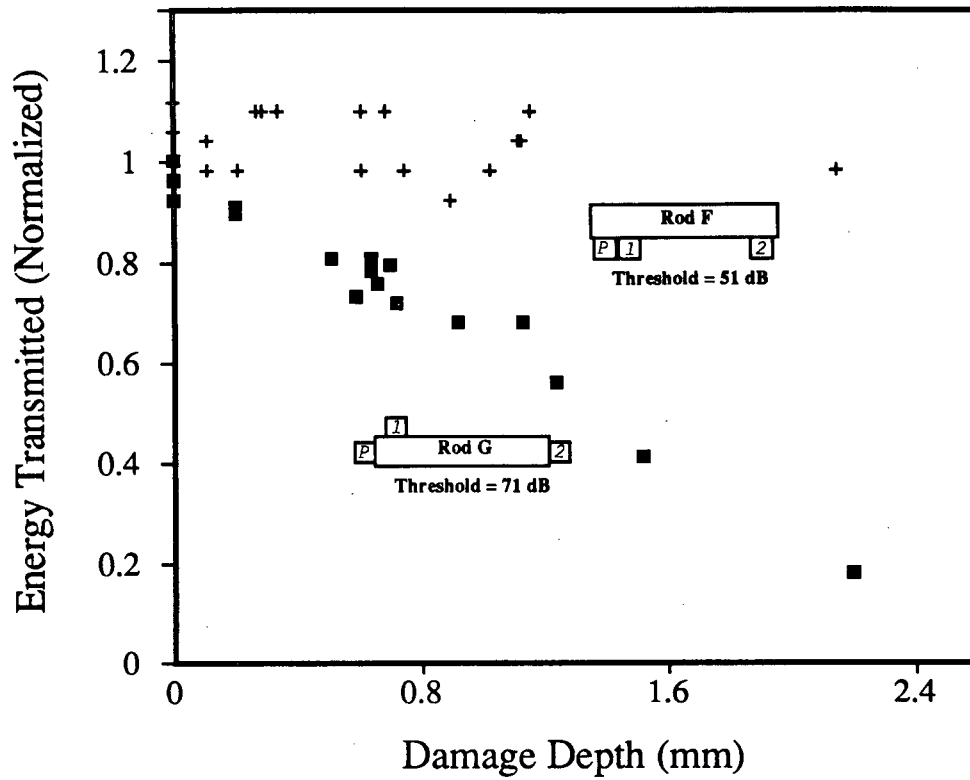


Figure 5.27

Attenuation of energy transmitted as a function of damage depth, rods F and G.

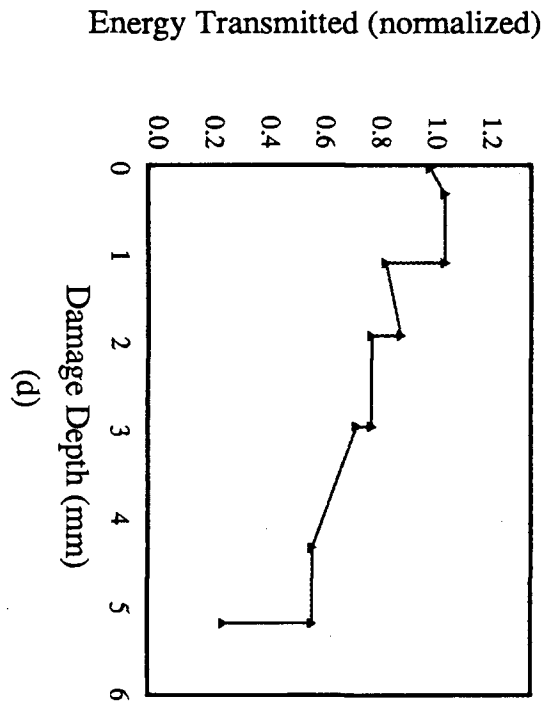
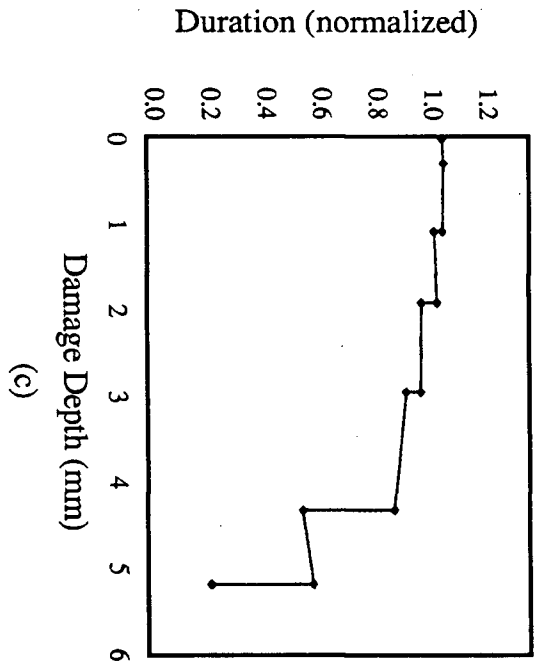
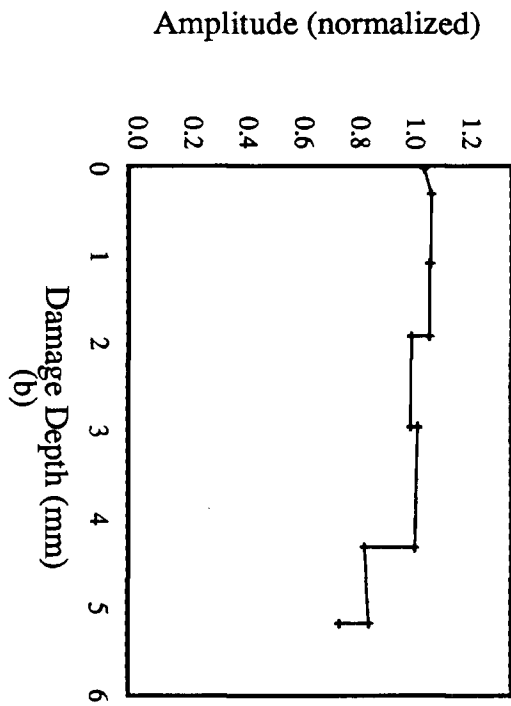
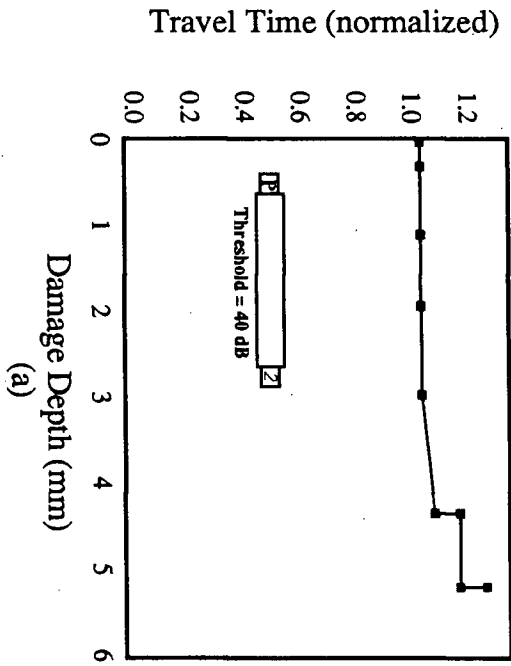


Figure 5.28 Change in AE parameters from pulser as a function of normalized compliance, laminate L. (a) change in travel time. (b) change in amplitude. (c) change in duration. (d) change in energy.

6 SUMMARY AND CONCLUSIONS

The high strength and stiffness to weight ratios of composite materials make them attractive for many structural applications in plates, shells and beams. Coupled with unique processing methods, composite structures can save weight, increase performance and reduce the number of parts required in structures and mechanical assemblies. Composite plates and shells are now used extensively by the aerospace industry for floors, doors, fairings, wing, tail and fuselage sections, rocket motor casings and other structural members that are more weight-sensitive than cost-sensitive. Recently, the automotive industry has embarked on a program of introducing composites to reduce both cost and weight. Initial attempts at manufacturing composite leaf springs have met both these objectives. This and other applications of composites to support flexural loads has given composite beams some commercial significance, yet the topic of bending has not received widespread attention in the literature and thus has provided an incentive for study.

The behaviour of unidirectional and cross-ply glass reinforced plastic beams were investigated in static and cyclic three-point bending. Aspects of damage initiation, characterization, growth and measurement were considered.

6.1 Unidirectional Beams

Static and cyclic bending of unidirectional glass reinforced plastic rods results in a damage zone which may be characterized by two dimensions, a length and a depth. During cyclic loading the rate of increase of the two damage dimensions is quite different. The ratio of deflection to load (the compliance) increases as the damage zone grows.

A non-uniform cantilever beam model, which assumes the damage depth is constant along the damage length and that the damage zone supports no load, is adequate to predict

the compliance for static loading (where a notch is cut into the tension side of the rod and the length allowed to grow). However the model consistently overestimates the compliance for cyclic loading, especially at high load ratios. The overestimate is related to the decreasing damage depth along the damage length during cyclic loading.

An expression for the energy release rate for crack extension in the length direction arises from differentiation of the closed-form solution of compliance as a function of the damage parameters. The energy release rate decreases as length increases and increases as depth increases. Damage grows in the length direction when the energy release rate G exceeds the lengthwise crack resistance G_c . For three types of rods the initial value of G_c is on the order of 200 J/m^2 . The critical energy release rate increases dramatically as the crack area increases because fibres bridging the longitudinal crack plane impede crack extension. The value of G_c completes the relation between damage parameters, a function of modulus, rod diameter, span, maximum load and G_c .

The relation between damage parameters completes characterization of damage development: damage in the depth direction grows at a uniform rate, and although the limited amount of data does not permit a growth law to be established, the growth rate during cyclic loading may be described by some empirical power law; damage in the length direction follows from the relation between damage parameters; compliance follows from the two-parameter non uniform cantilever beam model. The life of the specimen may be regarded as the number of cycles required to arrive at some increase in compliance and this number of cycles is related directly to the growth rate in the depth direction.

6.2 Cross-ply Beams

In cross-ply laminates, initiation of fatigue damage appears at laminate edges on the tension side beneath the central load point; it cannot be fully described by a damage depth and length. Neglecting initiation, damage grows in the depth and length directions, causing the compliance to increase.

Prediction of the compliance as a function of damage length and depth is based on a non-uniform cantilever beam model. A closed form expression for the compliance is derived from laminated plate theory, which takes into account stacking sequence and material properties, and agrees well with experimental results.

Crack extension in the length direction occurs when the energy release rate, derived from the compliance, exceeds the critical energy release rate. Limited results show the critical energy release rate in 0 degree plies begins at approximately 200 J/m² and increases to approximately 400 J/m². In the 90 degree plies the value is nearly 600 J/m².

6.3 Damage Measurement

Acoustic emission monitoring can be used to detect damage initiation without sophisticated test methods. One sensor was adequate to receive and record emissions before the first signs of visual damage or compliance increase in GFRP rods and laminates.

In unidirectional GFRP rods the number of fibre breaks appears to be proportional to the number of AE events which surpass a certain energy value. This was substantiated by correlations between events with energy greater than 100 and visually measured area damaged (proportional to number of fibre breaks), and between events with energy greater than 100 and compliance (related to theoretical relation involving area damaged and compliance).

Growth of damage in the length direction can be measured using two sensors by AE source location techniques. Events originating at the two advancing crack fronts were discriminated from the rest of the data following an event by event comparison between all events and events known to come from a crack front. Compared with visually measured damage length (known to be accurate) the source location was accurate for small lengths but overestimated the damage length at large lengths due to signal attenuation.

Growth of damage in the depth direction can be measured by attenuation of AE signal parameters from a simulated AE source. The most effective measure is the AE signal energy with the sending and receiving sensors mounted perpendicular to the beam longitudinal axis. The method is more sensitive to damage volume than to damage depth, but the two are related.

REFERENCES

1. Bennet, B.A., "Carbon Fibre Composites: A Light-weight alternative", Mechanical Engineering, Sept 1985 pp 36-40
2. Davidson, R., "The Torsional Fatigue Characteristics of Unidirectional Glass Reinforced Materials", Sixth International Conference on Composite Materials, July 20-24 1987 pp 4.100-4.113
3. Beardmore, P., "Composite Structures for Automobiles", Composite Structures, Elsevier Applied Science Publishers Ltd, Vol 5 1986, pp 163-176.
4. Beardmore, P. and Johnson, C.F., "The Potential for Composites in Structural Automotive Applications", Composites Science and Technology, 26 1986 pp 251-281.
5. Kocivar, B., "Rutan's Ultimate Flyer", Popular Science, Sept 1984 pp 72-75.
6. Jones, R.M., "Mechanics of Composite Materials", McGraw Hill, New York, 1975 pp
7. Katoh, T., and Yamota, K., "Development of the Graphite Epoxy Satellite Structure", Fifth International Conference on Composite materials, San Diego (1985) pp 409-418.
8. Tada, H., Paris, P.C., Irwin, G.R., "Stress Analysis of Cracks Handbook", Del Research Corp. 1973
9. Jones, R.M., "Mechanics of Composite Materials", McGraw Hill, New York, 1975 pp 76-80
10. Jones, R.M., "Mechanics of Composite Materials", McGraw Hill, New York, 1975 pp 76-80
11. Griffith, A.A., "The Phenomena of Rupture and Flow in Solids", Phil. Trans. Roy. Soc. London A 221 (1921) pp 163-197.
12. Beaumont, P.W.R., and Phillips, "Tensile Strength of Notched Composites", J. Composite Materials, Vol 6 (Jan 1972) pp 32-46
13. Beaumont, P.W.R., and Tetelman, "The Fracture Strength and Toughness of Fibrous Composites", Failure Modes in Composites, The Metallurgical Society, AIME, 1974, pp 49-80
14. Wolla, J.M. and Goree, J.G., "Experimental Evaluation of Longitudinal Splitting in Unidirectional Composites", J. Composite Materials, Vol 21 (January 1987) pp 49-67
15. Slepetz, J.M., and Carlson, L., "Fracture of Composite Compact Tension Specimens", Fracture Mechanics of Composites, ASTM STP 593, 1975 p 143-162
16. Konish, H.J., Swedlow, J.R. and Cruse, T.A., "Experimental Investigation of Fracture in an Advanced Fiber Composite", J. Composite Materials, Vol 6 (January 1972) pp 114

17. Reifsneider, K.L. "Life Prediction Analysis: Directions and Divigations", Sixth International Conference on Composite Materials, July 20-24 1987 pp 4.1-4.31
18. Russell, A.J. and Street, K.N. "The Effect of Matrix Toughness on Delamination: Static and Fatigue Fracture Under Mode II Shear Loading of Graphite Fiber Composites", Toughened Composites, ASTM STP937, Norman J. Johnson, Ed., American Society for Testing and Materials, Philadelphia, 1987, pp 275-294
19. O'Brien, T.K., "Characterization of Delamination Onset and Growth in a Composite Laminate", Damage in Composite Materials, ASTM STP 775 1982 pp 140-167.
20. Poursartip, A., "The Characterization of Edge Delamination Growth in Laminates Under Fatigue Loading", Toughened Composites, ASTM STP937, Norman J. Johnson, Ed., American Society for Testing and Materials, Philadelphia, 1987, pp 222-241
21. Springer, G.S. "Environmental Effects on Composite Materials", Technomic Publishing Co. 1981 pp 1-5
22. Bodig, J.B. and Jayne, B.A. "Mechanics of Wood and Wood Composites", Van Nostrand Rheinhold Co., 1982 pp 303-334.
23. Poursartip, A., Dorosh, M., Nadeau, J.S. and Bennett, R. "Acoustic Attenuation as a Measure of Damage in GFRP Rods", Second Int'l Conf. on Acoustic Emission from Reinforced Plastics, July 1986
24. De Roo, P. and Paluch, B. "A Fatigue Damage Model for Unidirectional Composites" Sixth International Conference on Composite Materials, July 20-24 1987 pp 4.431-4.442
25. Croman, R.B. "Flex Fatigue of Graphite Reinforced Thermoplastics", Sixth International Conference on Composite Materials, July 20-24 1987 pp 4.76-4.88
26. Bader, M.G. and Ellis, R.M. "The Effect of Notches and Specimen Geometry on the Pendulum Impact Strength of Uniaxial CFRP", Composites Nov 1974 pp 253
27. Han, K.S., and Koutsky, J., "Interlaminar Fracture Energy of Glass Fiber Reinforced Composites", J. Comp. Materials Vol 15 July 1981 pp 371-388
28. Broek, D., "Elementary Engineering Fracture Mechanics", Martinus Nijhoff 1982 pp 183
29. Devitt, D.F., Schapery, R.A. and Bradley, W.L. "A Method for Determining the Mode I Delamination Fracture Toughness of Elastic and Viscoelastic Composite Materials", J. Composite Materials, Vol 14 (Oct 1980) p 270
30. Poursartip, A., Ashby, M.F. and Beaumont, P.W.R., "Damage Accumulation During Fatigue of Composites", Scripta Metallurgica Vol 16 1982 pp 601-606
31. Highsmith, A.L. and Reifsneider, K.L., "Stiffness-Reduction Mechanisms in Composite Laminates", Damage in Composite Materials, ASTM STP 775 1982 pp 103-117.

32. Pao, Y.S. and Gajewski, R.R. "The Generalized Theory and Transient Responses in Layered Solids" J. Physical Acoustics Vol 13 (1977) pp 183-265
33. Kline, R. "Acoustic Emission Signal Characterization" Ed by J.R. Matthews, Gordon and Breach Sci. Pub. 1983 pp 105-138
34. Stephens, R. and Kim, H. "Acoustic Emission - A Diagnostic Tool in Non-Destructive Testing", Ultrasonic Testing, Ed. by J.R. Szilard, John Wiley and Sons, 1982 pp 459-489
35. Harris, D., Dunnegan, H., and Tetelman, A. Technical Bulletin DRC 105 Dunnegan Research Corp. 1983
36. Ishakawa, K. and Kim, H., J. Mat. Sci. Vol 9 (1974) p 737
37. Pao, Y.S. "Theory of Acoustic Emission" ASME Symposium on Elastic Waves and NDT of Materials, 1978 pp 107-128
38. Michaels, J., Michaels, T. and Sasche, W. "Applications of Deconvolution to Acoustic Emission Signal Analysis" Materials Evaluation 39 (Oct 1981) pp 1032-1036
39. Brown, T. and Mitchell, J. "Acoustic Emission Evaluation of Automotive Hybrid Composites and Attachments" 35 th Reinforced Plastics/Composites Inst. Conf. New Orleans LA Feb 1980 paper 26-B
40. Ono, K. "Acoustic Emission Behavior of Flawed Unidirectional Carbon Fiber-Epoxy Composites" Conf. on Acoustic Emission from Reinforced Plastics, July 1986, pp 22-28
41. Ponsot, B. and Valentin, D. "Acoustic Emission Analysis of the Dependence of Damage Accumulation in Composites on Matrix Properties" Conf. on Acoustic Emission from Reinforced Plastics, July 1986, pp 5-11
42. Berthelot, J. "Relation Between Amplitudes and Rupture Mechanisms in Composite Materials" Conf. on Acoustic Emission from Reinforced Plastics, July 1986, pp 126-133
43. Gorman, M. and Foral, R. "Acoustic Emission Studies of Fiber/Resin Double Cantilever Beam Specimens" Conf. on Acoustic Emission from Reinforced Plastics, July 1986, pp 104-109
44. Eckles, W. and Awerbuch, J. "Monitoring Acoustic Emission in Cross-Ply Graphite/Epoxy Laminates During Fatigue Loading" Conf. on Acoustic Emission from Reinforced Plastics, July 1986, pp 78-84
45. Maslouhi, A., Roy, C. and Proulx, D. "Characterization of AE Signals Generated in Carbon-Epoxy Composites" Conf. on Acoustic Emission from Reinforced Plastics, July 1986, pp 112-116
46. Fitz-Randolph, J. and Phillips, D., Beaumont, P.W.R. and Tetelman, A. "Acoustic Emission Studies of a Boron-Epoxy Composite" J. Composite Materials Vol 5 (1971) pg 541

47. Hamstad, M. and Moore, R. "Acoustic Emission from Single and Multiple Kevlar 49 Filament Breaks" J. Composite Materials Vol 20 (Jan 1986) pp 46-66
48. Gorman, M. and Rytting, D. "Long Duration AE Events in Filament Wound Graphite/Epoxy in the 100-300 kHz Band Pass Region" Conf. on Acoustic Emission from Reinforced Plastics, July 1984, session 6
49. Awerbuch, J., Gorman, M., and Madhukar, M. "Monitoring Damage Accumulation in Filament Wound Graphite/Epoxy Laminate Coupons During Fatigue Loading Through Acoustic Emission" Conf. on Acoustic Emission from Reinforced Plastics, July 1984, session 2
50. Ghafarri, S. and Awerbuch, J. "Monitoring Acoustic Emission in Impact Damaged Composites" Conf. on Acoustic Emission from Reinforced Plastics, July 1986, pp 120-125
51. Mitchell, J. and Miller, R. "Acoustio-Ultrasonics Principles and Instrumentation" Conf. on Acoustic Emission from Reinforced Plastics, July 1986, pp 222-225
52. "Recommended Practice for Acoustic Emission Testing of Fiber Reinforced Plastic Tanks/Vessels" The Society of the Plastics Industry, New York NY 1982
53. Swanson, T. "Development of Codes, Standards and Practices for Acoustic Emission Examination of Composites in the United States" Conf. on Acoustic Emission from Reinforced Plastics, July 1986, pp 177-178
54. "Recommended Practice for Acoustic Emission Testing of Fiberglass Reinforced Plastics Piping Systems" Conf. on Acoustic Emission from Reinforced Plastics, July 1983
55. Whalley, G. and Cole, D. "Development of AE Techniques for Quantitative Use on Aerospace CFRP Structures" Conf. on Acoustic Emission from Reinforced Plastics, July 1984, session 4
56. Holroyd, T. and Cox, P. "An Approach to AE Monitoring During the Rig Shop Testing of Large CFRP Aero-Engine Components" Conf. on Acoustic Emission from Reinforced Plastics, July 1986, pp 189-192
57. Timoshenko and Goodier, "Theory of Elasticity", McGraw Hill 1970 pg 41-46
58. Jones, "Mechanics of Composite Materials", McGraw Hill, New York, 1975 pp 301
59. Cooper, W.D., and Helfrick, A.D., "Electronic Instrumentation and Measurement Technology", Prentice Hall, 1985 pp 348-362
60. "Brittle Fracture of Non-Ceramic Insulators", Can. Elec. Assoc. Proj. CEA 186 T350, 1985
61. Broek, D., "Elementary Engineering Fracture Mechanics", Martinus Nijhoff 1982 pp 250-256
62. Jones, R.M., "Mechanics of Composite Materials", McGraw Hill, New York, 1975 pp 147-187

The increased use of composites as structural materials over the past two decades as structural components in automobiles, military and civilian aircraft and spacecraft has created a demand for capable non destructive evaluation (NDE) techniques and challenges NDE engineers to perfect novel NDE methods and to adapt old ones to inhomogeneous, non-metallic materials. Effective NDE methods must identify defects or damaged areas without degrading the sample and provide reliable information regarding type, location and severity of defects or damaged areas. Fortunately there is an extensive variety of suitable methods in use and a number of promising new techniques under development. Unfortunately there is no single method that is applicable under all conditions for all types of composites. Thus users of composites must be familiar with an assortment of procedures to ensure the integrity of their products. Acoustic emission (AE) is a relatively new technique which has received a great deal of attention.

Acoustic emission belongs to the class of NDE methods for composites known as acoustic methods (ultrasonics, acoustic emission and some similar techniques). In general any method where the transmission or detection of elastic waves is involved may be termed acoustic. Acoustic emissions are the generation of transient elastic waves by a rapid release of strain energy from a localized source from within a material. Waves advancing through an elastic solid cause particles in the medium to vibrate, transferring energy from particle to particle along the wave path. The conduct of these waves must be understood to appreciate acoustic emission as a tool for NDE of composite materials.

In a linearly elastic solid, four separate kinds of stress waves may exist. These are :

- longitudinal (compression, dilatational)
- transverse (shear, distortional)
- surface (Rayleigh)
- plate (Lamb)

Figure A.1 shows longitudinal, transverse and surface waves.

Longitudinal waves are those in which particle motion is parallel to the direction of wave propagation. Pressure waves travelling through air are a familiar example. For isotropic materials the velocity of propagation of such waves is

$$C = \sqrt{\frac{E}{\rho} \frac{(1-\nu)}{(1+\nu)(1-\nu)}} \quad (A.1)$$

for a three dimensional bulk elastic solid where E is Young's modulus, ρ is the density and ν is Poisson's ratio.

Transverse waves are those in which particle motion is perpendicular to the propagation direction. Since the velocity of this wave is less than the former, the two waves will refract at two different angles when transcending a boundary.

Rayleigh waves are a combination of longitudinal and shear waves that propagate along free boundaries or interfaces. These vibrations move easily at surfaces but are dissipated rapidly as they penetrate the material. The horizontal and vertical displacements travel at a third wave speed, slower than the previous two.

Similar to Rayleigh waves, plate waves are a combination of longitudinal and transverse modes. They combine in various ways to satisfy conditions at a free plane surface or internal interface. Particle motion is similar to that in Rayleigh waves although these disturbances occur only in thin sections, their velocity being a function of thickness and frequency.

The presence of interfaces between dissimilar materials in a composite gives rise to complex wave paths. Refraction and reflection occur at interfaces between dissimilar materials due to a change in acoustic velocity. A single incident wave type may be reflected or refracted when crossing a boundary or interface into any of the four wave types. When an acoustic wave strikes a boundary part of its energy is transmitted through the boundary and part is reflected. The relative amounts depend on the acoustic impedance of the materials on either side of the boundary. The acoustic impedance is a material property which is a measure of the material's resistance to wave propagation. For the simple case of a harmonic wave incident at 90 degrees to a material boundary the fraction of the transmitted energy is

$$T = \frac{4R_1R_2}{(R_1 + R_2)^2} \quad (A.2)$$

where R_1 and R_2 are the impedances of the materials on either side of the boundary. Cases other than this are remarkably complex. The vast number of interfaces within a composite cause difficulty in determining the wave path and subsequent transmitted and reflected energies. In addition to being scattered by reflection and refraction, an acoustic wave propagating through a material may also be absorbed and dissipated as heat. All of these effects are conveniently accounted for by the concept of attenuation, the loss in strength of a signal over the path travelled between source and receiver.

The discussion to this point covers only the basics of wave propagation in solids. The problem of transient waves travelling in anisotropic solids has only begun to be solved. In an article by Pao the generalized ray theory is presented as a means of analyzing acoustic emission signals. Unfortunately the theory has not been developed for orthotropic materials and may prove too complex for large numbers of emissions. Therefore no convergence of the above mentioned basics of wave propagation to the accurate description of acoustic emission in composites is expected; it is instructive, however, to realize the following points:

- A single acoustic emission may travel at four different speeds along a very complex path from source to receiver.
- A signal may be changed significantly along its path from source to receiver. Reflections and refractions at interfaces and free surfaces cause the waves to travel along a path which is not necessarily a straight line between source and receiver. Along this path waves are attenuated, or reduced in strength, by interacting with material boundaries.
- A single signal may be detected more than once. Waves may both reflect and refract at the same interface, causing multiple waves to propagate at different speeds and arrive at different times at the same receiver.

Rather than pursue the theoretical aspects of wave propagation, the usual approach in AE testing is to analyze each recorded AE signal or event. Acoustic emission events have been classified as either "burst" or "continuous". Burst emissions are those which are well enough separated in time to appear as discrete signals. Continuous emissions are essentially bursts which occur so close together, perhaps overlapping, that they cannot be resolved.

Unlike a transient recorder, acoustic emission equipment does not record and store complete waveforms. Instead, five parameters of each detected waveform are stored. The five parameters are the amplitude, duration, energy, counts and rise time.

The magnitude or sound pressure of an acoustic wave is an important parameter in acoustic methods. This quantity is difficult to measure so the relative sound pressure or amplitude is normally used, defined as

$$Amp = 20 \log \frac{P}{P_0} \quad (A.3)$$

where P is the detected sound pressure and P_0 is the minimum or threshold sound pressure. The quantity P is measured with a transducer, a device that converts a small surface deflection into a voltage. The value P/P_0 is assumed to be proportional to V/V_0 , the induced and threshold voltages of the transducer. V_0 is customarily taken as 1 micro-volt.

The duration of an AE event is measured as the time between first and final penetration of a pre-set threshold. The threshold is set electronically at a constant amplitude, typically 60 dB.

Similar to duration, the rise time is measured as the time between first penetration of the threshold and maximum amplitude.

The number of counts in an AE signal is the number of times the signal exceeds the threshold value. A single event may have any number of counts from one or two to several hundred.

Energy analysis can be achieved in two ways. The waveform can be digitized and integrated or integrated electronically. Analogue-digital conversion devices with high enough frequency resolution (ie transient recorders) do not have the storage capacity to capture tens of thousands of events. Thus the waveform is normally integrated electronically (the area under the voltage squared-time curve), figure A.2. If the sensor response is proportional to the surface displacements associated with the passing of a stress wave, then the electrical energy in the sensor is proportional to the mechanical energy in the stress wave. Values reported as "energy", then, are not absolute values, but are (linearly) proportional to stress wave energy. If the assumptions regarding sensor response and surface displacement are true then processes releasing high amounts of strain energy should have higher energies than processes releasing smaller amounts of strain energy.

Acoustic emission instrumentation consists of transducers, preamplifiers and a storage and output device. The ideal sensor is one which faithfully reproduces the waveform it receives. In a practical sense this means the sensor should have high sensitivity and a flat frequency response. Sensitivity refers to the minimum surface deflection detectable. For piezoelectric transducers (converts a surface displacement into a voltage), by far the most common in AE work, the sensitivity is believed to be near $1e-13$ m. For non-contacting laser interferometric transducers (surface displacement measured by change in optical path length) the sensitivity is $1e-12$ to $1e-11$ m. Rarely used capacitance microphones (surface displacement measured by capacitance change in

electrostatic element) have a sensitivity of $1e-12$ m, but a near ideal flat frequency response. For piezoelectric transducers the amplitude decreases with frequency, but in a jagged, step-like fashion. The transducer is more sensitive to some frequencies than others. There is a distinction between broad-band and resonant piezoelectric transducers. The resonant (undamped) type is highly sensitive at the resonant frequency, less sensitive at other frequencies. The broad band (damped) type has a roughly flat frequency response over a wider frequency range, but is less sensitive. Though easy to use, the piezoelectric transducer does not give an accurate measure of surface displacement. In different parts of its operating frequency range the transducer may be sensitive to surface displacement, velocity or acceleration. This has some serious implications regarding the assumption of transducer output giving an accurate representation of an incident stress wave. It was assumed that the transducer response was directly proportional to the surface displacement. However, the transducer may be more sensitive to waves of certain frequencies or not sensitive to displacement at all. It has already been shown that stress waves from the same source acting at distance x and $2x$ from a receiver may differ from one another by the time the waves reach the sensor location. Once the waveforms are detected, and perhaps further altered, by the receiver the two initially similar waveforms may bear little resemblance to one another. It appears that accurate identification of a variety of sources acting at various locations in a composite presents an enormous challenge.

Preamplification of the received signal is necessary to differentiate between AE and background noise. Typically the signal is amplified by 40 dB (100 X). For filtering out background noise the preamplifier has a built in band-pass filter, typically 100 kHz to 300 kHz. All signals within this range are accepted and recorded. Signals outside this range, say noise from rotating machinery, are not recorded.

In the laboratory the storage/output device is a microcomputer. Events are stored in a standard format on a floppy or a fixed disk. This data can be manipulated by software included with the equipment and plotted either on a CRT or printer for analysis.

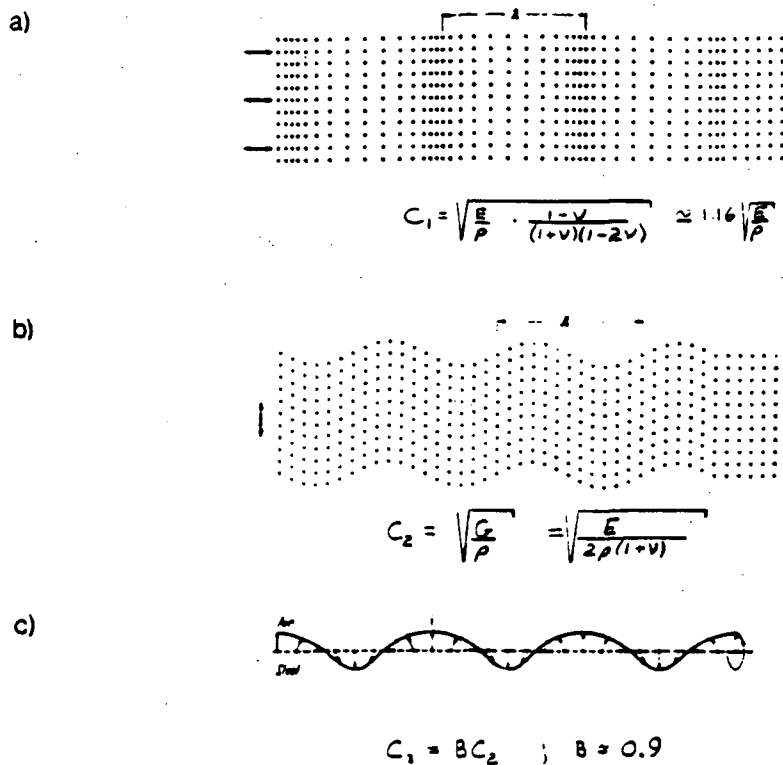


Figure A.1 (a) Longitudinal wave.
 (b) Transverse wave.
 (c) Rayleigh wave.

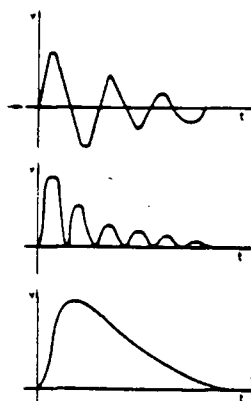


Figure A.2 Acoustic emission energy measurement.

APPENDIX B Area Moments of Inertia

The two area moments of inertia I_1 and I_2 remain to be determined. The area moment of inertia of the undamaged section, figure B.1 (a), is the well known expression

$$I_1 = \pi \frac{r^4}{4} \quad (B.1)$$

The area moment of inertia of the damaged section, figure B.1 (b), is more complex. The depth d leaves a circular cross section with a sector removed. Referring to figure B.1 (b) the moment of inertia about the midplane can be found by applying the formula for moment of inertia

$$I_{xx} = \int_A y^2 dA \quad (B.2)$$

From figure B.1 (b) an element of area dA is defined as the product of cross section width and infinitesimal depth increase dy .

$$dA = (2x)dy = 2\sqrt{r^2 - y^2} dy \quad (B.3)$$

For a given depth d the moment of inertia reduces to

$$I_{xx} = \int_{-(r-d)}^r 2y^2\sqrt{r^2 - y^2} dy \quad (B.4)$$

Integrating this expression

$$I_{xx} = 2\left(-y \frac{(r^2 - y^2)^{3/2}}{4} + r^2 y \sqrt{\frac{r^2 - y^2}{8}} + \frac{r^4}{8} \sin^{-1}\left(\frac{y}{r}\right)\right)_{d-r}^r \quad (B.5)$$

Substituting the integrator limits

$$2\left(\frac{\pi r^4}{16} - \left(\frac{(r-d)(2rd-d^2)^{3/2}}{4} + \frac{r^2(d-r)(2rd-d^2)^{1/2}}{8} + \frac{r^4}{8} \sin^{-1}\left(\frac{d-r}{r}\right)\right)\right) \quad (B.6)$$

In applying the flexure formula the moment of inertia of the cross section area about the neutral axis must be found. The moment of inertia about the neutral axis is found from the moment of inertia about the centroidal axis of the full circle from the parallel axis theorem. The theorem states that the moment of inertia of any area around any axis is equal to the moment of inertia of the same area around a parallel axis passing through the area's centroid plus the product of the same area and the square of the distance between the two axes. In this case, with A_{cs} representing the area of the damaged cross section

$$I_{xx} = I_2 + A_{cs}h^2 \quad (B.7)$$

$$I_2 = I_{xx} - A_{cs}h^2 \quad (B.8)$$

The area damaged, A_d , is a sector of depth d . From figure B.1 (c)

$$A_d = \frac{\theta}{2\pi} \pi r^2 - (r-d)\sqrt{2rd-d^2} \quad (B.9)$$

Making the substitutions

$$\sin \alpha = \frac{r-d}{r} \quad (B.10)$$

$$\theta = \pi - 2\alpha = \pi - 2 \sin^{-1} \frac{r-d}{r} \quad (B.11)$$

the area damaged is

$$A_d = \frac{r^2}{2} \left(\pi - 2 \sin^{-1} \left(\frac{r-d}{r} \right) \right) - (r-d) \sqrt{2rd - d^2} \quad (B.12)$$

Therefore the cross section remaining is

$$A_{cs} = \pi r^2 - \left(\frac{r^2}{2} - \left(2 \sin^{-1} \left(\frac{r-d}{r} \right) - (r-d) \sqrt{2rd - d^2} \right) \right) \quad (B.13)$$

The final step is to find the centroid of the area remaining. By defining y as shown in figure B.1 (a) the centroid is the distance h .

$$h = \bar{y} = \frac{\int y da_{cs}}{A_{cs}} \quad (B.14)$$

The element of area da_{cs} is the same as that in Eq. (B.3). Hence

$$h = \frac{2}{3A_{cs}} (2rd - d^2)^{3/2} \quad (B.15)$$

Finally, combining Eqs. (B.5), (B.10) and (B.13)

$$I_2 = I_{xx} - \frac{4}{9A_{cs}} (2rd - d^2)^3 \quad (B.16)$$

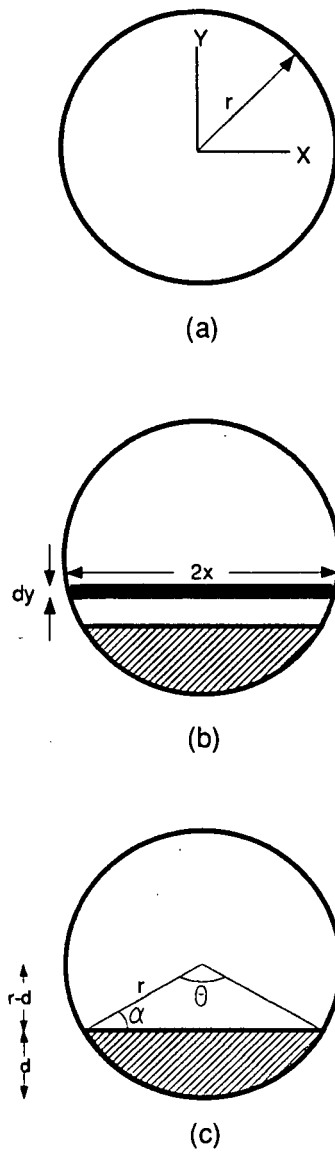


Figure B.1 (a) Undamaged cross section
 (b) Damaged cross section
 (c) Area damaged

APPENDIX C Determination of D'_{11}

The longitudinal modulus, transverse modulus and Poisson's ratio are determined from the fibre volume fraction (38%) and micromechanics principles*.

Longitudinal Modulus

$$E_L = E_f V_f + E_m V_m$$

where E represents modulus, V represents volume fraction and the subscripts f and m represent fibre and matrix. Substituting the material properties

$$E_L = (72)(0.38) + (5)(0.62) = 30.5 \text{ GPa}$$

Transverse Modulus

$$E_T = E_m \left(\frac{1 + \zeta \eta V_f}{1 - \eta V_f} \right)$$

$$\eta = \frac{E_f E_m - 1}{E_f E_m + \zeta}$$

Substituting the fibre and matrix moduli and $\zeta = 2$

$$E_T = 10.3 \text{ GPa}$$

Poisson's Ratio

$$\nu_{LT} = \nu_f V_f + \nu_m V_m$$

$$\nu_{LT} = (0.3)(0.32) + (0.3)(0.68) = 0.3$$

* see, for example, Agarwal, B.D. and Broutman, L.J. "Analysis and Performance of Fiber Composites", John Wiley & Sons, 1980 pp 39